XXXVIII

CICLO DEL CORSO DI DOTTORATO

The Fracture Toughness Enhancement of Micro-ceramic

Titolo della tesi

Wenjuan Cheng

Nome e Cognome del dottorando:

Prof. Marco Sebastiani

Doc[redacted]

Pro[redacted]

Coor[redacted]

To my dearest family, for their unconditional love that has shaped who I am.

To my grandfather, who would have been very proud of me, even though he is now in another world.

And to myself.

Acknowledgements

Eventually, I arrive at this moment to finalize my thesis. Although three years of PhD life seem to have passed in the blink of an eye, for me the journey to reach this point has been much longer. Above all, I would like to offer my first acknowledgment to myself—thank you for not being defeated by difficulties and negative emotions. You made it.

It has been a great pleasure to work with and learn from so many remarkable people throughout my PhD journey. Firstly, I would like to express my deepest gratitude to Prof. Marco Sebastiani for giving me the opportunity to join this project and for introducing me to this research field. Your guidance and supervision encouraged me to explore my potential and broaden my research interests. Meanwhile, I would like to sincerely thank Dr. Edoardo Rossi for his constant support and assistance in all aspects of my work. Your help and encouragement have greatly contributed to both my professional and personal growth.

My heartfelt thanks go to Prof. Edoardo Bemporad, Dr. Daniele De Felicis, Ilaria Favuzzi, Giulia Gigante, Daniele Duranti, Valerio Savo, Chiara De Bernardo, Saqib Rashid, Meral Tuna Eroglu, and all other colleagues at Roma Tre. Thank you for helping me adapt to laboratory life when I first arrived in Rome, and for your invaluable support in research activities and experiments.

I am also deeply grateful to Dr. Jens Bauer and the colleagues at KIT for their support during my three-month visiting period. This experience was extremely rewarding, providing me with valuable research skills and unforgettable professional experiences. I would like to sincerely thank Prof. Rostislav Daniel for his supervision during my stay at Montanuniversität Leoben. My appreciation also goes to Prof. Andrea M. Hodge and Dr. Danielle E. White from USC for their collaboration and support on the PVD-related experiments.

To all my friends, both in China and abroad, who have offered me emotional support, thank you for listening to my complaints and for your constant encouragement. Your presence made me feel that I was never alone and gave me the courage and confidence to keep moving forward.

Finally, to my dearest family in the world, thank you for your unwavering support. I know that deep in your hearts, you may have wished for me to live a life that is easier and more stable. Yet you chose to respect and support all of my decisions, allowing me to pursue whatever I wanted to try, surrounded by your love. You celebrate every small victory of mine, feel proud of each achievement, and worry during my difficult moments. Even though you often say you feel sorry that you were not able to accompany me more closely or offer more guidance in my academic and professional path, your unconditional love has been my greatest source of strength and motivation to overcome every challenge.

After three years of training, I may still not be highly skilled, but I have truly grown into a better person—stronger and more capable of facing life and the world. Finally, to the person I was four years ago, who doubted whether she was making the right decision: follow your heart, and go ahead.

Abstract

Micro- and nano-architected ceramics offer exceptional stiffness-to-weight ratios, thermal stability, and multifunctionality, yet their widespread application remains limited by intrinsic brittleness and flaw sensitivity at small length scales. As the characteristic dimensions of ceramic components approach the micron and sub-micron regime, fracture behavior becomes increasingly governed by surface condition, residual stress, and interface architecture rather than bulk material properties alone. This thesis investigates physically grounded surface- and interface-engineering strategies to enhance fracture resistance and control deformation behavior in micro-scale ceramic systems.

The thesis begins by establishing a reliable intrinsic mechanical baseline for sinterless silica fabricated via two-photon polymerization and low-temperature pyrolysis. Using nanoindentation and micropillar splitting, the elastic modulus, hardness, and fracture toughness of printed silica are quantitatively benchmarked against conventionally fabricated silica, demonstrating mechanical equivalence despite drastically reduced processing temperatures and enabling confident use of this material platform for microscale architectures.

Building upon this baseline, the thesis next explores fracture toughness enhancement of micro silica through atomic layer deposition (ALD) stress engineering. By conformally coating silica micropillars with thin amorphous Al_2O_3 and ZnO films of controlled thickness and intrinsic stress state, the interaction between film-induced residual stress and microscale crack systems is systematically examined. The significant improvement of fracture toughness (165%) reveals that thin-film stress can be deliberately leveraged as an active design parameter to modify crack driving forces and enhance apparent fracture toughness in brittle micro-ceramics.

Finally, the deformation and fracture behavior of optical ceramic nanomultilayers fabricated by physical vapor deposition (PVD) is investigated, with a particular focus on the role of aperiodicity and interface architecture. By comparing optically optimized and non-optimized multilayers composed of crystalline and amorphous ceramic constituents, this work elucidates how interface density, stress redistribution, and layer sequence govern crack propagation pathways and mechanical reliability.

Together, these studies demonstrate that surface and interface engineering, through residual stress control and multilayer interface design, provides powerful, complementary strategies for overcoming the intrinsic brittleness of micro-ceramics. The insights developed in this thesis establish a mechanistic foundation for the future design of robust, coated ceramic metamaterials with tunable mechanical performance.

List of Publications

Journal papers

- **Wenjuan Cheng**, Edoardo Rossi, Jens Bauer, Jose Paolo Martins, Raphael Guillemet, Laszlo Pethö, Johann Michler, and Marco Sebastiani. "Unlocking superior fracture resistance in micro-ceramics for architected meta-materials via ALD stress engineering." Acta Materialia (2025): 121474.
- Danielle E. White, **Wenjuan Cheng**, Koushik Jagadish, Edoardo Rossi, Yu-Tsun Shao, and Andrea M. Hodge. "Deformation Behavior of Optical Ceramic Nanomultilayers: The Role of Aperiodicity." Advanced Engineering Materials (2025): e202501269.
- Margherita Cescon, Stefania Morelli, Edoardo Rossi, Daniele Duranti, **Wenjuan Cheng**, Marco Sebastiani, Paola Palmero, Elisa Fiume, Bartolomeo Coppola, Alessandro Lanzi, Luca Lusvarghi, Giovanni Bolelli. "Enhancing the CMAS resistance of YSZ thermal barrier coatings via hybrid suspension/solution precursor plasma spraying with gadolinium doping." Ceramics International (2026): 1013-1033.

Conferences

- Summer School on Experimental Nano- and Micromechanics (24-28 July, 2023, Rome)
- Machine Learning for Micromechanics Workshop (22-23 Feb, 2024, Belgium)
- Gordon Research Conference on: Structural Nanomaterials: High-Performance Structural Materials for a Sustainable Society (12-17 May, 2024, Switzerland (**poster**))
- XIV Convegno INSTM (9-12 June, 2024, Cagliari (**short oral presentation**))

- KLA User Meeting (3-4 October, 2024, Rome)
- Nanomechanical Testing in Materials Research and Development IX (6-11 October, 2024, Sicily (**poster**))
- InMa 2024 Characterization and Properties of Interface-dominated Materials (19-20 November, 2024, Germany (**oral presentation and 3rd prize for Best young scientist award**))
- Summer School on Experimental Nano- and Micromechanics in Kassel University (28 July-1 August, 2025, Germany)
- COMPLAS 2025 (2-5 September, Barcelona, Spain (**oral presentation**))
- **Visiting period** in Karlsruhe Institute of Technology, Germany, 1 June – 31 August 2025
- **Visiting period** in Montanuniversität Leoben, Austria, 15 September - 14 December, 2025

Contents

List of Figures

List of Tables

Nomenclature

ρ_{rel}	Relative density
E_{eff}	Effective stiffness
σ_{eff}	Effective strength
S	Contact stiffness
P	Load
h	Depth into surface
h_c	Contact depth
h_a	Depth of the contact plane from the free surface
$h_{\max}$	Total depth at maximum load
ϵ	Intercept factor
$A(h_c)$	Projected contact area
θ	Semi-angle
α	Effective cone angle
β	Geometry correction factor
E_r	Reduced modulus
ν	Poisson's ratio
ν_i	Poisson's ratio of indenter
E	Elastic modulus
E_i	Elastic modulus of indenter
H	Hardness
F_0	Imposed harmonic force amplitude
z_0	Imposed displacement amplitude
ω	Excitation angular frequency
ϕ	Phase lag between force and displacement during measurement
m	Effective mass of the system
K_s	Supporting spring stiffness
D_i	Instrument damping
K_f	Frame stiffness
D_s	Sample damping
ν_f	Poisson's ratio of film
E_f	Elastic modulus of film
t	Film thickness
ν_s	Poisson's ratio of substrate

E_s	Elastic modulus of substrate
ν_c	Poisson's ratio of the composite
E_c	Elastic modulus of the composite
H_f	Hardness of film
H_s	Hardness of substrate
H_c	Hardness of the composite
σ_f	Fracture strength
γ_s	Surface energy (energy per unit newly created surface area)
a	Half-length of a through-thickness crack
γ_p	Plastic dissipation per unit crack surface area
G	Energy released per unit increase in crack area
σ_{ij}	Stress tensor
$f_{ij}(\theta)$	Angular function
K	Stress intensity factor
G_c	Critical energy release rate for crack propagation
K_c	Critical stress intensity factor (fracture toughness)
a_c	Equivalent contact radius between indenter and sample
c	Radius of indentation crack
σ	Effective tensile stress driving crack opening
P_c	Critical load at failure
γ	Geometry-dependent coefficient from FEM
R	Radius of micropillar for splitting
α_f	Thermal expansion coefficients of the film
α_s	Thermal expansion coefficients of the substrate
T_D	Deposition temperatures
T_M	Room temperatures
φ	Variation in splitting load

CHAPTER 1

Introduction

1.1 | Micro-metamaterials

Micro-metamaterials are architected solids whose mechanical response is governed predominantly by geometry rather than solely by composition. Through the deliberate design of unit-cell topology, connectivity, and hierarchy, these materials can exhibit combinations of stiffness, strength, and deformation modes that are inaccessible in conventional bulk materials. Recent advances in micro-fabrication have enabled the realization of three-dimensional micro-architectures with unprecedented geometric freedom, opening the door to ultralight, mechanically robust, and functionally programmable materials for structural, optical, and energy applications.

1.1.1 Architected materials: concept and significance

Architected materials are solids whose effective mechanical performance arises primarily from their engineered geometry rather than from the intrinsic properties of the constituent material alone. In contrast to monolithic materials, where stiffness and strength are governed directly by composition and processing, architected systems exploit the topology, connectivity, and relative density of their structural units to achieve mechanical responses that are inaccessible in homogeneous solids. Classical cellular-solid theory [1] establishes that key mechanical properties follow geometry-driven scaling laws of the form

$$E_{eff} \propto \rho_{rel}^{m} \tag{1.1}$$

$$\sigma_{eff} \propto \rho_{rel}^{n} \tag{1.2}$$

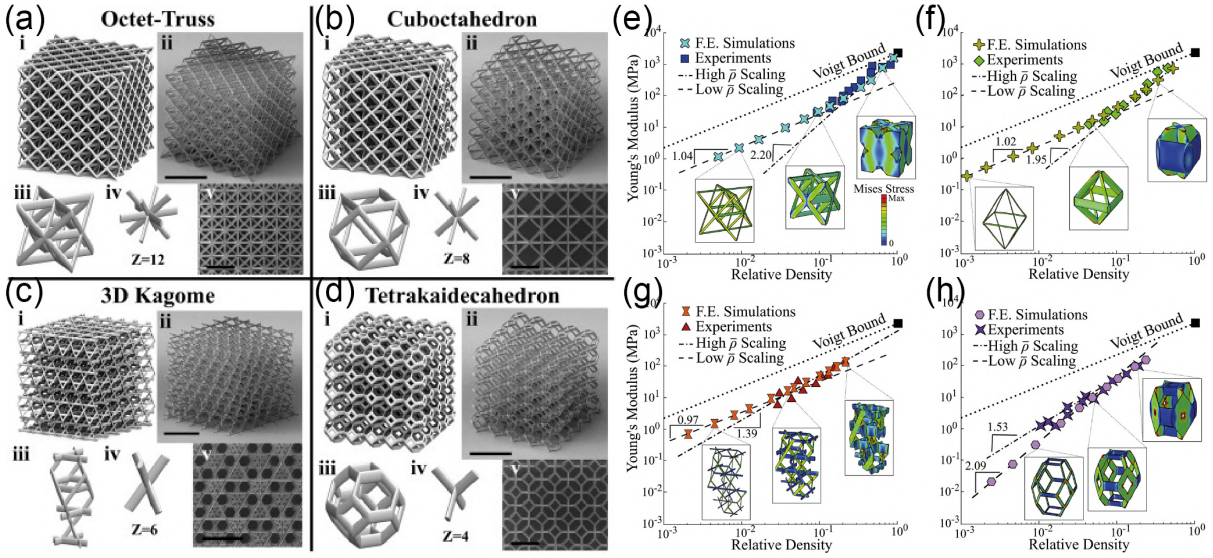

Fig. 1.1. Comparison of nanolattice topologies and their mechanical scaling behavior. (a–d) Architected lattice geometries—octet-truss, cuboctahedron, 3D Kagome, and tetrakaidecahedron—showing CAD models, nodal connectivity, and SEM images of fabricated structures (scale bars: $10\,\mu\text{m}$ in (ii), $5\,\mu\text{m}$ in (v)). (e–h) Young's modulus versus relative density for the corresponding solid-beam nanolattices, comparing finite-element (FE) predictions with experiments. Insets illustrate von Mises stress distributions under compression, highlighting topology-dependent load-bearing modes [3].

where E_{eff} and σ_{eff} denote effective stiffness and strength, ρ_{rel} is the relative density, and the exponents m and n strongly depend on the deformation mode of the underlying architecture ($m = n = 1$ for stretching dominated structure and $m = 2, n = 1.5$ for bending dominated structures [2]). The proportionality constants embed the constituent-material properties, such as its Young's modulus, yield strength, and intrinsic fracture resistance.

These relationships demonstrate the extent to which structural topology and nodal connectivity can dictate global performance. As shown in the Figure 1.1, the effective stiffness of octet-truss, cuboctahedral, 3D Kagome, and tetrakaidecahedral lattices follows distinct scaling trajectories, with stretching-dominated architectures approaching the Voigt upper bound and non-rigid geometries transitioning toward bending-dominated behavior at low densities [3]. Such geometric control enables the design of ultralight materials with high specific stiffness and strength, or with targeted deformation modes such as auxeticity, recoverable elasticity, or enhanced energy absorption [4–8].

While geometry dictates the scaling laws and deformation mechanisms, the constituent material remains fundamentally important: it sets the upper bounds on achievable stiffness, strength, and especially fracture toughness. Architected materials therefore do not eliminate

dependence on material properties; rather, they enable the decoupling of geometry-driven mechanical response from material-intrinsic behavior, allowing each to be tailored more independently than in conventional solids. This geometry–material interplay forms the basis of mechanical metamaterials, where topology is used to encode functionalities such as anisotropy, recoverability, and programmable failure modes [9, 10].

In this sense, architected materials provide a powerful route for performance optimization, via topology, hierarchy, and relative density, while still being fundamentally constrained by the mechanics of their constituent phases. This principle naturally motivates the following sections, which examine how micro-scale fabrication and surface/interface engineering further expand the accessible design space for high-performance ceramic micro-metamaterials.

1.1.2 Micro-scale fabrication of 3D architected structures

The emergence of micro-scale architected materials has been made possible by advances in high-resolution fabrication techniques capable of producing three-dimensional structures with sub-micron precision. Whereas traditional lattice materials were historically constrained to millimeter- or centimeter-scale features, often limited by manufacturing tolerances and geometric imperfections, modern microfabrication methods enable structures whose characteristic dimensions approach or even fall below the intrinsic flaw sizes of brittle solids. This shift to the micro-scale dramatically alters the accessible mechanical behavior and unlocks design opportunities not available in conventional architected systems.

Among the various fabrication routes, two-photon polymerization direct laser writing (TPP-DLW) has emerged as the most versatile platform for constructing complex three-dimensional architectures with feature sizes down to $100\,\mathrm{nm}$. Figure 1.2 represents the theory of the two photon polymrization and the set up of a typical TPP system [11]. TPP-DLW relies on nonlinear absorption of a tightly focused femtosecond laser beam within a photosensitive resin, allowing polymerization to occur only at the focal volume [11, 12]. As illustrated in Figure 1.2c, by rastering the laser in three dimensions, arbitrary freeform structures can be written voxel by voxel. This technique supports a broad range of lattice topologies, including truss-based, shell-based, woven, and hierarchical networks, and offers nearly unconstrained geometric freedom compared with planar lithographic processes. Additionally, the precise

control of the lattice geometry feature can be achieved by tuning the printing parameter such as laser power or scan speed [13–15].

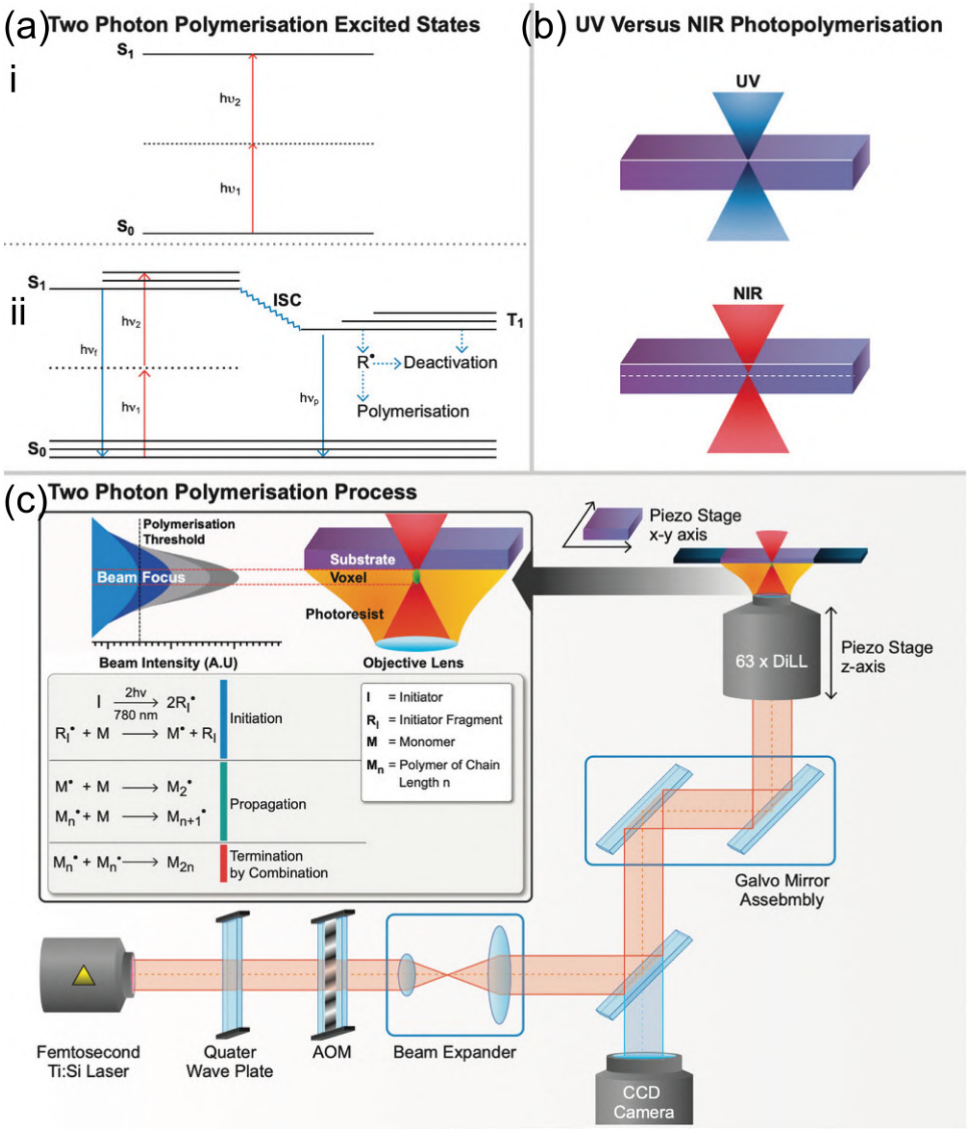

Fig. 1.2. Overview of two-photon polymerization: (a) (i) Two-photon absorption leading to electronic excitation via the simultaneous absorption of two photons through a short-lived virtual intermediate state. (ii) Initiation of the TPP process, illustrating the competing pathways for radical generation (R•), including emissive routes, fluorescence (hv_f) and phosphorescence (hv_p), which are shown by solid blue lines, and non-emissive routes indicated by dashed blue lines. (b) Comparison of UV and NIR photopolymerization: UV irradiation exhibits shallow penetration with strong surface interaction (top), whereas NIR irradiation enables deeper penetration with minimal surface interaction (bottom) (c) Schematic of the TPP system configured for printing in dip-in laser lithography (DiLL) mode with galvo mirror system and piezo stage controlling the beam path. [11]

Representative micro-architected structures fabricated by TPP-DLW demonstrate the breadth of accessible design space, as illustrated in Figure 1.3. Meza et al. [16] reported hollow-beam ceramic nanolattices with relative densities near 10^{-3} and ultrahigh specific strengths,

enabled by shell-buckling–dominated deformation at nanometer-scale wall thicknesses. Bauer and co-workers [17] achieved gigapascal-level strengths and recoverability in glassy-carbon octet lattices, highlighting the role of nanoscale flaw tolerance. More recently, Crook et al. [18] demonstrated plate-based carbon architectures in which curved plates mitigate stress concentrations, enabling improved damage tolerance. Together, these studies showcase how nanoscale geometry amplifies mechanical performance far beyond bulk material limits. Triply periodic minimal surface (TPMS) architectures, such as gyroid and Schwarz-type lattices, spinodal have also been fabricated with sub-micron resolution, exhibiting uniform stress distribution and high energy absorption [19, 20]. Re-entrant and auxetic lattices created via DLW enable extreme negative Poisson's ratios and programmable anisotropy [6]. More complex geometries, including woven micro-lattices [21] and tensegrity frameworks [22], further illustrate the versatility of the technique and highlight the ability of TPP-DLW to create architectures that would be impossible using any conventional microfabrication method.

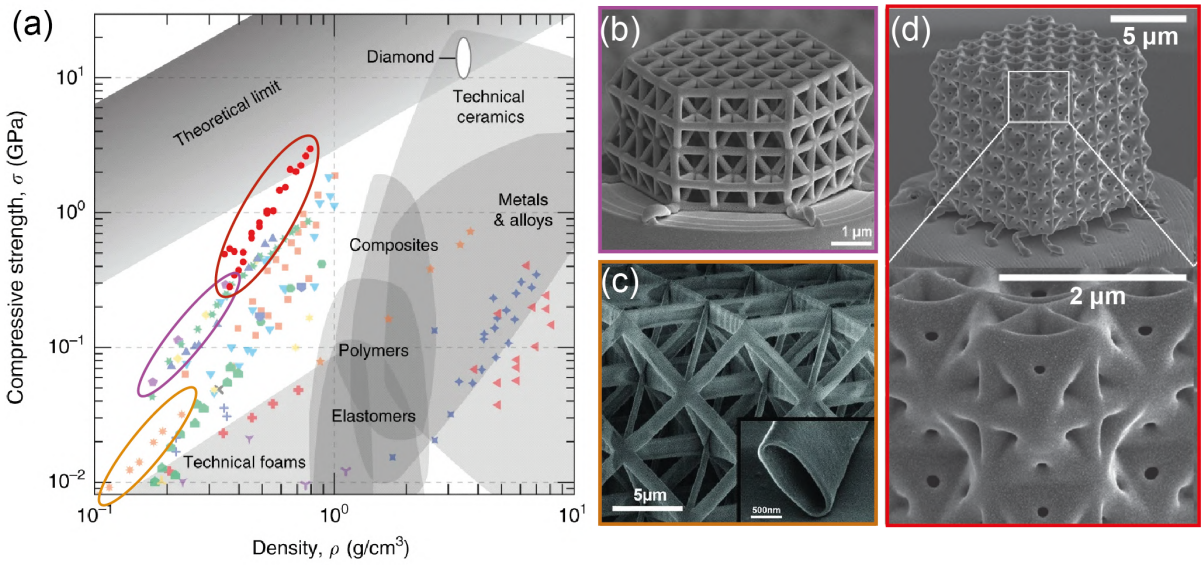

Fig. 1.3. (a) Compressive strength–density Ashby chart and representative micro-architected nanolattice structures: (b) glassy-carbon octet-truss nanolattice [17]; (c) Al_2O_3 hollow-beam octet nanolattice [16]; (d) glassy-carbon cubic–octet plate-nanolattice [18], demonstrating the potential of micro-metamaterials to expand the materials property space.

Because TPP-DLW is inherently a polymerization-based technique, the as-written architectures are polymeric and require post-processing to achieve ceramic, carbon, or metallic functionality. Several established conversion routes allow preservation of topology while enabling a broad palette of constituent materials. For example, direct pyrolysis of silicon-containing

photoresists yields polymer-derived ceramics such as SiOC or silica-like networks, with isotropic shrinkage that retains architectural fidelity [23, 24]. Metal nanoparticle–loaded resins can be written directly and subsequently sintered to form metallic-based micro-lattices [25–27].

Beyond chemical conversion, thin-film coating routes, such as atomic layer deposition (ALD), physical vapor deposition (PVD), electroless plating, or electrodeposition, provide a complementary pathway to generate ceramic or metallic shells on polymer scaffolds. These techniques offer nanometer-scale control of wall thickness and interface quality, enabling hollow-beam, core–shell, and multilayer architectures that substantially broaden the accessible material space for micro-architected structures. For example, ultrathin ALD Al_2O_3 coatings have been widely used to transform polymer and carbon scaffolds into conformal ceramic shells [17, 28, 29], while electroless plating allows uniform metallization of non-conductive DLW templates [30], yielding nickel or copper micro-lattices with continuous shell coverage. Together, these coating-based pathways expand the accessible material palette beyond polymer-derived ceramics and metals obtained by direct pyrolysis, enabling architected structures whose geometry is defined by DLW but whose composition is selected independently.

In summary, the combination of TPP-DLW with post-processing and coating strategies has transformed architected materials from conceptual designs into experimentally realizable micro-structures with unprecedented control over geometry, feature size, and constituent material composition. These advances make it possible to systematically probe mechanics at scales where structural design and intrinsic material size effects both play crucial roles. This coupling between geometry, fabrication, and material physics provides the foundation for the size-dependent mechanical phenomena examined in the next subsection.

1.1.3 Deformation and fracture mechanisms in architected micro-metamaterials

Architected micro-metamaterials derive their mechanical response from the interplay between geometry and constituent material behavior. As established in the previous sections, topology dictates the global deformation mode, while advances in micro-scale fabrication now allow these architectures to be realized with sub-micron fidelity. Reducing the characteristic feature size into the micro- and nano-scale not only enhances geometric precision but also places

the structural elements (struts, shells, plates) into a regime where flaw populations diminish and size-dependent strengthening becomes significant. These developments fundamentally alter how micro-architected materials deform and fail, making it essential to understand their deformation and fracture mechanisms.

1.1.3.1 Geometry-controlled deformation modes

The typical stress-strain curves of stretching- and bending-dominated cellular materials were summarized by Ashby, as shown in Figure 1.4 [31]. In stretch-dominated lattices, deformation is governed primarily by axial loading of the struts. After an initial elastic regime, these structures typically experience either plastic buckling or brittle collapse, often accompanied by a distinct post-yield softening regime during which the apparent stiffness becomes negative. By contrast, bending-dominated lattices tend to collapse at an approximately constant stress once the elastic limit of individual beams is reached, at which point cell edges yield, buckle, or fracture. In both cases, the final densification stage appears after extensive cell collapse. Importantly, for a given relative density, the modulus and initial collapse strength of stretching-dominated lattices are significantly higher than those of bending-dominated architectures. This makes stretch-dominated structures ideal for lightweight load-bearing applications, whereas bending-dominated systems are better suited for energy absorption.

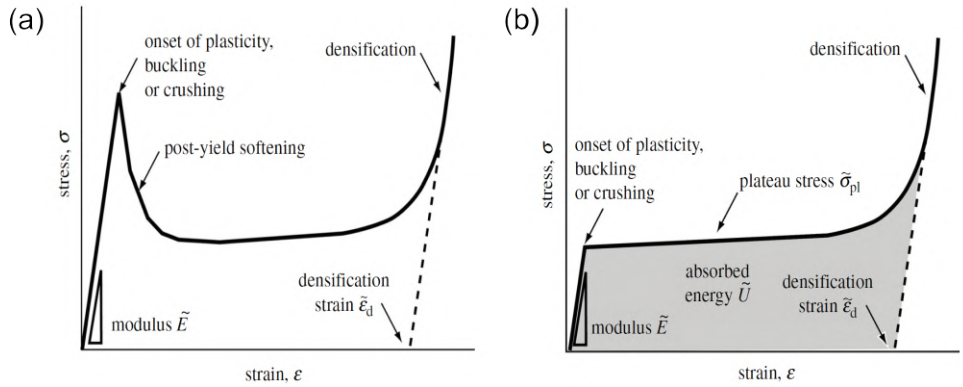

Fig. 1.4. (a) A schematic stress–strain curve for a stretch-dominated structure. It has high stiffness and high initial strength. (b) A stress–strain curve of a bending dominated lattice.

In practice, deformation behavior is also influenced by slenderness of the load-bearing members and by the mechanical properties of the constituent material. Meza and co-workers [3, 32] demonstrated that lattices with high slenderness ratios (i.e., long and thin struts, low relative density) tend to deform through beam buckling, whereas reducing slenderness

(increasing strut diameter or relative density) shifts the response toward yielding- or fracture-dominated behavior. Moreover, ductile constituents are more likely to exhibit a plateau regime associated with plastic deformation at nodes or joints, while brittle constituents undergo catastrophic collapse once the local fracture strength of a strut or node is exceeded.

A similar dependence on geometry is observed in hollow-tube lattices. Their deformation is strongly affected by the aspect ratio of the hollow cross-section [33, 34]. As wall thickness decreases, the collapse mechanism transitions from material fracture to elastic shell buckling, effectively shifting the behavior from "brittle-like" to more "ductile-like" responses [33]. As shown in Figure 1.5, a nanolattice with a wall thickness of $120\,\mathrm{nm}$ exhibits large displacement bursts corresponding to brittle layer-by-layer collapse. In contrast, a thinner $60\,\mathrm{nm}$ -wall structure displays a much smoother stress–strain response, with progressive, non-catastrophic shell buckling dominating the deformation process.

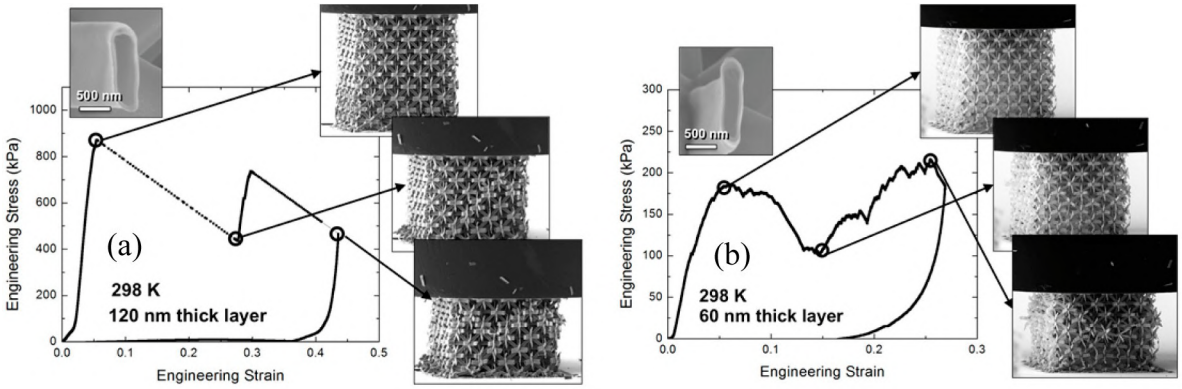

Fig. 1.5. Engineering stress–strain curve of hollow $Cu_{60}Zr_{40}$ nanolattices with the wall thickness of (a) $120\,\mathrm{nm}$ and (b) $60\,\mathrm{nm}$ at $298\,\mathrm{K}$. Insets include the cross-section of hollow member and snapshots during mechanical deformation [33].

1.1.3.2 Fracture behavior of the architected metamaterials

Beyond global deformation modes, recent studies have increasingly focused on understanding how classical fracture mechanics principles translate from continuum solids to architected lattice materials, with particular emphasis on flaw tolerance and topology-dependent toughness [35–41]. As illustrated in Figure 1.6, architected metamaterials may be viewed as discrete networks of struts or shells, whose fracture behavior represents a structural extension of classical fracture mechanics [40]. The local failure process zone is governed by the buckling, yielding, or fracture of individual struts near the crack tip. Although the classical linear elastic fracture

mechanics (LEFM) framework provides a useful conceptual guide, the actual failure processes in micro-architected lattices involve complex interactions between stress concentrations, unit-cell topology, deformation modes, and size-dependent material behavior. A full discussion of continuum fracture mechanics is given in Chapter 1.3.2.1. Here we focus on how fracture manifests within architected networks.

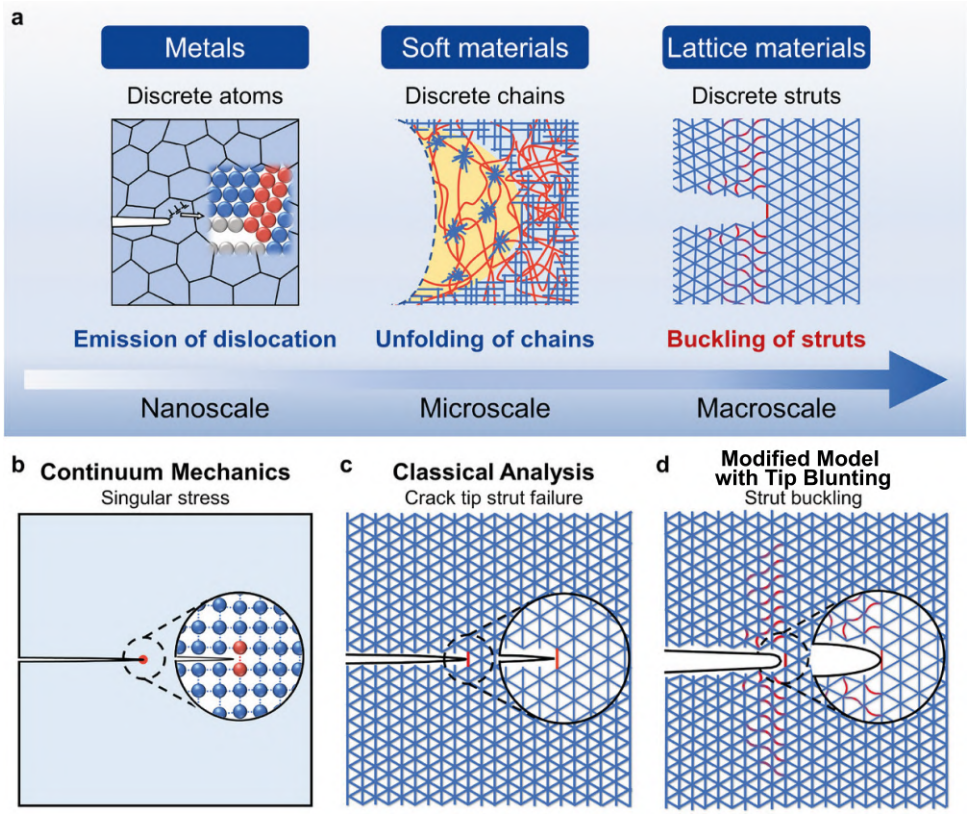

Fig. 1.6. Fracture behavior in discrete architected lattices. (a) Schematic illustrating the crack-blunting phenomenon in discrete materials across different scales. (b) Classical LEFM stress singularity. (c) Classical analysis of discrete lattice metamaterial fracture, limited to a single strut at the crack tip. (d) Modified model incorporating nonlocal buckling and crack-tip blunting, adapted from Wang et al [40].

One notable characteristic of architected micro-lattices is their insensitivity to externally introduced flaws. Montemayor et al. demonstrated that hollow Al_2O_3 nanolattices containing prefabricated notches (with notch-to-width ratios $a/w \lesssim 0.3$) fail at nearly the same load as unnotched specimens [35]. Failure did not initiate at the prefabricated notch but rather at intrinsic node-level stress concentrations, indicating that crack-like defects are not the dominant factor controlling strength in such architectures. Beyond flaw tolerance, several studies have demonstrated topology-enabled toughening in architected systems. For instance, Maurizi et al. [37] used compact-tension nano-architected specimens containing octet unit

cells and showed that these lattices possess significantly higher effective toughness than their macroscopic counterparts. This enhancement arises from distributed deformation within struts, progressive cracking, and dissipation mechanisms not captured in conventional LEFM scaling.

Beyond truss lattices, recent studies have revealed even more pronounced toughening in shell- and plate-based architected materials. Schwarz-P shell lattices exhibit substantially higher peak loads and dramatically increased energy absorption relative to octet lattices of similar relative density [38]. The topology distributes stresses efficiently, activates larger volumes of material into the high-stress regime, and enhances both plastic and nonrecoverable elastic dissipation, resulting in a significantly enlarged fracture process zone and superior fracture resistance.

1.1.3.3 Local deformation and failure

While the global deformation of architected metamaterials is governed primarily by topology and the associated load-path distribution [42], the onset of failure is dictated by local mechanical response within individual structural elements. Under external loading, stresses concentrate at a small subset of struts, shells, or nodes, typically at junctions or geometric curvature maxima, where local slenderness, wall thickness, and material properties determine whether these elements undergo elastic buckling, yielding, shell instability, or brittle fracture. Once initiated, such localized failure events perturb the surrounding stress field and may trigger cascading collapse or global instability.

Many jobs have focused on understanding and manipulating local deformation to enhance the failure resistance of architected lattices. The stretching-dominated octet lattice, for example, is known for its high stiffness and yield strength, while it exhibits layer-by-layer failure once the peak load is reached (Figure 1.7a). These discrete damage bursts correspond to struts in locally stressed regions reaching their buckling or fracture thresholds. Because the octet topology concentrates stresses at nodes, local failures tend to be spatially localized and can precipitate premature loss of load-carrying capacity. Bauer et al. proposed a tensegrity metamaterials which are composed of discontinuous compression members connected through a continuous tensile network, exhibit inherently delocalized deformation [22]. As illustrated in Figure 1.7a, deformation is distributed homogenously across the lattice and remains insensitive to the

applied strain level. Without early localization of damage in individual struts, the structure resists catastrophic collapse up to densification, yielding exceptional energy absorption.

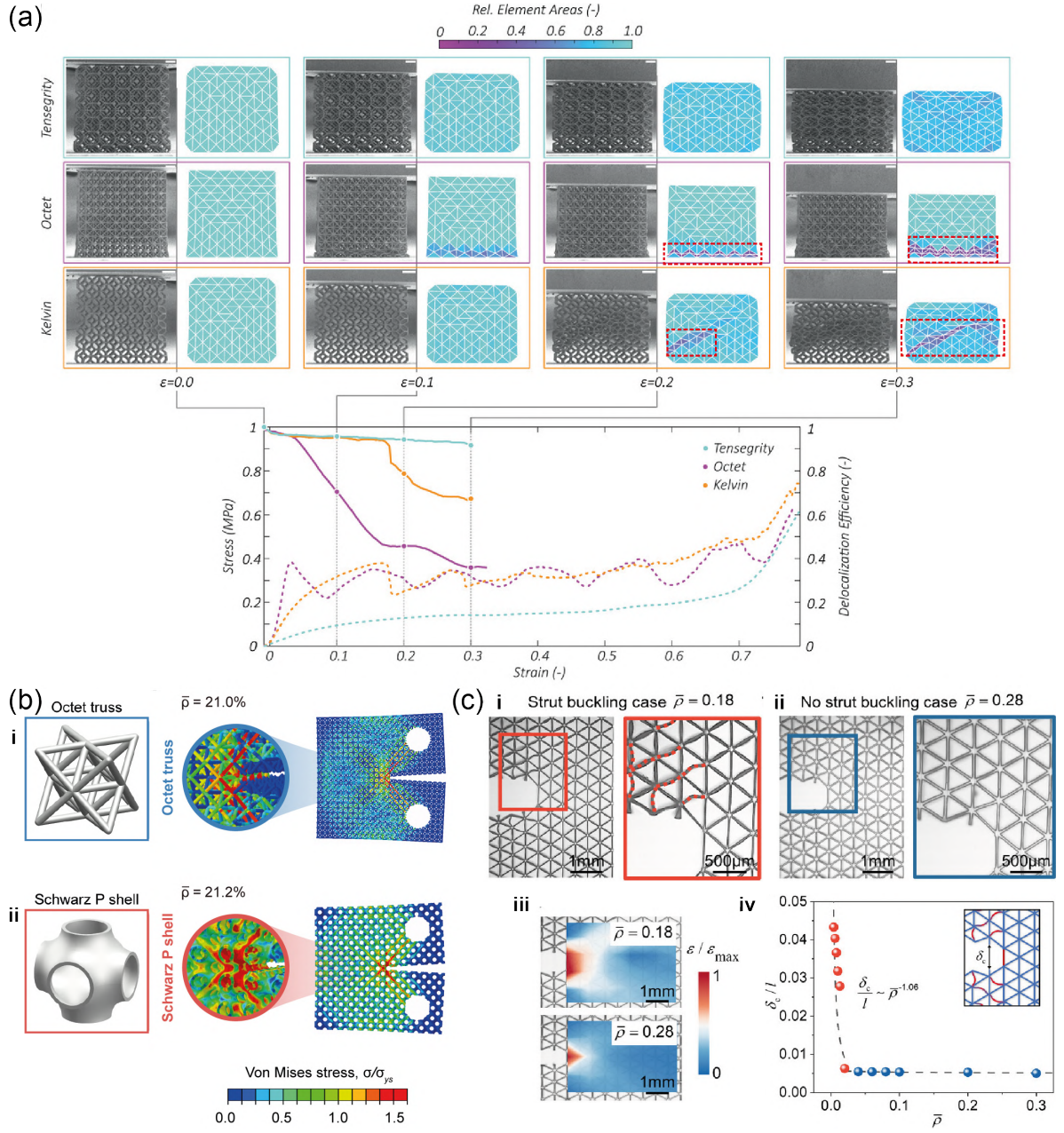

Fig. 1.7. (a) Uniaxial compression response of 4%-relative-density tensegrity, octet, and Kelvin lattices. In situ imaging and deformation maps reveal distinct deformation modes: the tensegrity lattice exhibits highly uniform, delocalized deformation over the full strain range, consistent with its stable stress–strain response, whereas octet and Kelvin lattices develop strongly localized deformation and damage, leading to abrupt load drops and instability. [22]. (b) FEM predictions of von Mises stress prior to fracture for octet truss and Schwarz-P shell lattices at comparable relative densities (~21%). The octet truss shows pronounced stress concentrations in struts and nodes, while the Schwarz-P shell distributes stress more uniformly across the shell network [38]. (c) Effect of strut buckling on fracture: buckling near the crack tip promotes strain delocalization and crack blunting, whereas the absence of buckling leads to highly localized deformation. Correspondingly, buckling-enabled lattices achieve significantly larger critical crack-tip opening displacements (CTOD) [40].

A different form of local-failure mitigation is provided by shell-based metamaterials, such as the Schwarz-P minimal-surface lattice. Rather than delocalizing deformation, the smooth curvature of the shell geometry homogenizes the stress field within each unit cell. As shown in Figure 1.7b, the absence of sharp stress concentrations suppresses premature element failure, leading to markedly higher fracture resistance [38].

Local deformation can also enable toughening under crack-tip loading. Wang et al. recently revealed that strut buckling in the crack-tip region of low-density lattices contributes to enhanced crack-tip opening displacement (CTOD), effectively blunting the crack and delaying propagation [40]. As shown in Figure 1.7c, slender struts are more prone to buckle near the crack tip than thicker ones, and this nonlocal buckling transformation leads to higher CTOD values, providing a structural toughening mechanism distinct from classical LEFM.

In summary, global topology determines how loads flow through an architected lattice, but local failure is ultimately governed by the intrinsic behavior of individual elements subjected to concentrated stresses. Both aspects, topology-driven stress distribution and material-controlled local failure, offer pathways to improve metamaterial performance. For example, the microalloyed medium-entropy (MEA)-polymer composite nanolattice fabricated through TPPDLW followed by PVD coating exhibits ultrahigh toughness and cyclability [43]. In-situ compression tests on both coated pillars and full octet lattices show that the $30\,\mathrm{nm}$ MEA film can deform by global wrinkling without cracking, verifying that the enhanced lattice-level toughness originates from the local ductility and stability of individual coated struts (Figure 1.8).

Building on these insights, the present work adopts an approach that isolates individual constituent elements to directly probe their intrinsic mechanical behavior, as illustrated in Figure 1.9. Such an element-level understanding is essential for predictive modeling of local failure and, ultimately, for the rational design of tough and reliable architected metamaterials. Guided by this perspective, the primary characterization methods employed in this study are introduced in Chapter 1.3 , followed by a detailed outline of the research activities in Chapter 1.4.

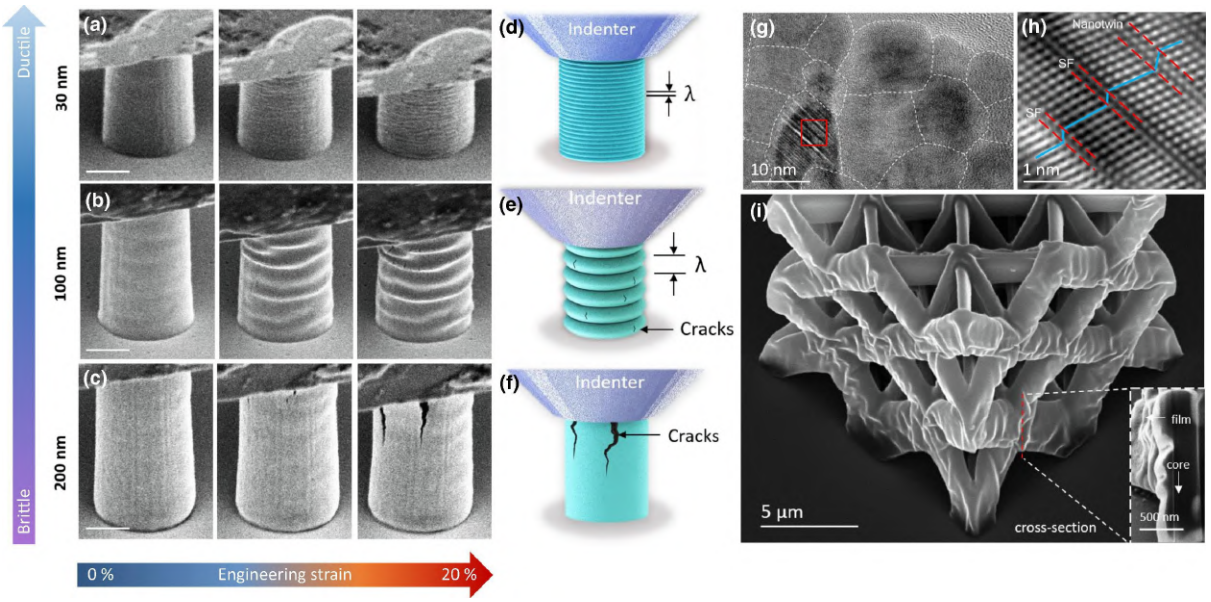

Fig. 1.8. In situ compression tests on MEA-coated pillars and corresponding microstructural characterization. (a–c) SEM images showing the deformation behavior of pillars coated with $30\,\mathrm{nm}$, $100\,\mathrm{nm}$ and $200\,\mathrm{nm}$ MEA films at several loading stages up to 20% strain; (d–f) Schematic illustrations of the corresponding composite nanolattice responses, highlighting a pronounced brittle-to-ductile transition as the MEA film thickness decreases. Scale bars: $2\,\mu\mathrm{m}$. (g) TEM image of a representative $30\,\mathrm{nm}$ MEA coating. (h) Inverse fast Fourier transform (IFFT) image of the boxed region in (g), revealing nanotwins and stacking faults within the ultrathin film; (i) SEM image of a wrinkled nanolattice after deformation, showing joint plastic deformation of the MEA shell and polymer core without interfacial delamination; inset: cross-sectional view of a deformed strut [43].

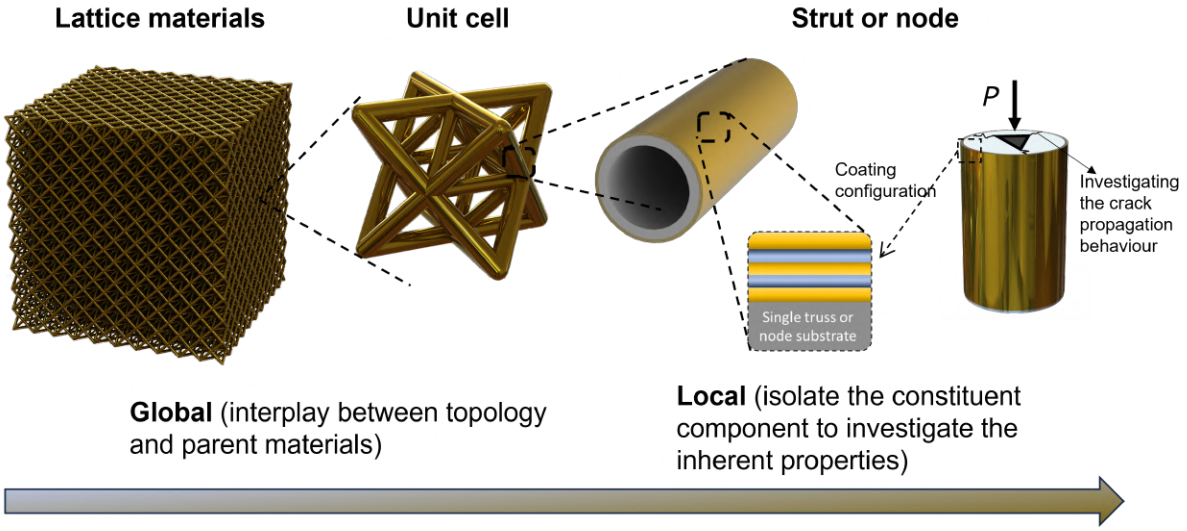

Fig. 1.9. Schematic illustrating the progressive simplification of architected metamaterials across multiple length scales. Complex lattice architectures (left) exhibit global deformation and failure governed by topology and load-path connectivity. At finer resolution (middle), individual unit cells and representative struts or shells determine local stress concentrations and element-level failure modes. At the smallest scale (right), single struts or node-level specimens isolated from the lattice enable direct probing of intrinsic material behavior, such as size effects, buckling, yielding, and fracture, without the complexity of architectural interactions.

1.2 | Surface engineering for enhanced micro-ceramic performance

Surface engineering has become a critical design strategy in the development of nano- and micro-architected metamaterials. As highlighted in Chapter 1.1.3, the mechanical response of metamaterials originates from the coupled contributions of topology and constituent material properties. In the present work, the topology is not the primary variable of interest; instead, attention is directed toward isolated micro-scale struts and pillars, which serve as model building blocks for probing fundamental failure mechanisms, as demonstrated in Figure 1.9. Within such isolated components, modifications to the constituent material, particularly within the near-surface region, can strongly reshape the effective mechanical response.

This is especially relevant in micro-ceramic systems, where the surface-to-volume ratio becomes significant and the characteristic dimensions of the structural members approach the intrinsic flaw sizes of brittle materials. Under these constraints, the near-surface region should therefore be regarded not only as a boundary condition but as a mechanically influential zone controlling stress concentration and fracture processes [44]. As a result, surface engineering provides an additional, geometry-dependent tuning parameter for tailoring the toughness, strength, and deformation behavior of micro-architected ceramics.

Surface modification techniques, particularly thin-film deposition routes such as atomic layer deposition (ALD) [45–50] and physical vapor deposition (PVD) [33, 34, 51–55], have therefore become indispensable tools for enhancing and controlling the performance of micro-architected lattices. Numerous studies on coated nano- and microlattices have demonstrated improvements including increased stiffness, enhanced recoverability, higher compressive strength, and elevated flaw tolerance under tension. These observations provide strong motivation for a systematic investigation of how surface treatments interact with the intrinsic brittleness of micro-ceramics and how they can be deliberately engineered to improve mechanical reliability.

1.2.1 Atomic layer deposition

1.2.1.1 Process fundamentals

ALD operates through a vapor-phase, self-limiting reaction mechanism that enables atomic-scale control of coating thickness together with exceptional conformality on complex three-dimensional micro-architectures [56], as illustrated in Figure 1.10. In a typical ALD cycle, gaseous precursors are introduced sequentially into the reaction chamber, each reacting solely with available surface functional groups rather than with previously deposited material. For example, during Al_2O_3 ALD using trimethylaluminum (TMA) and water, the first precursor pulse enables TMA to chemisorb onto surface hydroxyl (–OH) groups, releasing methane as a byproduct [57]. After purging the chamber, a water pulse reacts with the remaining $–CH_3$ ligands, regenerating surface hydroxyl sites and completing a single monolayer-equivalent reaction step. Because each reaction step proceeds only until surface reactive sites are saturated, the amount of material deposited per cycle, typically on the order of ≈ 1 Å, is governed by surface chemistry rather than deposition time.

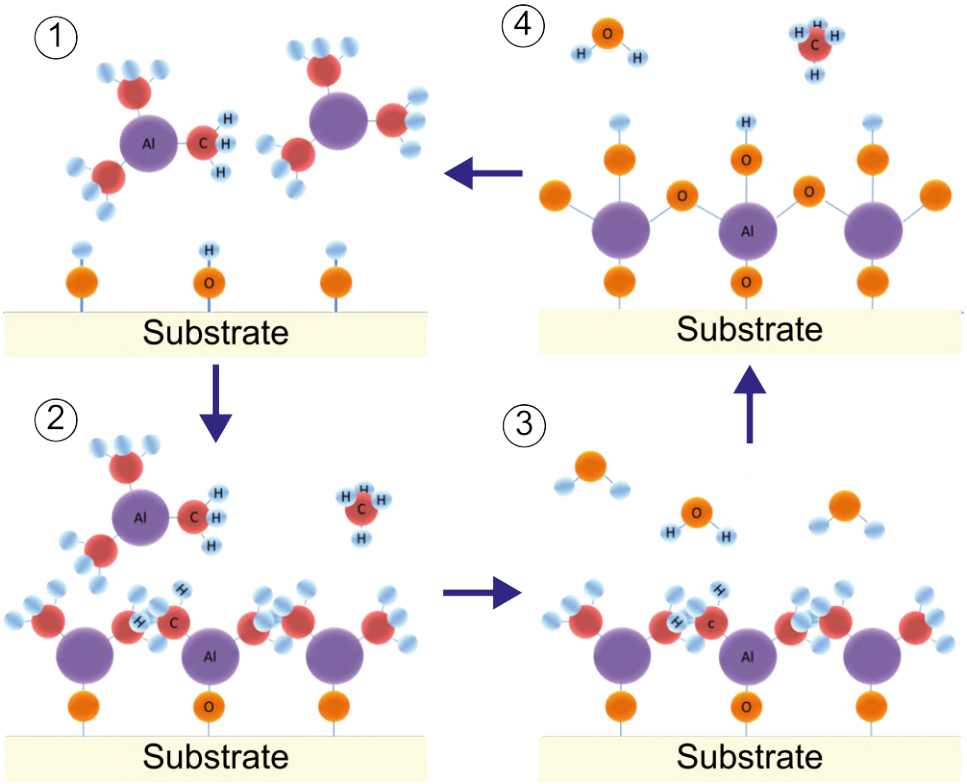

Fig. 1.10. Schematic illustration of the Al_2O_3 ALD process using trimethylaluminum (TMA) and water (H_2O) as precursors.

Through repeated pulse–purge cycles, ALD builds ceramic films in a layer-by-layer manner, producing amorphous or nanocrystalline oxides and nitrides with thicknesses typically in the nanometer scale on nano- and micro-lattice scaffolds. This self-limiting nature of ALD is critical for achieving highly uniform coatings across high-aspect-ratio struts, internal cavities, and tortuous geometries that are inaccessible to conventional line-of-sight deposition methods [58].

Beyond thickness control, ALD process parameters, including growth temperature, precursor chemistry, plasma assistance, and substrate bias, have pronounced effects on film density, crystallinity, residual stress state, and mechanical properties [57, 59–61]. For ALD Al_2O_3, systematic studies have shown that films grown from TMA and H_2O typically exhibit tensile residual stresses on the order of hundreds of megapascals, with the magnitude of tensile stress decreasing strongly with increasing deposition temperature (Figure 1.11b).

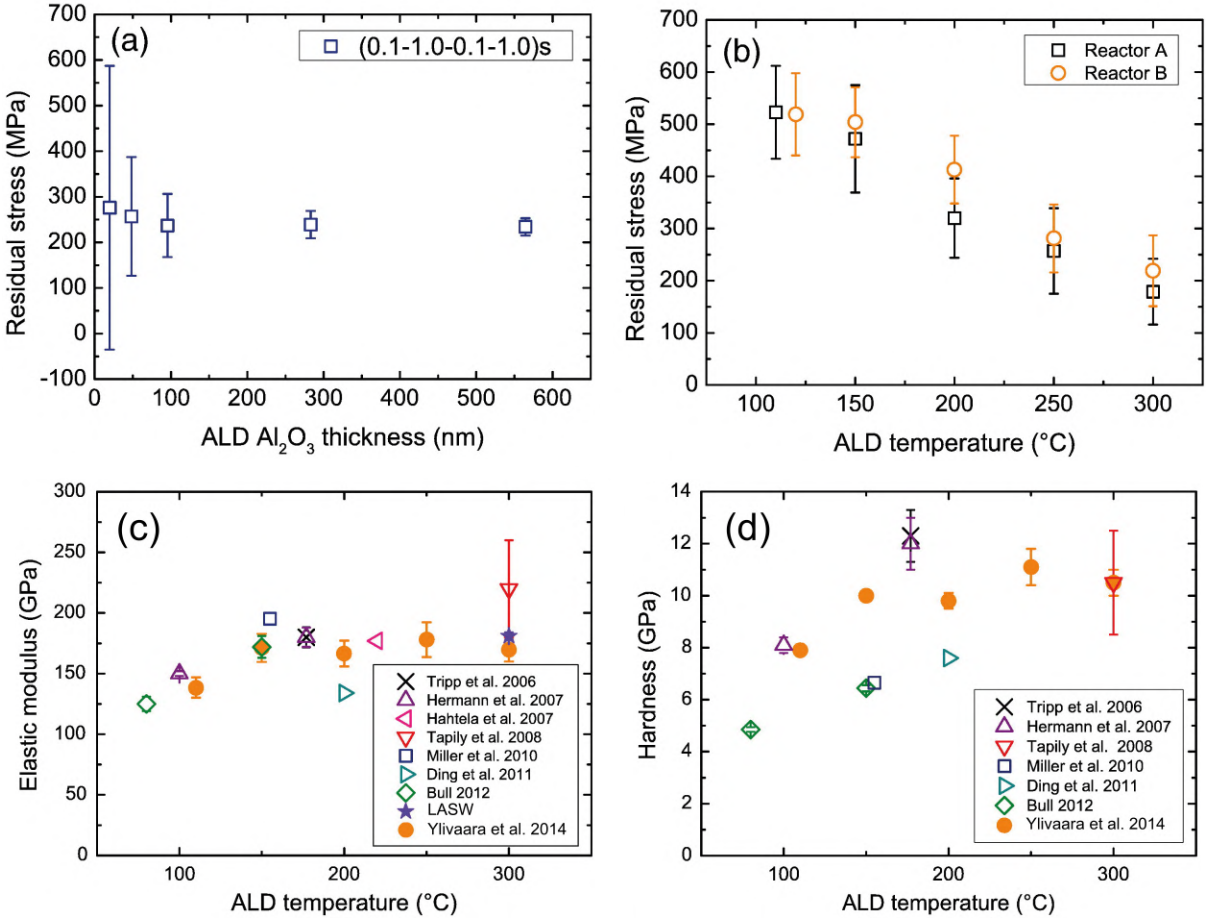

Fig. 1.11. The residual stress of the ALD Al_2O_3 as a function of (a) film thickness (deposited at $300\,^{\circ}\mathrm{C}$) and (b) growth temperature ($100\,\mathrm{nm}$ film thickness). The symbols present average stress values and bars present calculated maximum error values. Comparison of (c) elastic modulus values and (b) hardness for ALD Al_2O_3 with published values among various deposition temperature. Reproduced from Ylivaara et al's work [57].

Simultaneously, the elastic modulus and hardness increase with growth temperature as the film densifies and transitions from a relatively porous low-temperature structure toward a more tightly bonded oxide network, and then reach the constant value above $150\,^{\circ}\mathrm{C}$. The plasma in PE-ALD of Al_2O_3 promotes more complete surface reactions and enhances film densification of Al_2O_3, leading to reduced residual stress levels compared with those in thermally grown films [62], providing an additional degree of freedom for stress-state engineering. These characteristics establish ALD not only as a geometric coating technique but also as a powerful tool for tailoring intrinsic film stress and mechanical response.

1.2.1.2 ALD in architected materials

The integration of ALD coatings into nano- and micro-architected materials has enabled substantial advances in mechanical performance, particularly in hollow-beam and core–shell lattice systems. Numerous studies have demonstrated that conformal ALD coatings can transform polymeric or pyrolyzed scaffolds into mechanically robust ceramic architectures with precisely defined shell thickness and highly reproducible mechanical behavior [3, 16, 17, 28, 45–50].

For instance, as shown in Figure 1.3c, ultralight octet lattices fabricated with $10\,\mathrm{nm}$-thick ALD Al_2O_3 shells exhibit a rare combination of high stiffness, high strength, and pronounced energy absorption, while simultaneously recovering their original shape after compressive strains exceeding 50% [16]. By systematically tuning the shell thickness-to-radius ratio, these hollow ceramic nanolattices transition from catastrophic brittle fracture to a deformation mode dominated by elastic shell buckling, enabling a ductile-like structural response despite the intrinsically brittle nature of alumina. In this case, the deformation is primarily governed by the stability and collapse of a thin, stiff ceramic shell, with minimal contribution from a load-bearing core.

When combined with hierarchical architectures, as illustrated in Figure 1.12, ALD-grown Al_2O_3 layers further enable the fabrication of multi-order hollow and core–shell metamaterials that exhibit suppressed brittle failure and enhanced recoverability [47]. In these systems, two distinct deformation mechanisms may coexist. For purely hollow ceramic hierarchies, the response remains shell-dominated and governed by elastic buckling and progressive shell

collapse. In contrast, for Al_2O_3–polymer core–shell composites, the deformation is instead controlled by the mechanical mismatch between the stiff, brittle ceramic shell and the compliant, ductile polymer core. Here, load transfer, interfacial shear, and progressive polymer yielding play central roles, leading to fundamentally different failure and energy-dissipation mechanisms compared to those of hollow ceramic shells.

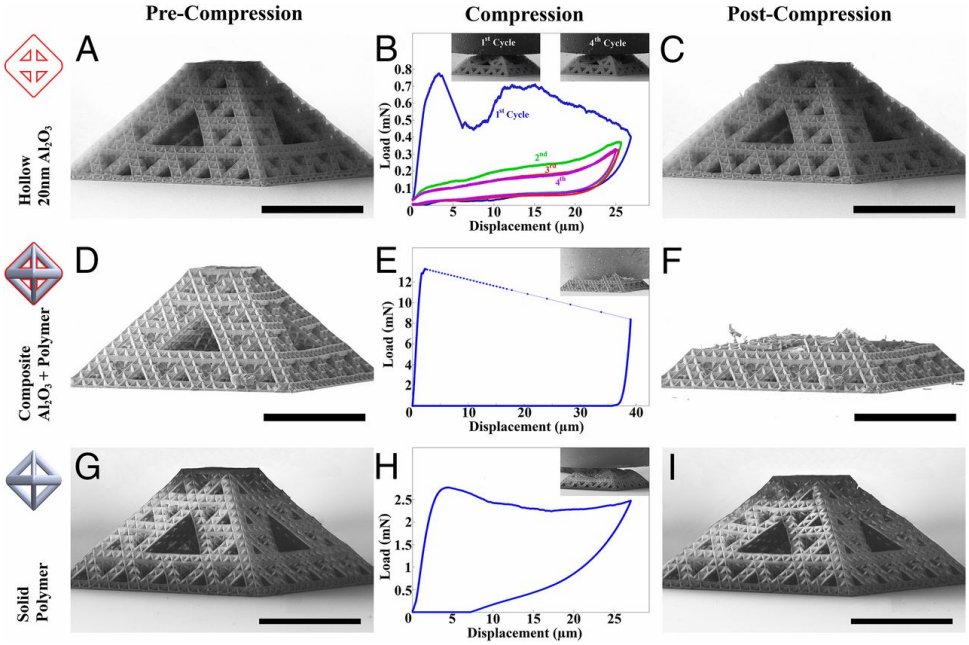

Fig. 1.12. An example of ALD-coated polymer microlattices with different structural configurations under compression. (a) Hollow Al_2O_3 lattice with a shell thickness of $20\,\mathrm{nm}$ before compression. (d) Composite lattice consisting of a polymer scaffold coated with $20\,\mathrm{nm}$ Al_2O_3 prior to compression. (g) Solid polymer lattice before compression. (b), (e), and (h) Corresponding load–displacement curves of the hollow Al_2O_3 lattice, the Al_2O_3–polymer composite lattice, and the polymer lattice, respectively. The hollow Al_2O_3 lattice was subjected to cyclic compression up to 50% strain, whereas the composite and polymer samples were compressed to 65% and 50% strain, respectively. Insets show the samples at the maximum applied strain. (c), (f), and (i) Post-compression images of the hollow Al_2O_3, composite, and polymer lattices corresponding to (a), (d), and (g), respectively. Scale bars: $50\,\mu\mathrm{m}$. [47]

Transforming three-dimensionally written polymer microlattices into glassy carbon nanolattices via pyrolysis and subsequently reinforced them with thin ALD Al_2O_3 coatings [17] further illustrated that alternative material combinations are able to reshape these mechanisms. In contrast to Al_2O_3–polymer composites, both the glassy carbon core and the alumina shell are stiff and brittle solids with comparable elastic moduli and strengths at the nanoscale. As a result, the glassy carbon–alumina architectures deform through a collective brittle-shell-dominated mode, rather than through a soft-core–hard-shell coupling mechanism. With strut diameters on the order of $200\,\mathrm{nm}$, these structures achieved material strengths approaching the

theoretical strength of glassy carbon (2–3 GPa), while the additional $10\,\mathrm{nm}$ alumina coating further modified the load distribution and failure stresses without fundamentally altering the underlying brittle deformation character, as shown in Figure 1.13.

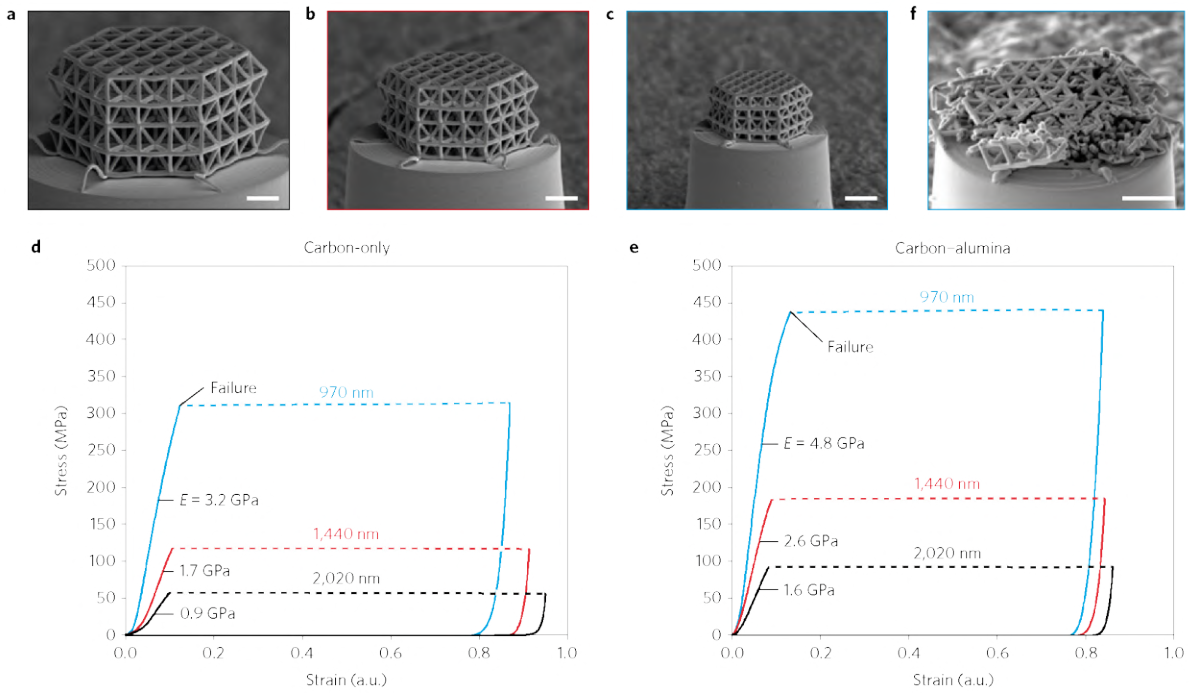

Fig. 1.13. Compression experiments of pyrolysed lattices with tetrahedral unit cells. a–c, SEM images of carbon lattices with strut lengths of (a) $2020\,\mathrm{nm}$, (b) $1440\,\mathrm{nm}$ and (c) $970\,\mathrm{nm}$, with relative density to be 12.5 %, 15.9 %, 25.2 %, respectively. (d) Stress–strain curves showing that strength and stiffness increase with decreasing dimensions, the abrupt increase of strain with dash line showing the brittle failure of the lattice. (e) Stress–strain curves for lattice structures with the same dimensions, reinforced with $10\,\mathrm{nm}$ Al_2O_3 coatings applied by ALD; strength and stiffness are enhanced further compared to the corresponding carbon-only structure shown in (d). (f) SEM micrograph of a fractured carbon-only structure (strut length: $970\,\mathrm{nm}$), showing mostly brittle failure. All scale bars are $2\,\mu\mathrm{m}$. [17]

Together, these examples demonstrate that ALD-enabled architected materials do not follow a single universal deformation or toughening pathway. Instead, distinct combinations of shell thickness, hierarchy, and constituent material pairing—ranging from hollow brittle ceramics, to brittle–ductile composites, to brittle–brittle hybrid systems—activate fundamentally different deformation and failure mechanisms. These mechanism-level differences ultimately govern whether a structure exhibits recoverability, energy absorption, ultrahigh specific strength, or structural robustness, thereby defining the application space of ALD-engineered micro- and nanolattices.

1.2.2 Physical vapor deposition

1.2.2.1 Process fundamentals

Physical vapor deposition (PVD) refers to a class of vacuum-based coating techniques in which solid source materials are physically transformed into vapor-phase species and subsequently condensed onto a substrate surface. In contrast to ALD, which relies on self-limiting surface chemistry, PVD processes are governed by line-of-sight transport of energetic atoms, ions, or clusters. Common PVD techniques employed for architected micro- and nanostructures include magnetron sputtering, electron-beam evaporation, and thermal evaporation [63, 64].

In magnetron sputtering, as illustrated in Figure 1.14, a plasma, typically formed in an argon atmosphere, is used to accelerate Ar^+ ions toward a negatively biased target material. Momentum transfer during ion bombardment ejects target atoms, which then propagate through the vacuum chamber and condense on the substrate to form a thin film. The kinetic energy of the arriving species, together with substrate temperature and background pressure, governs the resulting film density, microstructure, crystallinity, and residual stress state [65].

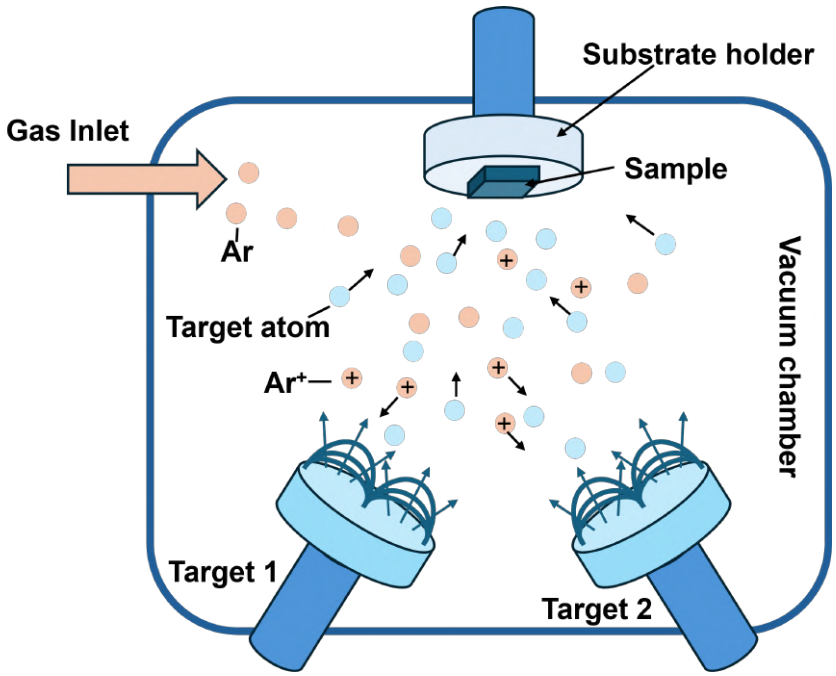

Fig. 1.14. The schematic exhibiting the magnetron sputtering

Compared to ALD, PVD generally offers higher deposition rates and significantly broader materials compatibility, encompassing ceramic oxides and nitrides, metals or alloys, and complex multilayer stacks. This versatility has enabled the widespread use of PVD for functional coatings across structural, electronic, and architected material systems.

A key advantage of PVD lies in its exceptional flexibility in alloy design. By co-sputtering from multiple targets or employing pre-alloyed targets, binary, ternary, and multicomponent alloys can be deposited with precisely controlled composition, enabling the synthesis of medium-entropy alloys (MEAs) and high-entropy alloys (HEAs) [43, 52–54, 66]. These studies have demonstrated that PVD-deposited HEA and MEA coatings enable architected lattices to overcome the conventional strength–recoverability trade-off by activating synergistic deformation mechanisms between a compliant polymer core and a high-strength metallic shell. This core–shell coupling promotes shell-dominated strengthening while preserving elastic recoverability through stable buckling and reversible deformation of the polymer scaffold.

However, because material transport during PVD proceeds predominantly along straight-line trajectories, conformal coating of high-aspect-ratio or deeply recessed micro-architectures is inherently limited by geometric shadowing. As illustrated in Figure 1.15, coating thickness typically decreases from the exterior surfaces toward interior struts, resulting in systematic thickness gradients within the structure [51, 55]. While such shadowing effects restrict full conformity, they can also introduce spatially varying material distributions that may be exploited to tailor stiffness and further modulate the mechanical response of architected lattices.

Importantly, advances in deposition configuration, including substrate rotation, target arrangement, and process parameter optimization, have been shown to substantially improve coating uniformity on complex three-dimensional architectures. For example, Feng et al. demonstrated that careful control of sputtering geometry enables relatively uniform deposition of multicomponent alloy coatings on 3D-printed polymer lattices, thereby combining architectural design freedom with the unique compositional versatility of PVD [43]. Together, these examples underscore the strength of PVD as a surface-engineering technique when material selection, alloy complexity, and multilayer design are prioritized over strict geometric conformity.

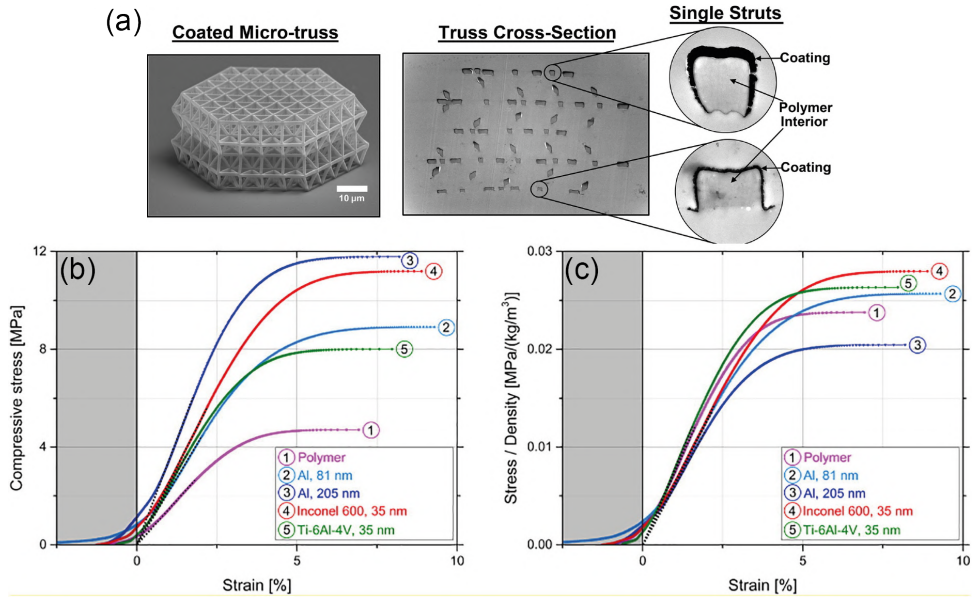

Fig. 1.15. (a) SEM image of a polymer micro-truss structure coated by magnetron sputtering, together with a microtome-prepared cross-section of the coated truss and representative cross-sections of individual struts, highlighting the nonuniform coating thickness arising from the line-of-sight (shadowing) effect inherent to PVD. (b) Representative uniaxial compression stress–strain responses of uncoated polymer and metal-coated micro-truss structures with different coating materials and thicknesses (Al: 81 and $205\,\mathrm{nm}$; Inconel 600: $35\,\mathrm{nm}$; Ti-6Al-4V: $35\,\mathrm{nm}$). (c) Corresponding compressive stress normalized by density (specific stress) as a function of strain. Metal coatings significantly enhance the absolute strength and stiffness of the micro-truss structures, while the specific mechanical response depends on both the coating material and thickness. [55]

1.2.2.2 Multilayer ceramic coatings and micro-mechanical effects

Although PVD is inherently limited in achieving fully conformal coatings on complex three-dimensional architectures, it offers exceptional flexibility in coating design, particularly for the fabrication of nanoscale ceramic multilayers with precisely controlled layer sequence, composition, and aperiodicity [67–69]. By alternately sputtering different ceramic targets, multilayers composed of oxides, nitrides, or their combinations can be synthesized with individual layer thicknesses ranging from a few nanometers to several tens of nanometers. At these length scales, the resulting high density of internal interfaces becomes a dominant factor governing mechanical behavior.

Extensive studies on PVD-deposited ceramic multilayers, including TiN/AlN and TiN/CrN systems, have demonstrated that heterointerfaces fundamentally alter deformation and fracture pathways compared to monolithic films [69–74]. Elastic modulus mismatch between adjacent layers redistributes stress at the nanoscale, while differences in bonding strength, crystallinity,

and defect density promote crack deflection, crack bifurcation, or interfacial delamination rather than straight-through crack propagation [75]. As a consequence, fracture resistance in multilayer ceramics becomes governed by crack–interface interactions across successive layers, rather than by the intrinsic toughness of any single constituent phase.

Beyond simple crack deflection, enhanced fracture resistance in PVD-fabricated ceramic multilayers arises from deliberately introduced spatial heterogeneity in mechanical properties across the coating thickness. Experimental studies on TiN/AlN and TiN/CrN multilayers have consistently shown that such heterointerfaces disrupt straight-through crack propagation, leading to crack branching, stepwise fracture, and distributed damage accumulation [70–73]. Consistent with these observations, Daniel et al. demonstrated through microcantilever bending experiments that alternating layers with pronounced differences in elastic modulus or fracture strength modify the local crack driving force as a crack traverses the multilayer stack [69]. When a crack propagating in a stiff, brittle layer encounters a more compliant or weaker constituent, the elastic energy release rate is reduced, promoting crack arrest or deflection instead of catastrophic failure.

Importantly, the dominant toughening mechanism depends on the nature of the mechanical contrast between adjacent layers. In systems such as TiN/SiO_x, elastic modulus mismatch between crystalline and amorphous layers governs crack–interface interactions, whereas in TiN/CrN or CrN/Cr multilayers with comparable elastic moduli, differences in intrinsic fracture strength play a more significant role [69, 75]. These findings establish spatial heterogeneity in mechanical property distributions—rather than crystallographic incoherence alone—as a general and robust toughening strategy in ceramic multilayers.

Residual stresses further modulate these interface-driven mechanisms in substrate-bound coatings. Differences in intrinsic growth stress and thermal expansion mismatch between adjacent layers generate alternating tensile and compressive stress fields that locally alter the effective stress intensity factor at the crack tip [69, 75]. While Daniel *et al.* isolated intrinsic material effects using stress-relaxed freestanding microcantilevers, their results suggest that residual stress gradients in attached multilayers can act synergistically with elastic and strength contrasts to further suppress unstable crack propagation.

Extending these concepts beyond periodic architectures, aperiodic multilayer sequences introduce nonuniform interface spacing and non-repeating stress fields that disrupt preferred fracture planes. By forcing cracks to repeatedly re-nucleate, deflect, or arrest at interfaces with varying mechanical contrast, aperiodic multilayers promote distributed deformation and progressive failure rather than abrupt fracture [76]. This interface-dominated and architecture-sensitive mechanical response provides the foundation for the investigations presented in Chapter 4.

1.3 | Microscale mechanical characterization strategies

Accurate evaluation of the mechanical behavior of micro-ceramics requires test methods capable of probing small, spatially confined volumes. Conventional bulk-scale techniques are often unsuitable at these dimensions, motivating the use of microscale approaches such as nanoindentation and indentation-based fracture testing. Nanoindentation enables reliable measurement of elastic modulus and hardness within micron-sized regions, while advanced indentation strategies, including indentation cracking and micro-pillar splitting, provide access to local fracture toughness even in complex or heterogeneous materials. Together, these methods form a comprehensive toolbox for characterizing the mechanical response of micro-structured ceramics. As mentioned in the Chapter 1.2, surface engineering explores a broader materials space for architected metamaterials. Meanwhile, it introduces an additional parameter, residual stress in the film, to tune the performance of the coated systems, which requires a precise measurement of the stress level within tens of nanometer thin films.

1.3.1 Evaluation of elastic modulus and hardness via nanoindentation

Nanoindentation is essentially an indentation test performed at nanometer-scale penetration depths, where the residual impressions are typically only a few micrometers in size, which is too small to be measured accurately by conventional optical methods. Consequently, the projected contact area is determined indirectly by the penetration depth of the indenter rather

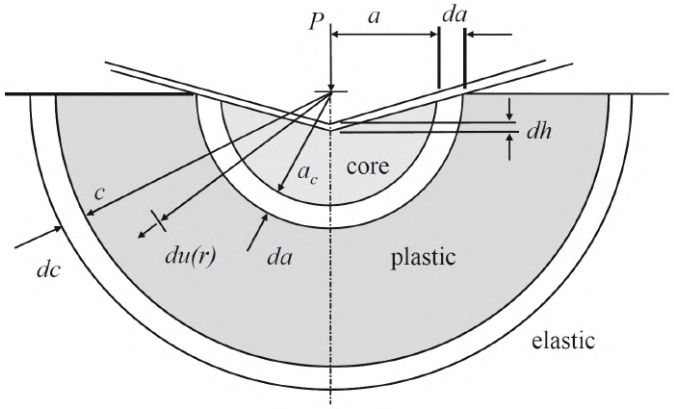

Fig. 1.16. Expanding cavity model schematic. The contacting surface of the indenter is encased by a hydrostatic "core" of radius a_c that is in turn surrounded by a hemispherical plastic zone of radius c. An increment of penetration dh of the indenter, results in an expansion of the core da and the volume displaced by the indenter is accommodated by radial movement of particles $du(r)$ at the core boundary. This in turn causes the plastic zone to increase in radius by an amount dc [79].

than by post-mortem imaging. Beyond hardness, modern nanoindentation techniques enable the extraction of a variety of mechanical properties, including elastic modulus, strain-hardening behavior, fracture toughness in brittle materials, and time-dependent viscoelastic response. In the following, only the aspects relevant to this work, such as the fundamentals of contact mechanics and the continuous stiffness measurement (CSM) technique, are briefly reviewed.

1.3.1.1 Contact mechanics and the Oliver–Pharr method

Modern nanoindentation analysis is based on the elastic contact solution originally developed by Sneddon for axisymmetric indenters [77], and later generalized by Oliver and Pharr to accommodate self-similar pyramidal indenters such as Berkovich and cube-corner tips [78]. The actual deformation field beneath a sharp indenter is elastic–plastic and highly heterogeneous. The stress state beneath the indenter is triaxial and evolves continuously with penetration depth, making an exact analytical description of the full stress and strain distribution intractable. Nevertheless, the contact mechanics of sharp indentation can be understood using a simplified expanding cavity model, as schematically illustrated in Figure 1.16. The region immediately beneath the indenter tip is commonly described as a highly confined, approximately hydrostatic core of radius a_c, where stresses exceed the yield strength and plastic flow is unavoidable. This core is surrounded by a hemispherical plastic zone of radius c, within which irreversible

deformation occurs under large shear stresses. Beyond the plastic zone, the material remains elastically deformed, storing elastic strain energy that is fully recoverable upon unloading [79].

This separation of deformation regimes has important implications for nanoindentation measurements. The indentation hardness primarily reflects the mean contact pressure required to sustain plastic flow within the core and surrounding plastic zone, and is therefore governed by the materials and interfaces contained within this plastically deformed volume. By contrast, the elastic response during unloading is controlled by the elastic strain field extending well beyond the plastic zone into the surrounding material. As a result, the unloading stiffness is sensitive to a much larger volume of material and can be analyzed using elastic contact solutions.

On this basis, Oliver and Pharr extended Sneddon's elastic framework to self-similar indenters by exploiting the predominantly elastic nature of the initial unloading response, enabling the extraction of elastic modulus and hardness from the measured load–displacement curve (Figure 1.17). The key idea is that the initial portion of the unloading response is predominantly elastic, permitting direct access to the contact stiffness:

$$S = \frac{dP}{dh}|_{h=h_{max}} \tag{1.3}$$

which characterizes how strongly the material resists elastic displacement under the applied load.

A central quantity in nanoindentation is the contact depth h_c, which determines the projected contact area $A(h_c)$ and thus directly influences the modulus and hardness. As illustrated in Figure 1.17a, the total penetration depth at maximum load is h_{max}, but only part of this displacement contributes to actual contact [79]. Oliver and Pharr introduced the geometric relation

$$h_c = h_{max} - h_a = h_{max} - \epsilon\frac{P}{S} \tag{1.4}$$

where the second term accounts for the elastic recovery of the surface furing unloading. The factor ϵ is an intercept factor that depends on the indenter shape (typically 0.75 for pyramidal indenters).

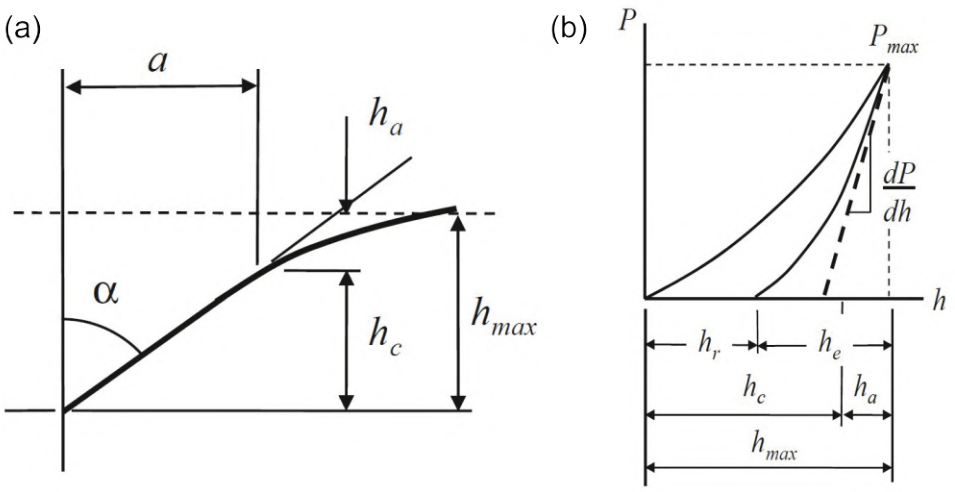

Fig. 1.17. (a) Geometry of contact with conical indenter; (b) Compliance curves, loading and unloading, from a nanoindentation experiment with maximum load P_{max} and depth beneath the specimen free surface h_{max} . The depth of the contact circle h_c and slope of the elastic unloading dP/dh allow specimen modulus and hardness to be calculated. h_r is the depth of the residual impression, and h_e is the displacement associated with the elastic recovery during unloading

Once h_c is known, the project contact area $A(h_c)$ is obtained from the idealized area function of the indenter geometry. For perfect Berkovich, Vickers or cube-corner tips, analytical expressions for $A(h_c)$ are listed in Table 1.1, corresponding to the shapes shown in Figure 1.18. In real experiments, however, tip rounding, manufacturing tolerance and wear cause deviations from ideal geometry, so the area function must be calibrated using a reference material such as fused silica.

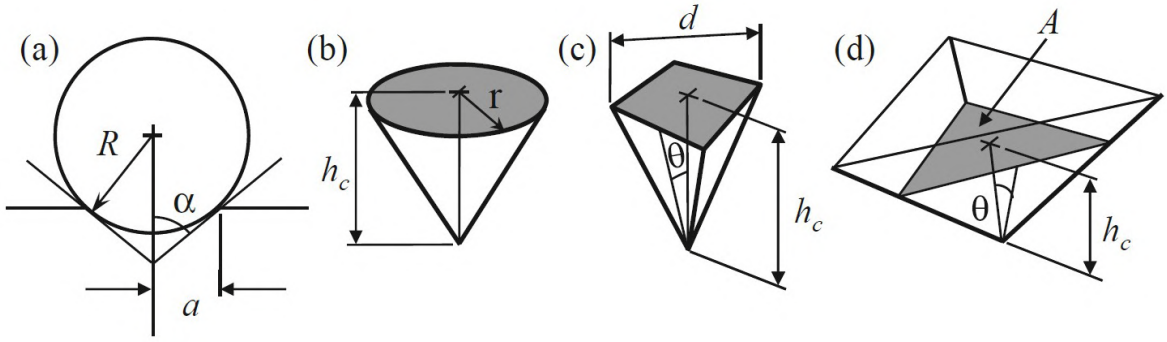

Fig. 1.18. Indentation parameters for (a) spherical, (b) conical, (c) Vickers, and (d) Berkovich indenters (not to scale)

Table 1.1
Projected areas, intercept corrections, and geometry correction factors for various types of indenters. The semi-angles given for pyramidal indenters are the face angles with the central axis of the indenter.

Indenter type	Projected area	Semi-angle θ (deg)	Effective cone angle α (deg)	Intercept factor[a] ϵ	Geometry correction factor β
Sphere	$A \approx \pi 2Rh_c$	N/A	N/A	0.75	1
Cone	$A = \pi h_c^2 \tan^2 \alpha$	α	α	0.727	1
Vickers	$A = 4h_c^2 \tan^2 \theta$	68°	70.3°	0.75	1.012
Berkovich	$A = 3\sqrt{3}\, h_c^2 \tan^2 \theta$	65.27°	70.3°	0.75	1.034
Cube corner	$A = 3\sqrt{3}\, h_c^2 \tan^2 \theta$	35.26°	42.28°	0.75	1.034

[a] The intercept factors given here are those most commonly used. The values for the pyramidal indenters should theoretically be 0.72 but a value of 0.75 better represents experimental data.

The reduced modulus E_r is computed from the contact stiffness and projected area using the Sneddon/Oliver–Pharr relation:

$$E_r = \frac{\sqrt{\pi}}{2\beta} \frac{S}{\sqrt{A(h_c)}} \tag{1.5}$$

where β is a geometry correction factor (e.g., 1.034 for Berkovich) accounting for deviations from perfect axisymmetry. The measured E_r incorporates contributions from both the indenter and the specimen:

$$\frac{1}{E_r} = \frac{(1 - \nu^2)}{E} + \frac{(1 - \nu_i^2)}{E_i} \tag{1.6}$$

where E and ν are the elastic modulus and Poisson's ratio of the sample, and E_i, ν_i are those of the diamond indenter. Because diamond is much stiffer than most materials, $(1 - \nu_i^2)/E_i$ is small, allowing accurate extraction of the specimen modulus E.

Hardness is defined analogously to traditional indentation, using the projected contact area at maximum load:

$$H = \frac{P_{max}}{A(h_c)} \tag{1.7}$$

Since hardness normalizes the applied load by the true contact area, accurate determination of $A(h_c)$ is essential.

Another important consideration is that the contact depth expression in Equation 1.4 assumes a "sink-in" deformation mode, where the material surface sinks beneath the indenter during loading. In some soft or low work-hardening materials, however, the displaced material flows outward and accumulates around the indenter edges, producing a "pile-up" morphology. In such cases, the true contact depth is larger than predicted, and can be approximated as $h_c = h_{max} + h_a$. Because pile-up leads to significant errors in the calculated contact area, and consequently in modulus and hardness, its presence must be carefully evaluated [80, 81]. This phenomenon does not play a role in the materials examined in this work and is therefore not discussed further.

1.3.1.2 Continuous stiffness measurement (CSM)

Based on the conventional Oliver–Pharr analysis determining the contact stiffness S from the initial slope of the unloading curve, Pethica and Oliver [82] introduced the continuous stiffness measurement (CSM) technique which provides a way to obtain S continuously during loading. The method superimposes a small sinusoidal displacement (or force) oscillation onto the quasi-static loading signal, as illustrated in Figure 1.19. The resulting dynamic load and displacement responses enable direct measurement of the contact stiffness at each penetration depth through:

$$S = \frac{\partial P}{\partial h}|_{elastic} \tag{1.8}$$

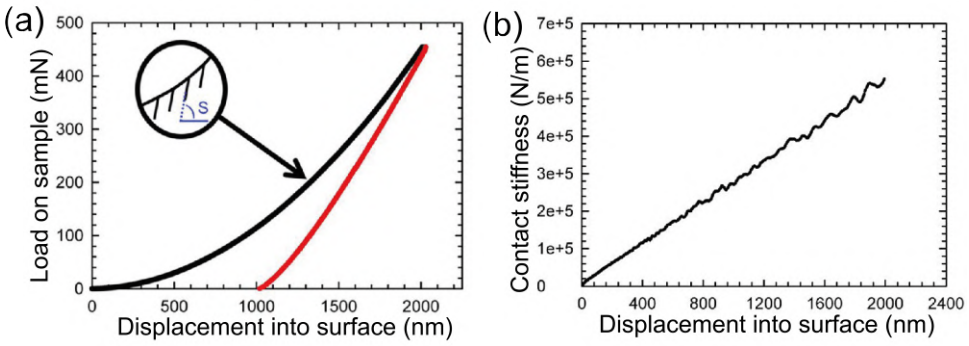

Fig. 1.19. (a) Load–displacement response with superimposed small oscillations used to probe the instantaneous stiffness; (b) continuously measured contact stiffness obtained by the CSM method.

In CSM, the indenter is driven with a harmonic force of amplitude ΔP_{CSM}, producing a displacement oscillation of amplitude Δh_{CSM} typically on the order of a few nanometers.

Because this oscillation is extremely small and applied at relatively high frequency, the deformation associated with this perturbation is essentially elastic, where plastic flow cannot evolve on the oscillation timescale. The ratio of the load and displacement amplitudes therefore provides the elastic contact stiffness directly:

$$S = \frac{\Delta P_{CSM}}{\Delta s_{CSM}} \cos\phi \tag{1.9}$$

where ϕ is the phase lag between load and displacement. For materials with predominantly elastic response (e.g. metals and ceramics at room temperature), φ is typically very small and often treated as zero, whereas time-dependent or viscoelastic behavior leads to a finite phase lag. Importantly, the dynamically measured stiffness S is the same quantity that enters the Oliver–Pharr equations (Equation 1.5) for determining modulus and hardness. CSM simply provides a more direct and depth-resolved measurement route. To interpret the oscillatory response quantitatively, the instrument and specimen can be represented by a mass–spring–damper system, as shown schematically in Figure 1.20 [83]. The measured dynamic response is governed by the combined stiffness and damping of the contact and the instrument frame. Solving the harmonic oscillator yields the relations

$$S = \left[\frac{1}{\frac{F_0}{z_0}\cos\phi - (K_s - m\omega^2)} - \frac{1}{K_f} \right]^{-1} \tag{1.10}$$

$$D_s\,\omega = \frac{F_0}{z_0}\sin\phi - D_i\,\omega \tag{1.11}$$

where F_0 and z_0 are the imposed harmonic force and displacement amplitudes, ω is the excitation frequency, m is the effective mass, K_s is the supporting spring stiffness, D_i is the instrument damping, and K_f is the frame stiffness. During a CSM test, ω, F_0, z_0, ϕ are measured or imposed, while m, K_s, and D_i are instrument-specific constants provided by calibration. The frame stiffness K_f, however, must be carefully calibrated to ensure accurate extraction of the true contact stiffness.

Once S is obtained from Equation 1.10 and 1.11, it can be directly substituted into the Oliver–Pharr formalism to compute the reduced modulus, sample modulus, and hardness as a function of depth. This capability makes CSM particularly powerful for characterizing thin films, multilayers, graded coatings, and heterogeneous microstructures. The quantity $D_s\,\omega$ additionally contains information on viscoelastic energy dissipation, though this aspect is not further discussed here.

The inclusion of the instrument dynamics here serves to underline a practical but crucial point that reliable material properties can only be obtained when instrumental compliance is accurately calibrated, the sample is securely mounted to ensure a rigid mechanical coupling, and the system exhibits stable drift behavior throughout the test. Because CSM measurements are highly sensitive to external vibration, thermal drift, and machine dynamics, proper experimental control ensures that the extracted stiffness truly reflects the specimen response. Detailed calibration and setup procedures are provided in the G200 manual [83], and once implemented, the method yields robust, material-specific results.

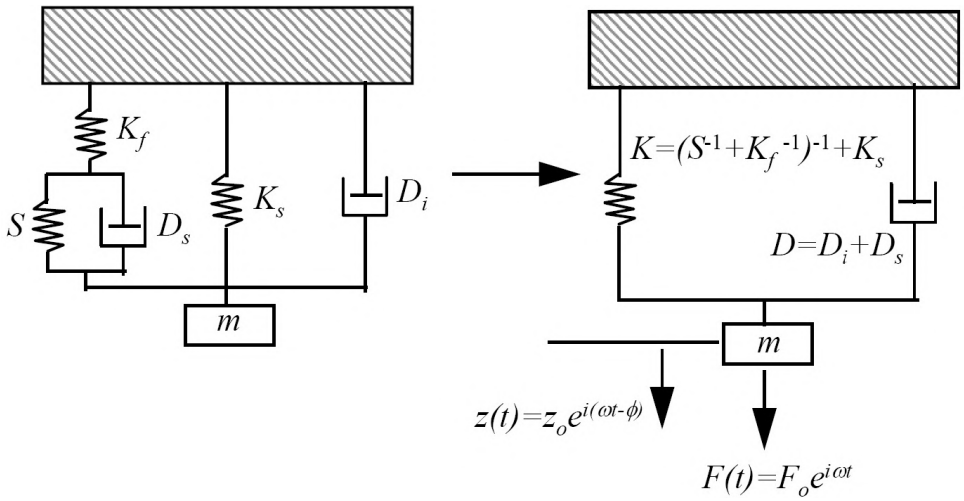

Fig. 1.20. Equivalent harmonic oscillator model describing the dynamic interaction between the specimen contact stiffness S, instrument stiffness K_s, frame stiffness K_f, and damping components.

1.3.1.3 The properties determination of thin film via CSM

As clarified above, the CSM technique provides depth-resolved measurements of stiffness and modulus, which is particularly powerful for characterizing thin films and coatings. This capability is essential for the materials studied in Chapter 3 and 4 , where mechanical properties must be evaluated within films of limited thickness. However, interpreting indentation data

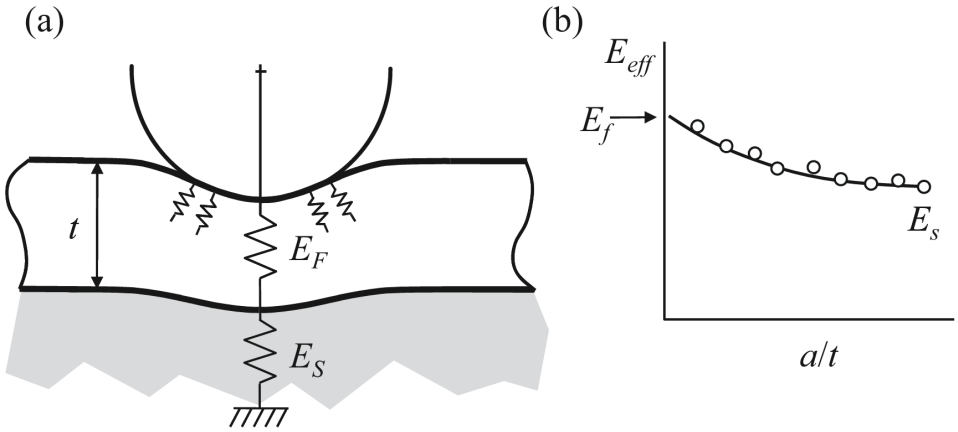

Fig. 1.21. (a) The contribution to E_{eff} from the film includes that from the localized support from the indentation stress field. (b) For a geometrically similar indenter, the indentation scales with a/t. The modulus of the film E_f is found by extrapolating measured values of E_{eff} to $a/t = 0$ [79]

from thin films is non-trivial because a film of finite thickness is supported by a mechanically distinct substrate, as illustrated in Figure 1.21. Consequently, the measured stiffness and modulus reflect the combined film–substrate response rather than the intrinsic properties of the film alone [79].

A commonly cited practical guideline is that the indentation depth should remain below approximately 10 % of the film thickness to minimize substrate effects [84–86]. In practice, this "10 % rule" is often difficult to satisfy, especially for very thin coatings or multilayer architectures. As a result, considerable effort has been devoted to developing analytical and numerical models that describe the interaction between film and substrate during indentation [87].

One of the earliest analytical approaches was proposed by Doerner and Nix [88], who introduced an exponential weighting function to account for substrate effects in the composite reduced modulus:

$$E_r = \left[\frac{1-\nu_f^2}{E_f}\left(1-e^{-\alpha t/h_c}\right) + \frac{1-\nu_s^2}{E_s}e^{-\alpha t/h_c} + \frac{1-\nu_i^2}{E_i} \right]^{-1} \tag{1.12}$$

$$\frac{1-\nu_c^2}{E_c} = \frac{1-\nu_f^2}{E_f}\left(1-e^{-\alpha t/h_c}\right) + \frac{1-\nu_s^2}{E_s}e^{-\alpha t/h_c} \tag{1.13}$$

where t is the film thickness and α is an empirical fitting constant determined from experiments on films of known properties. Subsequently, King [89] used finite-element simulations of flat cylindrical and pyramidal indenters on layered systems and modified the Doerner–Nix model by replacing the contact depth h_c with a, the square root of projected contact area A_c. With the advent of CSM, the continuous modulus–depth profile makes it possible to identify the onset of substrate influence directly rather than relying on a single unloading curve.

Taking advantage of this capability, Saha and Nix [86] analyzed the parameter P/S^2, obtained from the Oliver–Pharr framework (Equations 1.5 and 1.7):

$$\frac{P}{S^2} = \frac{1}{\beta^2}\frac{\pi}{4}\frac{H}{E_r^2} \tag{1.14}$$

which depends only on the directly measured quantities P and S and is therefore independent of tip-area calibration. For homogeneous materials, H and E_r are essentially depth-independent, so P/S^2 remains constant. For film/substrate systems, however, deviations in P/S^2 reveal the transition from film-dominated to substrate-dominated deformation. Saha and Nix showed that substrate effects can be modeled by replacing the film thickness t in King's expression with an effective thickness $(t–h)$, where h is the indentation depth. Like the Doerner–Nix model, these approaches rely on exponential weighting functions to separate the contributions of the film and substrate to the composite modulus E_c. With sufficient depth-resolved data from CSM, $E_c(h_c)$ can be fitted to Equation 1.13 to extract intrinsic film properties reliably.

Complementary to modulus models, energy-based methods have been developed to analyze the composite hardness of film/substrate systems. Korsunsky et al. [90] and Tuck et al. [91] proposed a widely used hardness model based on indentation work, expressed as:

$$H_c = H_s + \frac{H_f - H_s}{1 + \left[(h/t)/\beta_0\right]^X} \tag{1.15}$$

where H_s and H_f are the intrinsic substrate and film hardness, respectively, and β_0 and X are two fitted constants. By plotting composite hardness H_c versus $\log(h/t)$, both film and substrate hardness can be extracted. This model has been successfully applied over a

wide range of indentation scales (nano to macro) and for systems spanning hard-on-soft and soft-on-hard architectures.

Together, these analytical and semi-empirical frameworks form the theoretical basis for interpreting CSM-generated modulus and hardness data in thin films and multilayers. They are essential for extracting reliable intrinsic material properties from indentation tests where substrate effects are otherwise unavoidable.

1.3.2 Evaluation of fracture toughness via pillar splitting method

1.3.2.1 Fracture mechanics

In general, the strength of a material is defined as the maximum stress it can sustain before failure, which for a dense, defect free solid is theoretically on the order of $E/10$. In real engineering materials, however, the measured strength is always much lower due to the inevitable presence of micro cracks, flaws or voids that cause severe stress concentration [92]. Thus, beyond simply quantifying strength, it is also vital to understand how and why materials fail. Specifically, it requires insight into how cracks originate and propagate under external loads, which is essential for predicting failure, designing safer structures, and improving the reliability of engineering components.

The modern theory of fracture traces back to the pioneering work of Griffith in 1920, who first proposed that fracture in brittle solids is governed by an energy balance between the elastic strain energy released and the surface energy required to create new crack surfaces [93]. A crack of half-length a in a infinite plate under plane stress (Figure 1.22) can grow only when such growth leads to a decrease (or no net increase) in the total potential energy. This consideration yields the classical Griffith equation:

$$\sigma_f = \sqrt{\frac{2E\gamma_s}{\pi a}} \tag{1.16}$$

where γ_s is the surface energy of the material, E is the Young's modulus.

While Griffith's theory successfully describe brittle materials such as glass, it fails to account for the significantly higher fracture resistance observed in most structural metals. Irwin [94] and Orowan [95] independently extended the Griffith's expression by incorporating

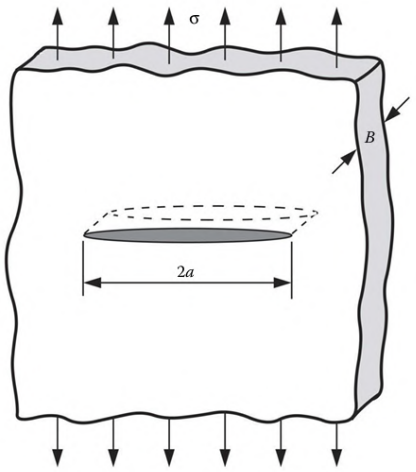

Fig. 1.22. A through-thickness crack in an infinitely wide plate subjected to a remote tensile stress.

the plastic work dissipated in the crack tip process zone. The effective surface energy thus becomes:

$$\sigma_f = \sqrt{\frac{2E(\gamma_s + \gamma_p)}{\pi a}} \tag{1.17}$$

where γ_p is the plastic work per unit new surface area, typically much larger than γ_s. In an ideally brittle solid, a crack can be formed merely by breaking atomic bonds; γ_s reflects the total energy of broken bonds pure unit surface area created. In metals, crack propagation involves not only bond rupture but also extensive dislocation activity near the crack tip, giving rise to substantial plastic dissipation.

A major conceptual advance was introduced by Irwin, who reformulated fracture using an energy-based parameter, the energy release rate, G, defined as the mechanical energy available for an increment of crack growth [96]. For an infinite plate in plane stress containing a crack of length $2a$ in Figure 1.22, the energy release rate is:

$$G = \frac{\pi\sigma^2 a}{E} \tag{1.18}$$

Irwin subsequently showed that the near-tip stresses exhibit a universal square-root singularity and introduced the stress intensity factor K, which characterizes the amplitude of

this singular field 1.23 [97],

$$\sigma_{ij} = (\frac{K}{\sqrt{2\pi r}}) f_{ij}(\theta) \tag{1.19}$$

where r and θ are polar coordinates centered at the crack tip, σ_{ij} is the stress tensor, $f_{ij}(\theta)$ are angular functions determined by the crack geometry and loading mode. For mode I loading,

$$K_I = \sigma\sqrt{\pi a} \tag{1.20}$$

The critical condition for crack extension is reached when K_I=K_c, the fracture toughness. The relationship between G_c and K_c is:

$$K_c = \begin{cases} \sqrt{EG_c} & \text{for plane stress,} \\ \sqrt{\dfrac{EG_c}{1-\nu^2}} & \text{for plane strain.} \end{cases} \tag{1.21}$$

and under plane strain deformation, the toughness is denoted K_{Ic}, which is widely accepted as an intrinsic material property.

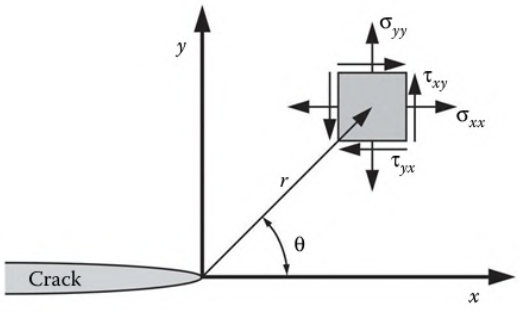

Fig. 1.23. Definition of the coordinate axis ahead of a crack tip. The z direction is normal to the page.

1.3.2.2 Indentation crack

With the advancement of fracture mechanics, sharp indentation has emerged as a powerful microscale probe not only for hardness and modulus, but also for evaluating the fracture toughness, especially in brittle materials [98–102]. Unlike conventional fracture toughness tests, indentation does not require a pre-crack. Rather, deformation-induced flaws are naturally nucleated under the complex stress fields generated beneath the indenter. Sharp contacts

produce extremely high stress gradients, and in the case of ideal elastic contact even true singularities, which are partially relieved by localized inelastic deformation.

As illustrated in Figure 1.24, the simplified elastic-plastic model proposed by Marsh [103] divides the indentation field into three characteristic regions. Immediately beneath the indenter lies an outwardly expanding "hydrostatic core" that exerts uniform pressure on the surrounding material. This core is enclosed by a "plastic region", within which material flow is governed by a yield criterion. Surrounding the plastic zone is the elastic "matrix", which deforms elastically under the applied load. It is worth noting that this model assumes a nearly spherical symmetry of the plastic boundary. However, for cone or pyramid indenters with small included angles, the plastically deformed material tend to pile up along the indenter faces, thereby breaking the symmetry.

Another important point is that the material within the plastic zone necessarily undergoes permanent deformation during a complete loading and unloading cycle. Consequently, the initial stress-free state in the surrounding elastic matrix can never be fully recovered. A residual stress field therefore remains in the unloaded material, typically containing a significant tensile component even though its distribution differs substantially from that in the fully loaded state. In practice, deformation-induced flaws tend to nucleate at points of intense stress

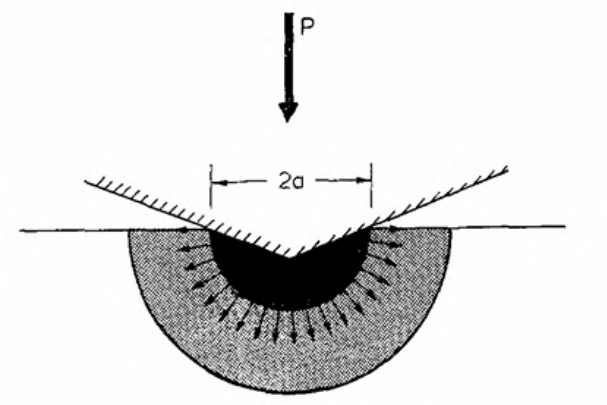

Fig. 1.24. Model for elastic-plastic indentation problem. Dark region denotes "hydrostatic core", shaded region denotes "plastic zone", and surrounding region denotes "elastic matrix".

concentration ahead of locally constrained bands or zones of inelastic deformation. Once a particular flaw reaches a critical configuration, it evolves into a dominate crack and enters a regime where Griffith's energy balance becomes applicable. During crack advance, mechanical energy released from the indentation field is converted into new surface energy. For example,

Figure 1.25 shows a typical Vickers indentation illustration the nucleation of median cracks during loading and the subsequent propagation of radial cracks upon unloading [102].

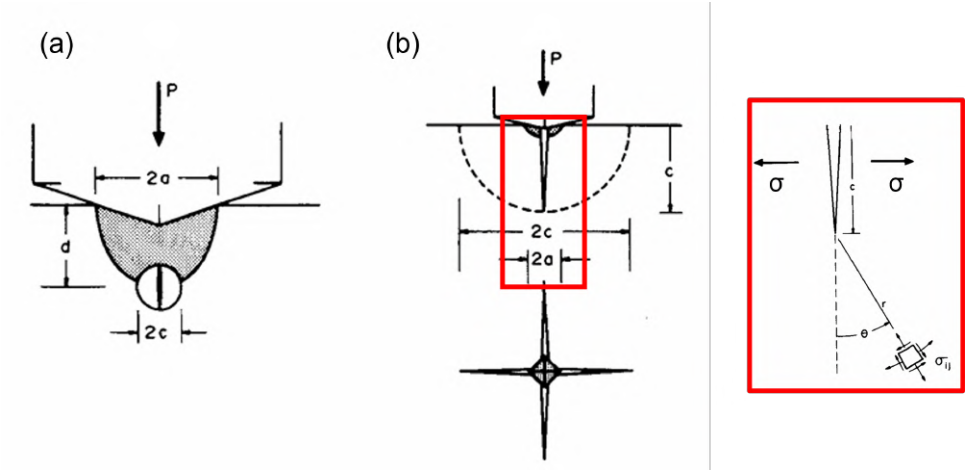

Fig. 1.25. Idealized deformation and fracture pattern for Vickers pyramid indentation, showing (a) initiation and (b) propagation of median cracks, with the inset illustrating the crack-tip stress field. The characteristic length scales a and c correspond to the deformation and fracture processes, respectively; a represents the equivalent contact radius (denoted a_c in the main text), and c is the radial crack length.

The driving force for indentation-induced crack growth is still described by the stress intensity factor [102]. In the vicinity of a crack tip, the stresses take the familiar asymptotic form

$$\sigma_{ij} = K_I g_{ij}(\theta)/\sqrt{2\pi r} \tag{1.22}$$

where the $g_{ij}(\theta)$ are angular functions defining the near-tip field. Crack advance occurs when the applied intensity K_I reaches the critical value K_c, so that K_c provides the quantitative measure of the material's fracture toughness under indentation loading.

Although the indentation stress field is highly complex, the fully developed median–radial crack system adopts a remarkably simple geometry. Once the crack grows well beyond the plastically deformed region ($c \gg a_c$ in Figure 1.25), the near-tip fields are no longer sensitive to the details of the indentation contact but are instead governed by the symmetric opening of a penny-shaped flaw embedded in an approximately uniform far-field residual tensile stress. Using Sneddon's solution for the strain energy of a penny crack [104] , and applying the Griffith definition $G = dW/dA$, the energy release rate for a crack of radius c scales as

$$G \sim \frac{\sigma^2 c}{E} \tag{1.23}$$

where σ is an effective tensile stress representing the elastic recovery and residual opening forces generated during unloading. This scaling underlies the classical LEM indentation fracture relations. Dimensional considerations, together with the elastic–plastic analyses underlying the classical LEM model [98], show that this effective stress depends on the indentation load P and the contact scale a through

$$\sigma \sim (\frac{E}{H})^{1/2} \frac{P}{c^2} \tag{1.24}$$

so that substitution into the Griffith–Irwin relation $K_I = \sqrt{EG}$ yields a stress-intensity factor of the form

$$K_I \sim (\frac{E}{H})^{1/2} \frac{P}{c^{3/2}} \tag{1.25}$$

Since crack propagation requires $K_I = K_c$, the indentation toughness relation can be expressed in the widely adopted LEM form

$$K_c = \alpha \sqrt{\frac{E}{H}} \frac{P}{c^{3/2}} \tag{1.26}$$

where α is a dimensionless coefficient that depends primarily on the indenter geometry and the crack-shape assumptions. This relation is valid for well-developed median/radial cracks ($c >> a_c$) and forms the basis of most indentation toughness measurements in brittle ceramics.

1.3.2.3 Indentation crack types

During sharp indentation of brittle materials, a variety of crack geometries may develop depending on the indenter shape, the applied load, and the material's deformation characteristics (Figure 1.26).

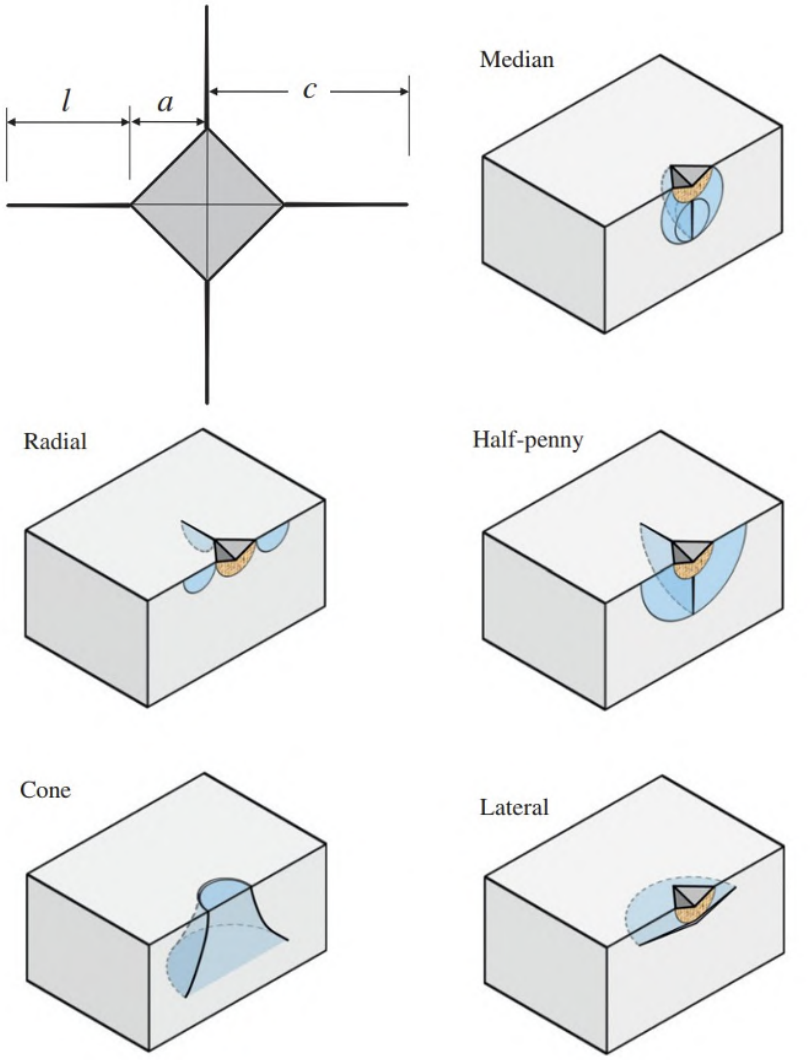

Fig. 1.26. The five major crack types in indentation cracking

Although these cracks are often classified into distinct categories, they are not independent phenomena; rather, they represent different geometric expressions of the same underlying stress field acting at different stages of loading and unloading. Figure 1.26 summarizes the five principal crack types commonly observed in indentation fracture: median, radial, half-penny, Hertzian cone, and lateral cracks.

- **Median Cracks**

Median cracks form beneath sharp indenters during loading. They initiate below the indenter tip in the region of high axial tensile stress and extend downward, approximately symmetric about the indentation axis. Median cracks develop while the indenter is still in contact, driven by the tensile components generated by elastic–plastic mismatch beneath the

indenter. Once stablized, a median crack adopts a vent-like subsurface shape, which in far-field approximation behaves as a penny-shaped crack. This geometry is crucial for deriving the LEM scaling laws used to evaluate fracture toughness.

- **Radial cracks**

Radial cracks emanate from the corners of a Vickers or Berkovich indentation impression during unloading. They initiate at the free surface, where tensile residual stresses peak as the plastically deformed zone attempts to recover elastically. These cracks propagate outward and downward and are commonly used in indentation toughness measurements, where the crack length c is taken along the radial trace. It is worth noting that in some materials, particularly hardmetals, superficially similar surface cracks may appear during loading. These cracks remain shallow and surface-localized, forming the so-called Palmqvist crack geometry, in which only the short surface trace is observed. Although they may resemble the early stages of a radial crack, Palmqvist cracks are mechanically distinct and do not correspond to the long through-thickness radial cracks relevant for toughness evaluation.

- **Half-penny cracks**

A half-penny crack represents the fully developed form of the median crack. As indentation load increases or in materials with limited plasticity, the median crack grows laterally and approaches a semi-circular (half-penny) shape in cross-section. This crack is symmetric in the plane of indentation and corresponds to a classical penny-shape flaw in LEFM. The half-penny geometry provides the justification for the LEM toughness relation (Eq. 1.25), as the stress intensity field surrounding such cracks scales in a predictable manner with load and crack size.

- **Hertzian cone cracks**

Hertzian cone cracks are characteristic of spherical (Hertzian) indentation. They originate at the periphery of the contact circle, where the maximum hoop tensile stress arises during loading. Cone cracks initiate at the free surface and propagate downward along a conical surface. They are typically observed in glasses and other highly brittle solids indented with spherical or blunt indenters. Cone cracking involves minimal plasticity and represents the classical Hertzian fracture mode.

- **Lateral Cracks**

Lateral cracks nucleate beneath the indenter during unloading and propagate approximately parallel to the surface. They are driven by tensile residual stresses concentrated near the elastic–plastic boundary. Lateral cracks are responsible for chipping, spalling, and substantial material removal, dominating the final failure morphology at high loads or in extremely brittle materials. While they do not directly contribute to the LEM toughness formulation, the emergence of lateral cracks marks the limit of the stable median–radial crack configuration. Once lateral cracking occurs, the simple scaling relations underlying indentation toughness measurements no longer apply.

1.3.2.4 Advanced Indentation Cracking Techniques: Micro Pillar Splitting

Although indentation cracking provides a convenient means for probing fracture resistance, its practical application is often limited by uncertainties associated with crack morphology, surface-trace identification, and the need to accurately measure crack lengths. The complex elastic–plastic stress field beneath a sharp indenter further complicates interpretation, as different crack systems (median, radial, Palmqvist, lateral) may be activated depending on load, geometry, and material response. These factors make conventional indentation-based toughness measurements sensitive to crack-shape assumptions and prone to significant scatter.

To overcome these limitations and to enable quantitative toughness measurements at the microscale without relying on post-mortem crack length measurements, an advanced approach, the pillar indentation splitting method, was developed [105]. In this technique, a micro-pillar of radius R is fabricated by focused ion beam (FIB) milling and subsequently loaded with a sharp indenter (Figure 1.27), which generates a well-defined and highly reproducible tensile stress field within the pillar. Instead of forming surface cracks that must be optically measured, the pillar undergoes a sudden axial splitting event at a critical load P_c, recorded as a clear pop-in in the load–displacement curve. This event corresponds to the initiation of a mode-I fracture along a nearly vertical plane.

Although both indentation cracking and pillar splitting involve subsurface tensile stresses, the origins and distributions of these stresses differ fundamentally. In conventional indentation of a bulk specimen, the stress state is strongly influenced by the free surface and by elastic–plastic mismatch beneath the indenter. These factors produce a localized subsurface tensile zone from

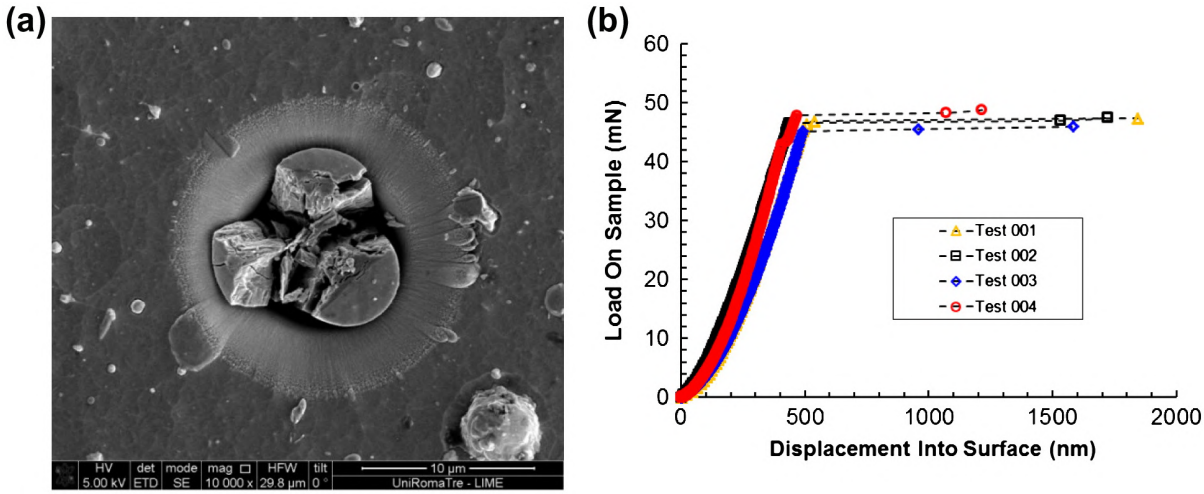

Fig. 1.27. (a) Example of a CrN pillar after splitting. (b) Load-displacement curves for CrN pillars, highlighting the critical load,P_c, corresponding to the crack 'popping out' to the side surface, and pillar splitting [105]

which median cracks originate, and upon unloading, surface-connected radial cracks emerge. In contrast, pillar indentation involves a confined three-dimensional geometry in which the tensile stress field is volume-dominated and peaks along the pillar axis. This geometric constraint drives an internal axial splitting instability rather than the surface-activated crack systems observed in standard indentation tests. Consequently, the characteristic length scale governing fracture is the pillar radius R, rather than a surface-measured crack length.

Because the splitting crack spans the pillar height and the stress field remains geometrically self-similar for any sufficiently sharp indenter, the resulting toughness scaling is universal for Berkovich, cube-corner, and other pyramidal geometries. The proportionality constant γ in the resulting relation is obtained through cohesive-zone finite-element simulations, which account for effects such as pillar aspect ratio, indenter geometry, friction, and crack-path stability. This leads to the calibrated expression

$$K_{Ic} = \gamma \frac{P_c}{R^{3/2}} \tag{1.27}$$

where γ is a geometry-dependent coefficient determined numerically. A key advantage of this method is that neither crack geometry nor crack size needs to be measured, and the stress field driving fracture is far more controlled and interpretable than in conventional indentation cracking.

Finite element modeling (FEM) plays a central role in the quantitative interpretation of the pillar indentation splitting method, as the determination of the calibration coefficient γ in Equation 1.27, which converts the critical load P_c into the fracture toughness K_c, relies entirely on numerical simulation. This coefficient cannot be obtained analytically because the stress field within a confined micropillar arises from complex three-dimensional interactions between the indenter, the pillar geometry, and the underlying substrate. FEM is therefore indispensable for establishing an accurate γ value and enabling quantitative toughness measurement.

Beyond calibration, FEM offers essential physical insight into the mechanics of micro-pillar splitting. It enables direct visualization of the three-dimensional tensile stress distribution generated by a sharp indenter. The information is extremely difficult, if not impossible, to obtain experimentally. Simulations can also track the evolution of the crack front during the splitting process (Figure 1.28b–c), thereby linking the experimentally observed load drop to the underlying fracture mechanics that trigger the instability, which is very important for the interpretation for the phenomenon in Chapter 3.

Because the test involves a sharp pyramidal tip, the contact problem is often simplified by exploiting indenter symmetry. A representative six-fold symmetric slice is commonly used in FEM (Figure 1.28a), reducing computational cost while preserving the essential features of the stress field. The material is typically modeled as linearly elastic prior to fracture, while cohesive zone elements or pre-inserted cracks may be introduced to simulate crack initiation and propagation. Appropriate boundary conditions must constrain the substrate without introducing artificial stiffness. Together, these modeling components allow FEM to accurately reproduce the stress evolution and fracture processes observed in the actual experiment.

Following its introduction as a fracture-toughness test for thin ceramic coatings, the pillar indentation splitting method has undergone substantial development and rapid expansion into a wide range of material systems. Early studies concentrated on validating the method, understanding the sources of scatter, and clarifying the influence of indenter geometry [106–108]. Increasing indenter sharpness enhances the local stress concentration and reduces the critical load at which splitting occurs; nevertheless, the resulting toughness values remain essentially insensitive to the indenter angle when an appropriately calibrated γ factor is used (Figure 1.29). This finding highlights the intrinsic robustness of the method and indicates

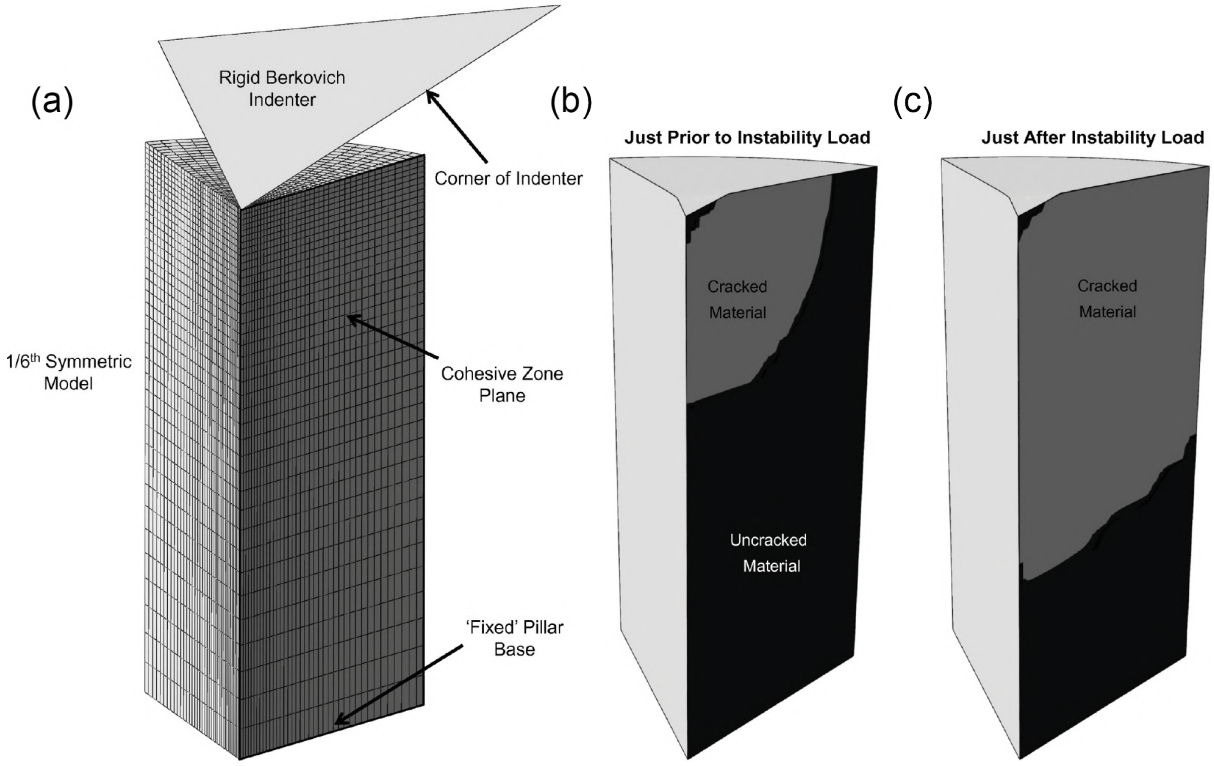

Fig. 1.28. (a) The finite element mesh used in the simulations of pillar indentation fracture; Crack geometries during pillar splitting (b) just before and (c) just after the instability load, the indenter has been removed for clarity [105].

that discrepancies between measurements are governed more by calibration accuracy and load alignment than by the choice of indenter. Complementing this, Lauener and co-workers quantified the influence of positional misalignment, showing that the indenter must be centered within approximately 10% of the pillar diameter to avoid asymmetric loading (Figure 1.30), and evaluated both the contribution of FIB-induced damage and the feasibility of extending the technique to elevated temperatures.

As the pillar splitting method matured, it was rapidly adopted for solid-state electrolytes and cathodes [109], materials for which traditional indentation cracking often fails due to porosity, grain-size gradients and limited crackability. Mechanical stability is critical in these systems, as cycling-induced volume changes and internal stresses may cause cracking and eventual cell failure. Consequently, understanding their intrinsic crack resistance is essential. The pillar splitting test enables direct access to the toughness of the essentially pore-free solid phase, as demonstrated for LLZO-based electrolytes where fully dense samples cannot be produced experimentally [110]. Subsequent studies on LLZO and LATP by Nonemacher et al. [111] and Yan et al. [112] showed that the method can resolve toughness at the level of single

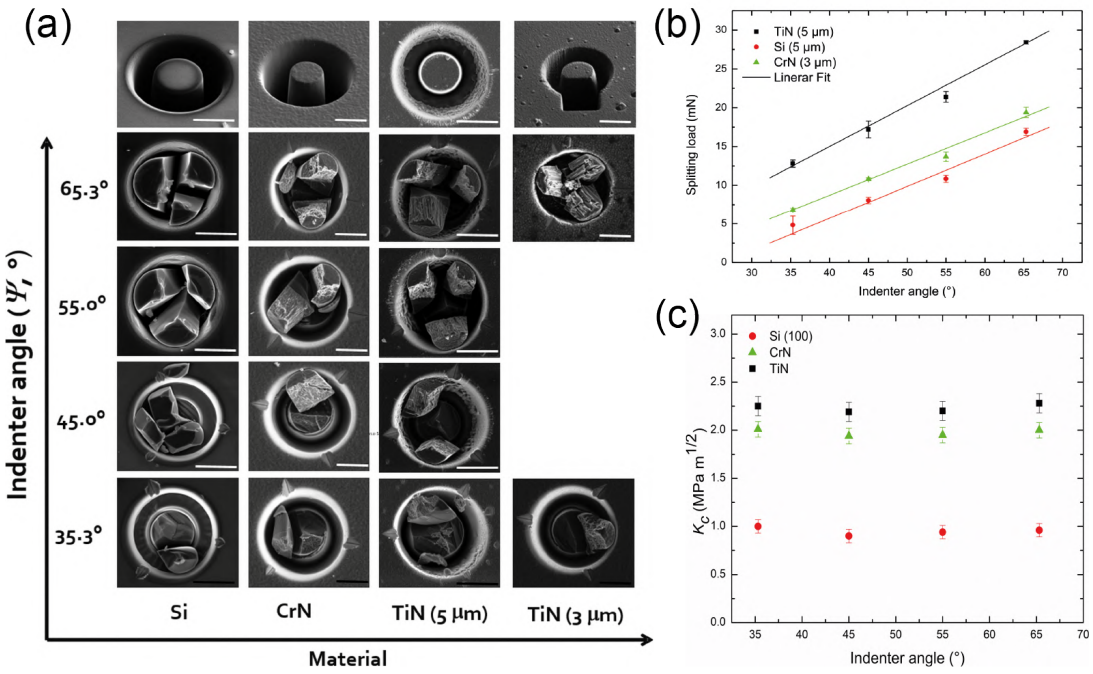

Fig. 1.29. (a) Pillar splitting in three different materials tested using indenters with varying tip angles; (b) average critical splitting load as a function of indenter angle for each material; (c) corresponding apparent fracture toughness plotted against indenter angle [107].

grains and polycrystals, including the influence of crystallographic orientation. These findings highlight the technique's capability for localized, microstructure-specific toughness assessment, which is crucial for evaluating the reliability of solid-state battery materials.

With its capability to probe fracture behavior at the micrometer scale, the method has also been widely adopted for heterogeneous and composite materials, where local variations in composition and microstructure govern failure. Zhou et al. [113] applied micropillar splitting to a dual-phase proton-conducting ceramic, identifying distinct partial- and full-splitting events in the load–displacement curve and linking the intrinsic toughness to crack deflection at phase boundaries. More recently, Li et al. [114] used the technique to dissect the fracture resistance of individual constituents within SiC_f/ BN/SiC composites, demonstrating that phase-specific toughness can be directly measured within a single composite, as shown in Figure 1.31. The growing interest in microscale fracture behavior has also driven the widespread adoption of pillar splitting in multilayer coatings and thin-film systems. White et al. [76, 115] used the method to assess fracture resistance in optical dielectric multilayers, such as AlN/SiO_2, TiO_2/SiO_2, and AlN/Al_2O_3, revealing clear correlations between nanoscale layer design and mechanical robustness. Similar efforts by Xia et al. [116, 117] showed that multilayer and fully coated

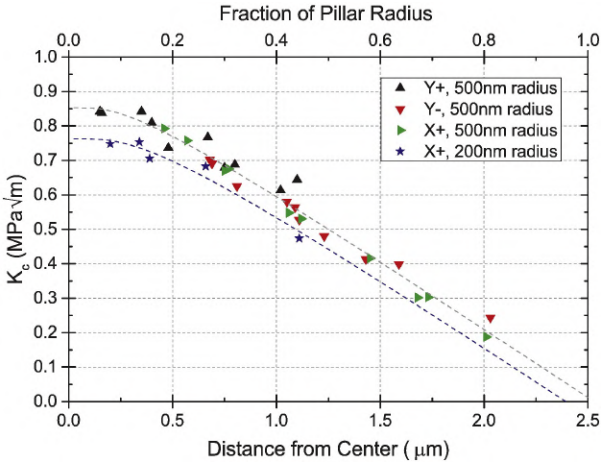

Fig. 1.30. Apparent fracture toughness as a function of the radial offset from the pillar center for a pillar of radius $2.5\,\mu\mathrm{m}$, with the indenter tip radius indicated. [108].

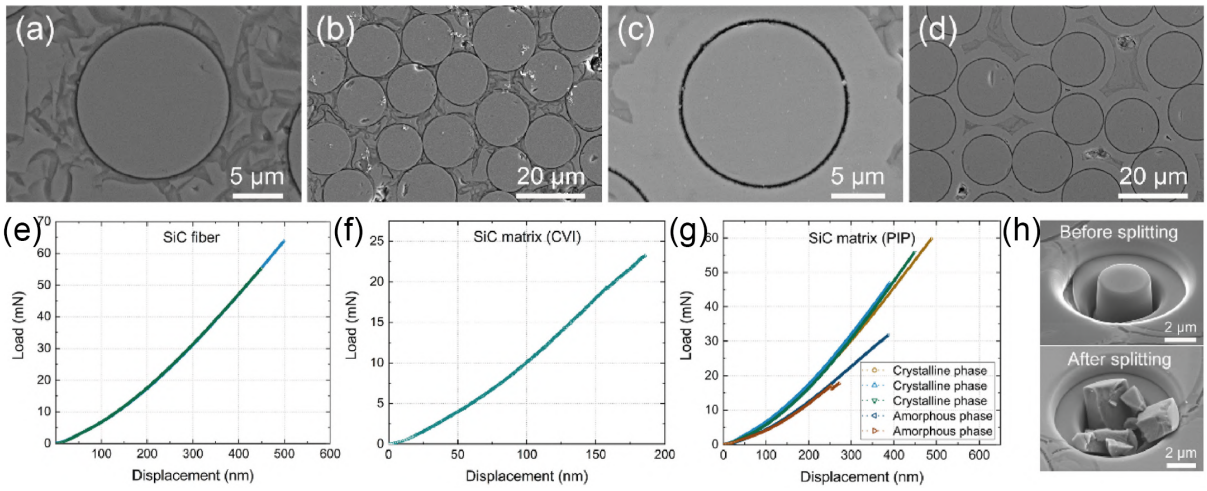

Fig. 1.31. (a–b) SEM images of $\mathrm{SiC}_f/\mathrm{BN}/\mathrm{SiC}_{PIP}$; (c–d) SEM images of $\mathrm{SiC}_f/\mathrm{BN}/\mathrm{SiC}_{CVI+PIP}$; Load-displacement curves and morphology of micropillar splitting: (e) SiC fiber; (f) CVI-SiC matrix; (g) PIP-SiC matrix; (h) SEM images before and after micropillar splitting.

diamond-like carbon films on silicon micro pillar substrate can be reliably characterized even when the coating thickness is only a few micrometers, underscoring the method's suitability for thin, hard coatings. Beyond room temperature, pillar splitting has proven effective under elevated thermal conditions. Best et al. [118] demonstrated controlled splitting of nitride coatings up to 500 °C, while Kanjilal et al. [119] employed in-situ high-temperature testing to map the brittle-to-ductile transition of $CaAl_2$ Laves phase, showing increased apparent toughness prior to the onset of plastic deformation. The method has further been applied to complex materials such as radiation-damaged minerals and thermal-barrier coatings. For instance, Beirau et al. [120] resolved toughness variations of radiation-damaged zoned zircon

with the increased amorphous fraction. Recent studies on YSZ-based TBCs have linked thermal-cycling-induced microstructural evolution to local changes in fracture resistance and optimize the thermal barrier performance[121, 122]. These applications collectively demonstrate the versatility of pillar splitting across coatings, thin films, and thermally or structurally complex ceramics.

1.3.3 Evaluation of residual stress via FIB-DIC

Residual stress is an internal stress field that remains in a material or structure in the absence of externally applied loads. In micro- and nano-scale ceramic systems, residual stress becomes particularly important because the characteristic dimensions are small and the surface-to-volume ratio is high, so even ultra-thin coatings can strongly affect the local mechanical state of the whole component. As discussed in the previous Chapter 1.2, residual stress is not merely a secondary byproduct of processing, but also can be treated as an active parameter governing crack initiation, crack-path selection, and the apparent fracture resistance of the coated system. Therefore, a local, depth-sensitive characterization to provide precise determination of stress level is essential. Among the available approaches, focused ion beam–digital image correlation (FIB-DIC) has emerged as a powerful method for probing residual stress in thin films with sub-micrometer lateral resolution and depth resolution down to tens of nanometers [123].

1.3.3.1 Origins of residual stress in thin films

Residual stress in thin films generally arises from two main contributions: intrinsic (growth-induced) stress and thermal stress [124]. Intrinsic stress develops during film growth as atoms or molecular species adsorb, react, and incorporate into the evolving film, leading to strain accumulation through densification, defect incorporation, grain coalescence, or incomplete structural relaxation. In ALD films, this contribution is often dominant because the layer is built through a self-limiting cycle-by-cycle process, and low deposition temperature, limited atomic mobility, and incomplete network condensation can result in significant tensile stress [57]. In PVD films, intrinsic stress is likewise governed by growth conditions, but additional effects such as energetic particle bombardment, atomic peening, and texture evolution can play a major role [125]. As a result, PVD coatings often exhibit pronounced through-thickness

stress gradients, especially in multilayer systems where local growth conditions change at each interface.

Thermal stress originates during cooling from the deposition temperature because of the mismatch in thermal expansion between the film and the substrate. Depending on the relative contraction of the two materials, the resulting stress in the film may be tensile or compressive. In ultra-thin coatings, the final residual stress is often determined by the combined effect of growth-induced and thermal contributions, and may also depend strongly on film thickness, since thinner films generally retain less relaxed stress states. For brittle micro-ceramics, residual stress is especially important because it directly affects crack initiation and propagation. Depending on the crack geometry and stress state, it may either enhance or reduce the apparent fracture resistance, making accurate local stress characterization essential.

1.3.3.2 Focused ion beam–digital image correlation (FIB-DIC)

Focused ion beam–digital image correlation (FIB-DIC) is a semi-destructive residual stress measurement technique that combines incremental FIB milling, high-resolution SEM imaging, and image-based displacement tracking to quantify local stress relaxation [123, 126, 127]. The method is particularly attractive for micro-scale coated systems because it is applicable to both crystalline and amorphous materials, provides site-specific information, and offers spatial resolution that is difficult to achieve with conventional X-ray-based techniques.

The basic principle of the method is to progressively release the pre-existing residual stress by milling an annular trench around a small central island. As the material is removed step by step, the constrained strain stored in the film is partially relieved, producing a small deformation of the island surface. This deformation is measured by DIC from a sequence of SEM images, yielding the strain-relief profile as a function of milling depth. However, the experimentally measured strain relief is not itself the original residual stress; rather, it is the elastic response of the system to local material removal. Therefore, an inverse analysis is required to reconstruct the underlying stress state from the measured strain evolution.

A convenient framework for this reconstruction is the eigenstrain formulation. In this context, eigenstrain represents the inelastic strain permanently introduced during film growth. It can be regarded as the source of the residual stress field. When part of the stressed material

is removed, elastic compatibility is altered and a fraction of the stored elastic strain is released, but the eigenstrain itself remains the intrinsic quantity associated with the material state [123]. For this reason, the strain-relief profile obtained during incremental milling can be inverted to recover the eigenstrain distribution as a function of depth, from which the residual stress profile is subsequently determined through Hooke's law using the elastic constants of the coating.

To perform this inversion, a calibration relationship is required between the normalized milling depth h/D and the measured strain relief, where h is the milling depth and D is the inner diameter of the annular trench. This relationship is expressed through the strain-relief function and its corresponding master influence function. The need for an influence function arises because the measured surface strain at a given milling step does not depend only on the stress state at that exact depth, but on the cumulative stress redistribution produced by all previously removed material. The influence function therefore describes the sensitivity of the measured strain relief to eigenstrain located at a given normalized depth, allowing the experimental signal to be translated into the underlying eigenstrain profile.

A key aspect of the method is that the average strain is usually not taken over the entire top surface of the ring-core island. The outer perimeter is often affected by FIB artifacts, taper, redeposition, or local damage, which can degrade DIC accuracy. For this reason, strain is evaluated over an inner effective area, commonly defined by a reduction factor relative to the full pillar radius. In the present work, an 80% reduction factor was adopted, following established practice in eigenstrain-based FIB-DIC analysis. For a reduction factor of 0.8, the fitted influence-function parameters are $\alpha = 8.813$, $\beta = 6.647$, and $\gamma = 53.852$. The corresponding strain-relief function can be written as

$$f\left(\frac{h}{D}\right) = 1 - \exp^{-\alpha\left(\frac{h}{D}\right)}\left[1 + \beta\left(\frac{h}{D}\right) - \gamma\left(\frac{h}{D}\right)^2\right], \tag{1.28}$$

and the associated master influence function is obtained by differentiation:

$$F\left(\frac{h}{D}\right) = \exp^{-\alpha\left(\frac{h}{D}\right)}\left[\alpha - \beta + \alpha\beta\left(\frac{h}{D}\right) + 2\gamma\left(\frac{h}{D}\right) - \alpha\gamma\left(\frac{h}{D}\right)^2\right]. \tag{1.29}$$

Based on this formulation, the measured strain-relief profile is first converted into the eigenstrain depth profile, and the residual stress is then calculated from the elastic constitutive

relation. In this thesis, the coating modulus used in this step was independently obtained from nanoindentation after substrate-effect correction. An important feature of the method is that its sensitivity depends strongly on the normalized milling depth. Previous analyses showed that the most reliable sensitivity is achieved only within a limited range of h/D, whereas very shallow cuts may be affected by trench geometry and stress concentration, and deeper cuts progressively lose sensitivity. Consequently, the ring-core diameter must be selected according to the thickness range of interest, which is particularly important for ultra-thin films.

Overall, FIB-DIC is especially well suited to the present thesis because it enables local residual stress profiling in ultra-thin ceramic coatings with high spatial resolution, while also providing a physically grounded route from measured strain relief to eigenstrain and, ultimately, to residual stress. This makes it a powerful tool for correlating deposition conditions, internal stress state, and fracture response in coated micro-ceramic systems.

1.4 | Outline and objectives

Based on the discussion above, the central objective of this thesis is to establish physically grounded strategies for tailoring fracture resistance and deformation behavior in micro-scale ceramic systems through surface and interface engineering. As the characteristic dimensions of ceramic components approach the microscale, their mechanical response becomes increasingly sensitive to surface condition, residual stress, and interfacial architecture. This thesis therefore aims to isolate and systematically investigate these effects, moving beyond bulk material properties and architectural topology alone.

To achieve this objective, the work is structured around three interconnected research tasks. First, a reliable intrinsic mechanical baseline for micro-fabricated silica is established. Using TPPDLW followed by low-temperature pyrolysis, the elastic modulus, hardness, and fracture toughness of silica are quantified and benchmarked against conventionally fabricated counterparts. In particular, silica micropillars with varied radii are fabricated using this novel route, and multiple pyrolysis temperatures are explored to assess the influence of size and thermal processing on mechanical properties. This task provides a validated reference state for

microscale silica, ensuring that subsequent modifications to fracture behavior can be interpreted mechanistically rather than attributed to fabrication artifacts.

Second, the role of surface-induced residual stress in controlling fracture behavior is investigated. Ultra-thin, conformal ceramic coatings deposited by ALD are employed to introduce well-defined stress states at the surface of silica micropillars. The resulting residual stress fields are quantified using FIB–DIC techniques. By systematically varying coating thickness and intrinsic film stress, this study elucidates the interaction between thin-film stress and microscale crack systems, demonstrating how residual stress can be leveraged as an active design parameter for enhancing fracture toughness in brittle micro-ceramics.

Third, the thesis examines interface-dominated deformation and fracture mechanisms in ceramic nanomultilayers fabricated by PVD. Focusing on optically relevant multilayer systems with controlled aperiodicity and crystallinity contrast, this work investigates how multilayer architecture, interface type, and local volume fraction govern crack propagation pathways, strain localization, and mechanical reliability. These studies establish interface engineering as a complementary strategy to stress-based toughening, particularly for functional coatings in which optical and mechanical requirements must be balanced.

Together, these three tasks form a coherent framework for understanding and engineering the mechanical behavior of micro-ceramics through surface and interface design. Rather than treating fracture toughness as a fixed material constant, this thesis demonstrates how it can be actively tuned through controlled modification of near-surface stress states and interfacial architectures, laying the groundwork for the future development of robust, coated ceramic metamaterials.

CHAPTER 2

The mechanical properties of sinterless silica

2.1 | Introduction

Glass is one of the most technologically indispensable inorganic materials, owing to its outstanding optical transparency, excellent thermal and chemical stability, and robust long-term mechanical reliability. These attributes underpin its widespread use in micro-optics, photonics, microelectromechanical systems (MEMS), microfluidics, and emerging nanophotonic devices [128–130]. However, glasses and especially high-purity glasses such as fused silica glass are very difficult to shape, which requires high-temperature melting and casting process from macroscopic objects or hazardous chemicals for microscopic features [131]. Specially, the conventional shaping methods such as etching or laser milling, FIB milling, are constrained to planar or quasi-planar geometries, which is not suitable for some complex shapes in micro devices on chips [128, 132]. These drawbacks largely limited the application of silica in micro devices.

In contrast, three-dimensional (3D) micro-printing technologies offer nearly unconstrained geometric freedom, enabling the realization of complex free-form architectures that are inaccessible to traditional top-down methods. However, direct 3D printing of silica glass has historically relied on particle-loaded resins followed by high-temperature sintering (typically above $1100\,^{\circ}\mathrm{C}$, [133–136]), which restricts compatibility with on-chip integration and severely limits resolution and materials integration.

A transformative advance was recently reported by Bauer et al., who introduced a sinterless, low-temperature two-photon polymerization (TPP) route for fabricating optical-grade fused

silica using a particle-free polyhedral oligomeric silsesquioxane (POSS) precursor [137]. Unlike conventional particle-based routes, this method leverages a continuous silicon–oxygen molecular network that converts into dense amorphous SiO_2 at temperatures as low as $650\,^{\circ}\mathrm{C}$. This breakthrough reduces the processing temperature by nearly $500\,^{\circ}\mathrm{C}$, enables sub-100-nm feature resolution, and allows direct on-chip fabrication of complex 3D silica micro- and nanostructures with excellent optical quality and mechanical resilience. The work of Bauer et al. establishes a fundamentally new materials platform for free-form silica microfabrication, which opens the door for systematic mechanical investigations of architected silica at previously inaccessible length scales.

While the optical performance and compressive strength of sinterless TPP-derived silica have been demonstrated, a comprehensive and quantitative understanding of its local nanomechanical properties, particularly its fracture mechanism remains limited. As the characteristic dimensions of silica-based components continue to shrink into the micro- and nanoscale regime, their mechanical integrity becomes increasingly governed by size effects, surface flaws, and fabrication-induced defects. Under such conditions, precise understanding of the intrinsic mechanical properties of microscale silica is essential for both reliable device design and the development of mechanically resilient micro-architected structures.

In this chapter, we systematically investigate the intrinsic mechanical properties of sinterless TPP-derived silica fabricated through two-photon polymerization followed by pyrolysis. The elastic modulus and hardness are quantified using continuous stiffness nanoindentation, while the fracture toughness is evaluated using the micro-pillar splitting method with both cube-corner and Berkovich indenters. To benchmark the reliability and transferability of this novel fabrication route, the measured mechanical properties are directly compared with those of silica pillars produced by established lithography- and FIB-based fabrication techniques. Beyond method validation, this study further examines the influence of pillar size and heat-treatment temperature on the measured fracture toughness and elastic response. By investigating silica pillars with radii ranging from the sub-micron to several micrometers and by comparing samples pyrolyzed at $1000\,^{\circ}\mathrm{C}$ and $1100\,^{\circ}\mathrm{C}$, this chapter assesses the robustness and size independence of the intrinsic fracture resistance of sinterless silica. These results provide a critical reference state for the later chapters of this thesis.

2.2 | Materials and methods

2.2.1 Micro silica fabrication

2.2.1.1 Sinterless silica micro pillars

The sinterless silica micro pillars were fabricated via TPP-DLW followed by pyrolysis, following the approach reported by Bauer et al. [137]. The POSS-glass resin was prepared by mixing 89 wt% acrylate-functionalized POSS monomer, 9 wt% trifunctional acrylic monomer and 2 wt% photoinitiator of the α-aminoketone family, each component contributing specific functionalities to the hybrid network. The TPP printing of 3D polymer-template micro pillars followed simple standard procedures by using the Nanoscribe PPGT2 system. Therein, the resin was drop cast onto silicon substrate and the 63X objective was directly immersed in the resin. The printing was performed using galvo scanning mode, with a laser average power of $20\,\mathrm{mW}$ and a writing speed of $20\,000\,\mu\mathrm{m\,s^{-1}}$. Uniform circular pillars were designed with a height-to-diameter ratio of 1 and nominal diameters of $4\,\mu\mathrm{m}$, $6\,\mu\mathrm{m}$, $8\,\mu\mathrm{m}$, $10\,\mu\mathrm{m}$, $12\,\mu\mathrm{m}$, which were used for the pillar splitting tests. To meet the requirements for standard CSM testing, the pads were printed as arrays of disks with a diameter of $30\,\mu\mathrm{m}$ and heights ranging from $6\,\mu\mathrm{m}$ to $10.5\,\mu\mathrm{m}$. The printing strategy followed a [0/60/120/90/150/30] laminated manner from unidirectional layers, consisting of multiple voxel-lines with a hatching distance, and a slicing distance between neighboring layers of $0.1\,\mu\mathrm{m}$ and $0.1\,\mu\mathrm{m}$, respectively. Each layer was completed with a contour scan to ensure geometry uniformity. After TPP-DLW, the printed structures were developed by immersion in isopropanol alcohol for $20\,\mathrm{min}$, followed by propylene glycol monomethyl ether acetate (PGMEA) for $5\,\mathrm{min}$ to dissolve the remaining uncured resin. The fabricated specimens were then supercritically dried to prevent damage from capillary forces.

After that, the as-printed polymer templates were subsequently pyrolyzed in air atmosphere using a split tube furnace under $700\,^{\circ}\mathrm{C}$, $1000\,^{\circ}\mathrm{C}$ and $1100\,^{\circ}\mathrm{C}$ for three hours, respectively. The applied heating profiles included a ramp rate of $0.5\,^{\circ}\mathrm{C/min}$, and the cooling rate is $3\,^{\circ}\mathrm{C/min}$. During pyrolysis, all specimens underwent linear isotropic shrinkage of approximately 50%, resulting in fused silica micro pillars with final diameters ranging from $1.98\,\mu\mathrm{m}$ to $5.61\,\mu\mathrm{m}$,

as shown in Figure 2.1. When comparing the Figure 2.1a, f and g, where the samples were same for the as-printed size but sustain different processing temperature. It can be noticed that the samples pyrolyzed at $1000\,^{\circ}\mathrm{C}$ and $700\,^{\circ}\mathrm{C}$ shows similar shrinkage rate, while the even higher temperature $1100\,^{\circ}\mathrm{C}$ leads to higher shrinkage, around 56 %. The pads shrank to a final diameter of around $15\,\mu\mathrm{m}$. Due to their relatively low height-to-diameter ratio, the pads experienced nonuniform shrinkage during sintering, leading to a slightly uneven top surface (Figure 2.2), which is becoming worse with the processing temperature increase.

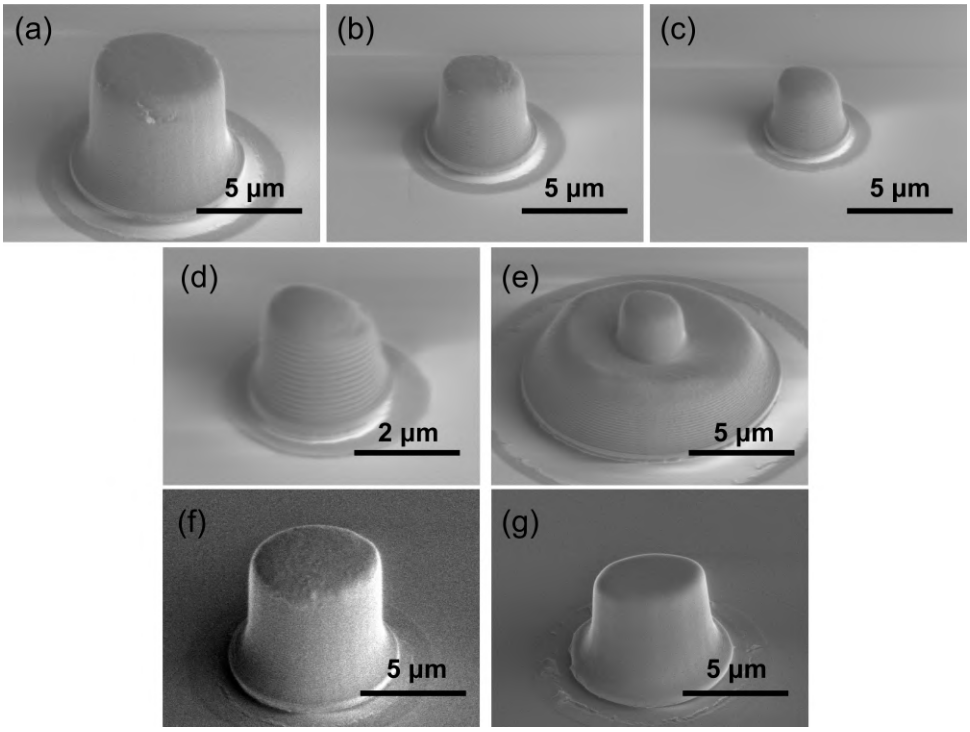

Fig. 2.1. The representative SEM images of micro silica pillar fabricated through TPP and followed pyrolisis at (a-e) $700\,^{\circ}\mathrm{C}$, (f) $1000\,^{\circ}\mathrm{C}$, and (g) $1100\,^{\circ}\mathrm{C}$ with the radii to be (a) $2.91\,\mu\mathrm{m}$, (b) $1.74\,\mu\mathrm{m}$, (c) $1.33\,\mu\mathrm{m}$, (d) $1.27\,\mu\mathrm{m}$, (e) $0.98\,\mu\mathrm{m}$, (f) $2.92\,\mu\mathrm{m}$ and (g) $2.62\,\mu\mathrm{m}$. It is worthy to note that the SEM images in (a-c) and (e-f) were exhibited with the same magnifer.

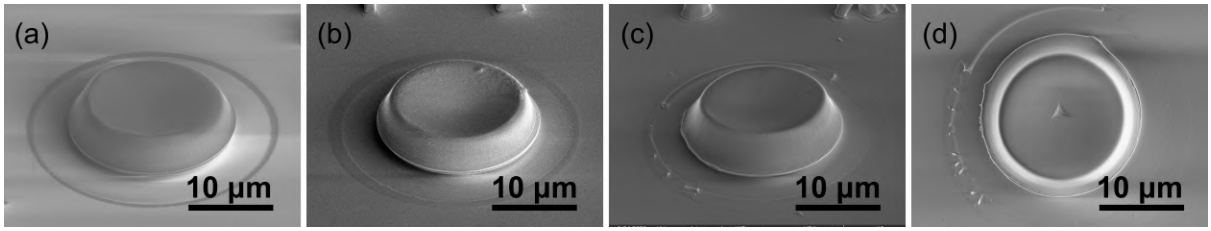

Fig. 2.2. The representative SEM images of silica micro pads fabricated through TPP and followed pyrolysis at (a) $700\,^{\circ}\mathrm{C}$, (b) $1000\,^{\circ}\mathrm{C}$, and (c,d) $1100\,^{\circ}\mathrm{C}$ with the (d) showing the plan view of the pad after nanoindentation test.

2.2.1.2 Reference silica micro pillars

To validate the effectiveness of the novel approach for silica fabrication at reduced sintering temperature, the mechanical properties of the bulk silica from traditional methods were evaluated to be the reference. The preparation of the reference pillars for the splitting tests was performed by a Lithography based technique and an improved FIB procedure.

- **Lithography based deep reactive ion etching**

The fabrication of fused silica micro-pillars followed methods primarily based on the seminal work by Bruns et al. [138], involving lithography-assisted deep reactive ion etching (DRIE). A $500\,\mu\mathrm{m}$ thick, 10 × 10 mm^2 fused silica wafer was processed. Firstly, the $500\,\mathrm{nm}$ and $100\,\mathrm{nm}$ thick aluminum layer was magnetron sputtered onto the front side and the back side of the substrate respectively. The deposition was performed Alliance-Concept DP650 system. The aluminum layer serves as the mask in the front side and increase the electrical conductivity between the sample and substrate during etching process. The etching process contained two main steps. The aluminum mask was firstly covered with a photoresist layer and the direct laser writer (Heidelberg MLA150) was used to patterned the photoresist layer. Subsequently, the hard aluminum mask was patterned by Cl_2/BCl_3 plasma etch (STS Multiplex ICP plasma etcher system). Next, pillar structures were etched into the silica substrate with a high-rate plasma etch using C_4F_8 and O_2 gases in a SPTS APS plasma etcher.

The metallic mask was removed by immersion into a commercial aluminum etchant (ANPE, Microchemicals GmbH), then rinsed in DI water. Subsequent dicing and coating steps protected the pillars, with a diameter of $5.16\,\mu\mathrm{m}$ and a taper angle of 6°. Further details align closely with Bruns et al.'s work.

- **Focused ion beam milling**

The FIB milling procedure was optimized from the ring-core milling approach with the Helios 5CX Dual Beam Microscope, which can minimize the FIB-induced damage on the edge of pillars. The ring milling was carried out in a single outer-to-inner pass with a beam current of $0.48\,\mathrm{nA}$ for coarse milling, followed by a final refinement and shaping process involving a current $48\,\mathrm{pA}$. The resulting pillars had an average radius of $2.51\,\mu\mathrm{m}$ and H/D ratio is nearly 1.

2.2.2 Nanoindentation testing

2.2.2.1 Standard CSM testing

Nanoindentation tests were performed under ambient conditions using a G200 (KLA Corporation) system with Continuous Stiffness Measurement (CSM) mode to evaluate the elastic modulus and hardness of these silica samples fabricated from different techniques. All CSM tests were conducted at a constant strain rate of $0.05\,\mathrm{s}^{-1}$. For the 3D printed silica, the CSM tests were performed on the top surface of the pad with cube corner diamond tip to eliminate edge effects from the surface curvature, as shown in Figure 2.2d. And only one indent was tested in the center position of each pad to avoid the plastic zone overlap between indents. Max depth was set as $400\,\mathrm{nm}$ and the results were evaluated in the depth range from $100\,\mathrm{nm}$ to $350\,\mathrm{nm}$ (less than 10% of the total height) to minimize the effects from the silicon substrate. More than twenty pads were indented to make sure that at least 12 tests were used for the evaluation. For other two types silica samples, the CSM tests were performed on the flat surface of the wafers with a 4×4 array. Max depth was set as $500\,\mathrm{nm}$ and space between indents is $25\,\mu\mathrm{m}$. At least 12 tests were analyzed for final results. Machine compliance and the indenter area function were calibrated on a fused quartz reference sample before and after each test, following the procedure outlined by Oliver and Pharr [78].

2.2.2.2 Pillar splitting testing

The crack propagation resistance of these silica samples were evaluated through pillar-splitting experiments. This technique involved applying an indentation load to the pillars until fracture occurred, eliminating the need for post-test crack length measurements [105, 107, 120]. Firstly, both Berkovich tip and cube corner tip were employed on micro silica pillars with diameter around $5\,\mu\mathrm{m}$ from three techniques to investigate the effect from the tip angle. Then the experiments related with the investigation of size effect and processing temperature were conducted with the cube corner tip to minimize the densification effects associated with a blunt tip. Tip sharpness was regularly monitored, and the area function was recalibrated to confirm stability over the entire test campaign. This minimizes the influence of tip blunting on crack initiation loads, as discussed in previous studies [108, 139].

The apparent fracture toughness (K_c) was calculated using the relationship provided in Equation (1.27). Nanoindentation pillar splitting tests were conducted at a constant strain rate of $0.05\,\mathrm{s}^{-1}$ to assess their apparent fracture toughness. Even though the surface of the 3D printed silica shows the slicing and hatching imprint, the fracture morphology didn't show the crack propagation path dependency along the imprint. The surface roughness is not expected to influence the measured fracture response. To ensure accuracy in tip positioning [108], only experiments with indenter tip precisely centered on the pillar surface, within $0.5\,\mu\mathrm{m}$, were considered. The centering was verified through post-experiment scanning electron microscopy (SEM) imaging of residual marks on the substrate.

2.3 | Results and discussions

2.3.1 Compare with bulk materials

2.3.1.1 E&H comparison

As exhibited in the Figure 2.3, the three silica samples show overlapping mechanical properties with minor to no differences. The elastic modulus lies in the range from 72 to $74\,\mathrm{GPa}$, and the hardness varies from 9 to $10\,\mathrm{GPa}$. Especially, the measured modulus is consistent with the result reported in Jens' work [137] where the pillar compression method was employed. It is worth noting that the measurements for both lithography silica and FIB milled silica was carried out on the polished surface of the wafer, representing the properties of common forms of dense fused silica. In contrast, the tests of 3D printed silica were performed on the top surface of the printed pads with Berkovich tip. The bigger scatter observed in the depth profile of the mechanical properties likely originates from the surface unevenness caused by the shrinkage during pyrolysis. The 3D printed silica shows slightly higher hardness (around 6%) than the other two silica samples, indicating a modest enhancement in local strength. Overall, the results provide strong evidence that the novel 3D printing technique yield silica with fundamental properties comparable to those produced by conventional methods, but requiring a significantly lower sintering temperature.

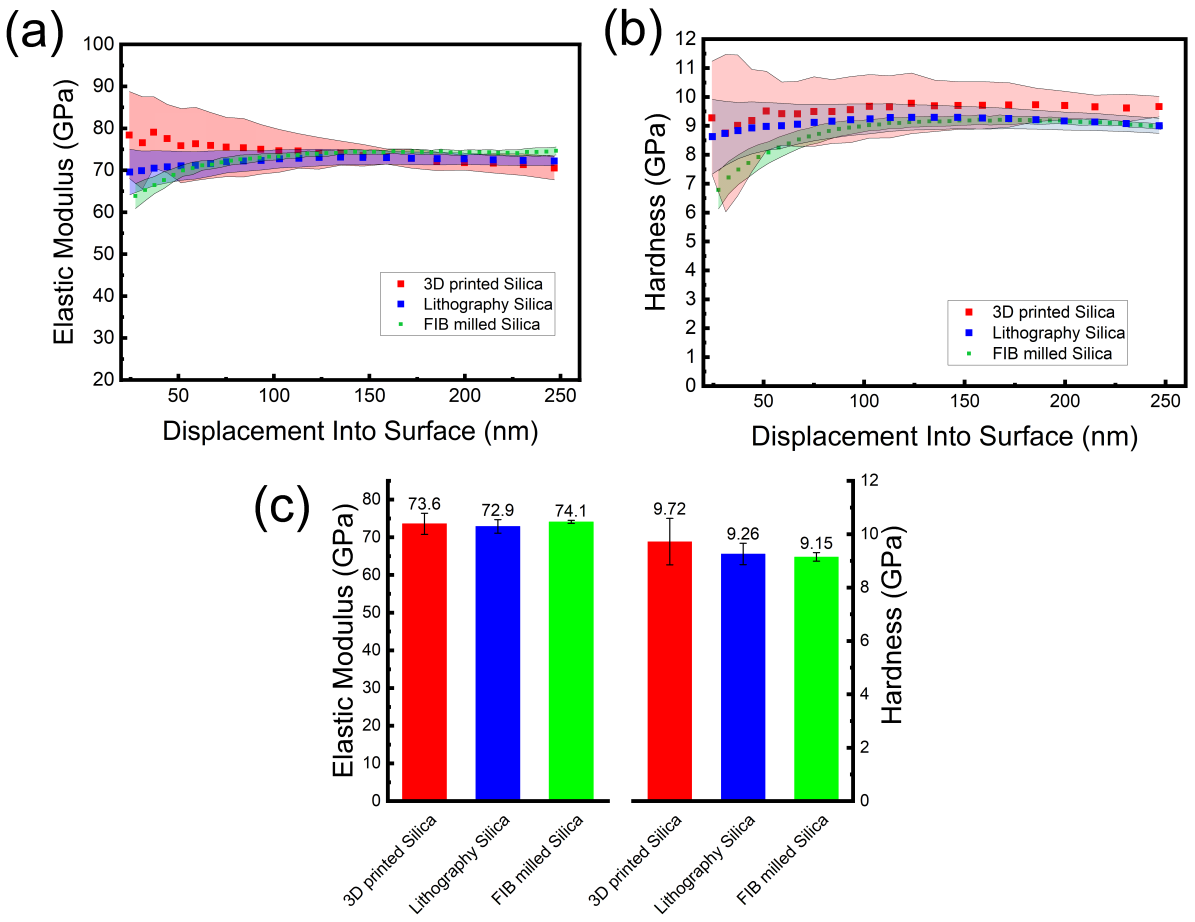

Fig. 2.3. The (a) elastic modulus, and (b) hardness of silica samples fabricated from different techniques as a function of indentation depth. (c) Average elastic modulus and hardness comparison of silica samples fabricated from different techniques

2.3.1.2 Fracture toughness comparison

As introduced in the Chapter 1.3.2, the pillar splitting method is employed to evaluate the crack propagation resistance of the three silica samples. Figure 2.4a and b display the load-displacement curves obtained from splitting tests using Berkovich and cube corner tips, respectively. It should be noted here that the splitting result of FIB milled silica pillars under cube corner tip is not presented since the pillars might be damaged during the FIB process and they were not broken suitably during the splitting. The Berkovich tip, with a centerline-to-face angle of $65.3°$, is significantly blunter than the cube corner tip ($35.5°$). Consequently, the critical crack load for the Berkovich tip ranged from 60 to $120\,\mathrm{mN}$, whereas it was below $7\,\mathrm{mN}$ when using the sharper cube corner tip. An advantage of the pillar splitting method is that the indenter geometry does not affect the accuracy of the fracture toughness evaluation, since the geometry factor of the tip is inherently accounted for in the coefficient γ [107]. Based on the

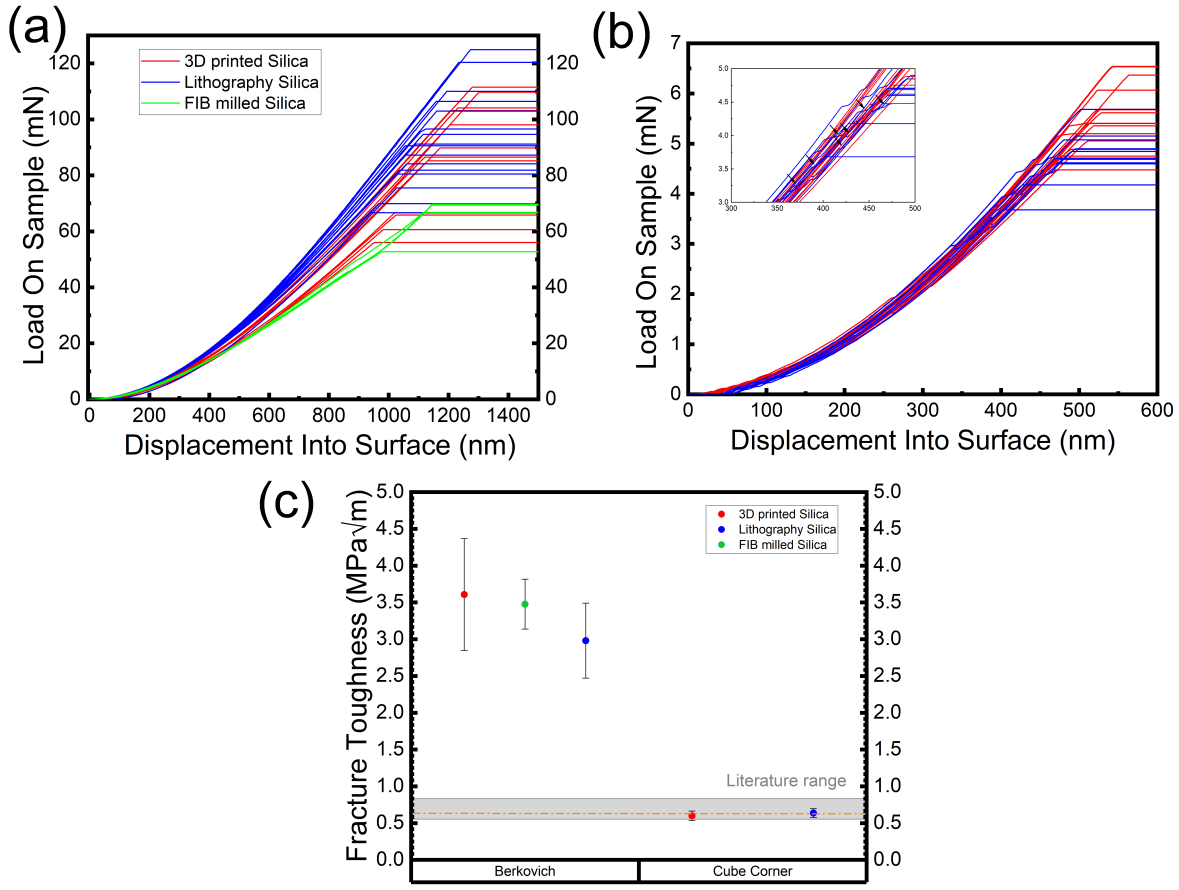

Fig. 2.4. Representative load-displacement curves obtained on the micro silica pillars via (a) Berkovich tip, and (b) cube corner tip. (c) Fracture toughness comparison for the silica samples and the reference range.

relationship reported by Ghidelli et al. [107] between the γ coefficient and the E/H ratio, which is obtained from the CSM results, the following values were used: for the Berkovich tip, $\gamma = 0.18$, 0.19, and 0.20 for the 3D printed, lithography and FIB milled silica samples, respectively; for the cube corner tip, 0.55 was calculated for 3D printed silica, and 0.56 was used for both lithography and FIB milled silica. The final results are presented in the Figure 2.4c. Firstly, for each tip, the three silica samples show comparable fracture toughness. Using the Berkovich tip, the measured values are $3.60 \pm 0.67\,\mathrm{MPa}\sqrt{\mathrm{m}}$, $2.98 \pm 0.51\,\mathrm{MPa}\sqrt{\mathrm{m}}$, $3.47 \pm 0.33\,\mathrm{MPa}\sqrt{\mathrm{m}}$ for the 3D printed, lithography, FIB milled silica, respectively. With the cube corner tip, the corresponding values are $0.59 \pm 0.06\,\mathrm{MPa}\sqrt{\mathrm{m}}$, $0.63 \pm 0.05\,\mathrm{MPa}\sqrt{\mathrm{m}}$, for the 3D printed silica and lithography silica with the cube corner tip. The results indicate again that the 3D printed silica compares favorably with the silica from traditional methods, which reinforces the validity and effectiveness of the novel 3D printing process in fabricating silica with robust properties.

Practically, the fracture toughness value should be independent of the indenter angle. But here the K_c value obtained from the Berkovich tip splitting tests is approximately five times higher than those from the cube corner tip, which is consistent with the reference range reported in [138]. This discrepancy highlights the densification phenomenon in silica [140, 141], which was not considered in the FEM simulation used to determine the γ coefficient. In particular, the blunter Berkovich tip requires a much higher load to induce cracking and cause the pillar failure compared with the sharper cube corner tip. Consequently, the densification becomes more pronounced during the loading which is not captured by the definition of γ . In contrast, the cube corner tip provides a more accurate assessment of the crack propagation resistance of the silica [142].

2.3.2 Size effect

Taking advantage of the 3D printed technique, micro pillars with the diameter smaller than $2\,\mu\mathrm{m}$ can be fabricated to investigate the influence of specimen size on the fracture toughness of silica. The selected range of pillar radii was not limited by of the TPP process itself, but rather by the practical constraints associated with the ex-situ pillar splitting experiments which defined the testing position via optical microscope. As can be seen from the load-displacement curves obtained from splitting tests on pillars of varying radii in Figure 2.5, the loading curves for pillars with radii of $2.91\,\mu\mathrm{m}$ and $1.74\,\mu\mathrm{m}$ demonstrate a consistent trend. However, as the pillar radius decreases, the scatter in the measurement becomes more pronounced, due to the increased sensitivity to tip-center position alignment at smaller scales. Previous researches have investigated the influence of positioning accuracy on the evaluation of fracture toughness [108]. It has been reported that the positioning accuracy of the system should be within ± 10% of the pillar diameter to ensure consistent results. When the indenter is offset farther from the center, the apparent fracture toughness decreases. In this work, the G200 system was employed, which has a position error of approximately $500\,\mathrm{nm}$ due to stage limitations. This inaccuracy can lead to an underestimate of the crack propagation resistance for pillars with radii smaller than $2.5\,\mu\mathrm{m}$ from the 10% rule.

Typically, postmortem images are used to identify and exclude those tests with significant offset, retaining only those with accurate alignment for analysis. However, this approach

is not feasible in the present study since for pillars with radii less than $1.5\,\mu m$, even SEM imaging can not tell if the center position is well aligned. To address this issue, the number of tests was increased to improve statistical reliability, and the data were corrected based on the empirical relationship between the apparent toughness and the offset distance reported in [108]. As shown in the Figure 1.30, the relationship between how the offset fraction regarding the pillar radius would underestimate the apparent fracture toughness was exhibited. For the measured results, we assume a position error around $500\,nm$ from the stage, and implemented the function from Figure 1.30 to correct the measured fracture toughness. The final K_c value for samples of different size, after applying the positioning correction, was displayed in Figure 2.6. The same γ coefficient, 0.55, was applied to measurements for all radii. As illustrated

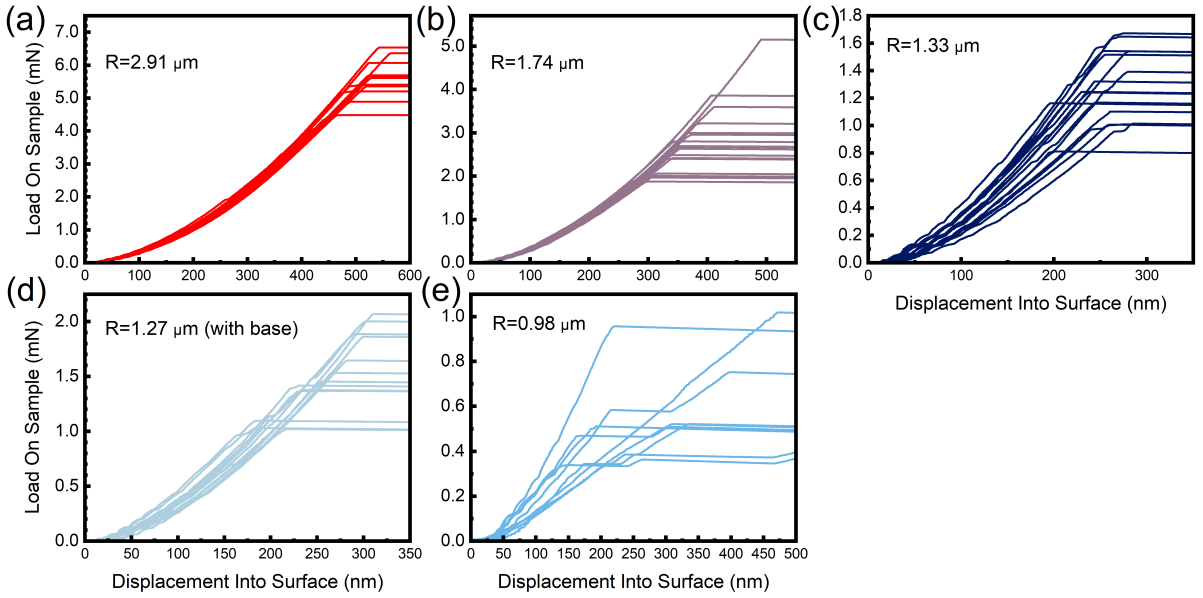

Fig. 2.5. Representative load-displacement curves obtained on the 3D printed micro silica pillars with the radius ranging from (a) $2.91\,\mu m$, (b) $1.74\,\mu m$, (c) $1.33\,\mu m$, (d) $1.27\,\mu m$, (a) $0.98\,\mu m$.

in Figure 2.6, with the pillars radii decrease, the corrected fracture toughness values remain within the range reported in literature. The increased data scatter is mainly attributed to the limitations of the testing system. Even though in-situ pillar splitting within an SEM system can be utilized to reduce the scatter, the electron beam used for live imaging and positioning might affect the silica properties. Therefore, particular care should be taken, for example by turning off the beam during testing. The results obtained from the ex-situ tests clearly

demonstrate that there is no pronounced size effect on the crack propagation resistance of silica. Consequently, the time consuming in-situ tests were not used here.

Unlike strength, which shows a significant improvement when reducing the testing size from macroscopic to microscopic scales, the fracture toughness of silica remains largely size-independent. For example, micro pillars fabricated by the same process show a strength of approximately $4\,\mathrm{GPa}$ [137] and the femtosecond-laser-assisted etching micro silica pillars can reach strength as high as $8\,\mathrm{GPa}$ [143]. Both of them are much higher than the compressive strength of bulk fused silica. The distinction arises from the different mechanical perspectives represented by strength and fracture toughness. Strength refers the maximum stress that a material can sustain before failure. The practical strength of the bulk specimens is usually limited by surface flaws such as micro-cracks introduced during manufacturing, processing and handling [131], When reducing the specimen size, the number and size of potential defects inside the materials decrease. Therefore, the micro scale glass is expected to approach the theoretical strength of glass determined solely by intrinsic atomic interaction. In contrast, fracture toughness reflects the material's resistance to crack propagation, i.e., its ability to create new surfaces and how easy or difficult the propagation is. As describe in the Chapter 1.3.2, when the elastic strain energy stored in the specimen exceeds the surface energy required to form new fracture surface, the crack opens. That is the definition of energy release rate. At the atomic scale, the creation of new surface requires breaking the atomic bonds, which links directly the fracture toughness and the bond energy. Tromans et al. [144] estimated the theoretical fracture toughness of various brittle minerals using a Morse-type bonding model, where the amorphous silica has G_{IC} value $3.72\,\mathrm{J/m^2}$, leading the K_c around $0.52\,\mathrm{MPa}\sqrt{\mathrm{m}}$. Even though the fracture energy of fused silica is not a fixed value, for example, a theoretical estimate of $1.75\,\mathrm{J/m^2}$ for the surface energy of silica glass was obtained by Charles [145], who assumed the surface energy to be equal to the sublimation energy of the materials associated with the surface. And Wiederhorn measured the fracture surface energy of fused silica under different environment, which is around $4.3\,\mathrm{J/m^2}$ [146]. Both Charles and Wiederhorn use the term γ_s which is half of the G_c since crack create double surface. The resulted K_c value ranging from $0.52\,\mathrm{MPa}\sqrt{\mathrm{m}}$ to $0.8\,\mathrm{MPa}\sqrt{\mathrm{m}}$. The prediction aligns well with the range reported in the literature and with the experimental results obtained in this work. Specifically, for

brittle silica, fracture is governed by the intrinsic atomic bonding and surface energy, which are size-independent within this testing regime.

Even though the ductile deformation of silica has been observed under specific nanoscale conditions [147, 148], such behavior occurs only in nanometer scale and low strain rate. For example, $18\,\mathrm{nm}$ diameter SiO_2 glass nanofiber has been shown to exhibit 18% elongation due to enhanced ionic mobility within the free surface affected zone, which promotes bond-switching events under tensile stress [149]. However, within the size range investigated in this work, the silica micropillars exhibit purely brittle fracture behavior. Therefore, the fracture toughness remains independent of specimen size and is governed solely by the intrinsic atomic bonding energy [150].

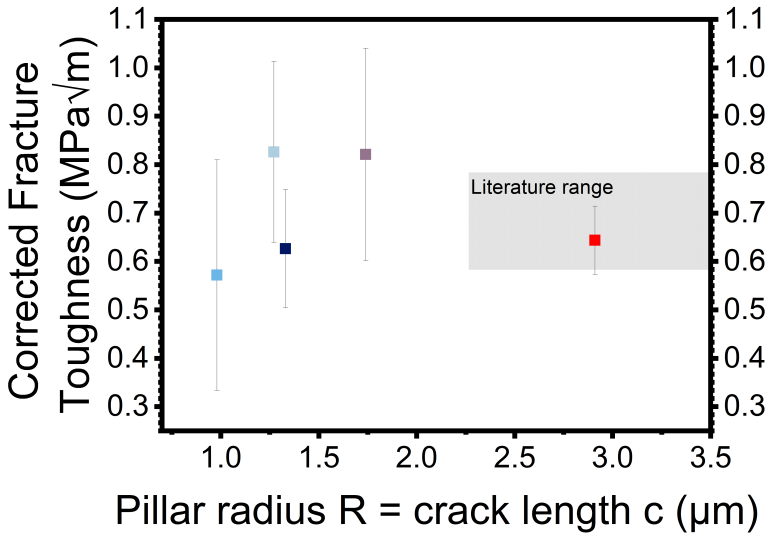

Fig. 2.6. Average fracture toughness comparison for the 3D printed silica with varied radius.

2.3.3 Different processing temperature

The results presented above demonstrate that the silica fabricated at a low processing temperature of $700\,^{\circ}\mathrm{C}$ exhibits identical mechanical properties with those of commercial fused silica. In the work of Bauer et al. [137], it was reported that heat treatment at $1000\,^{\circ}\mathrm{C}$ further enhances the yield strength and compressive strength of the 3D printed silica. Building on that study, the influence of processing temperature on the mechanical properties is further investigated in this section.

2.3.3.1 E&H comparison

As illustrated in Figure 2.7, the 3D printed silica processed at different temperatures show similar elastic modulus and hardness. Indeed, the consistent properties observed along the depth profiles confirm the structural uniformity and homogeneity of the silica samples. The consistency is likely because the processing temperatures remain below the glass transition temperature of fused silica, reported to be $1185\,^{\circ}\mathrm{C}$ to $1200\,^{\circ}\mathrm{C}$ [151]. As clarified in Bauer's previous work [137], the decomposition and mass loss of the as-printed organic-inorganic template mainly occur between $350\,^{\circ}\mathrm{C}$ and $650\,^{\circ}\mathrm{C}$ in air atmosphere. Above $650\,^{\circ}\mathrm{C}$, all organic constituents are completely volatilized, leaving behind only the inorganic material that forms a dense, amorphous silica network without detectable porosity. Consequently, for the samples sintered at $1000\,^{\circ}\mathrm{C}$ and $1100\,^{\circ}\mathrm{C}$, no further compositional changes occur, but only limited microstructural reorganization takes place at elevated temperature [152]. This reorganization is also supported by the micro-Raman spectroscopy reported by Bauer et al. [137], which shows that the characteristic fused silica spectrum is already established at $650\,^{\circ}\mathrm{C}$. Further heating only induces subtle structural rearrangements and, above $800\,^{\circ}\mathrm{C}$, the spectra become indistinguishable from those of commercial fused silica. However, such atomic- or molecular-scale rearrangements are insufficient to overcome the energy barrier for crystallization [153]. As a result, the final material remains amorphous fused silica. Although structural relaxation may occur during heating and influence the mechanical response at elevated temperature, these modifications are thermally reversible and unstable below the glass transition temperature [154, 155]. Therefore, the final samples exhibit consistent mechanical performance, comparable to that of commercial silica glass.

2.3.3.2 Fracture toughness comparison

The pillar splitting tests were employed to evaluate the crack propagation resistance of the sample samples sintered at different temperatures. As shown in Figure 2.8a, the representative load-displacement curves of the samples exhibit the similar mechanical response, consistent with the trends observed for elastic modulus and hardness. The fracture toughness values were calculated using Equation 1.27 and presented in Figure 2.8b.

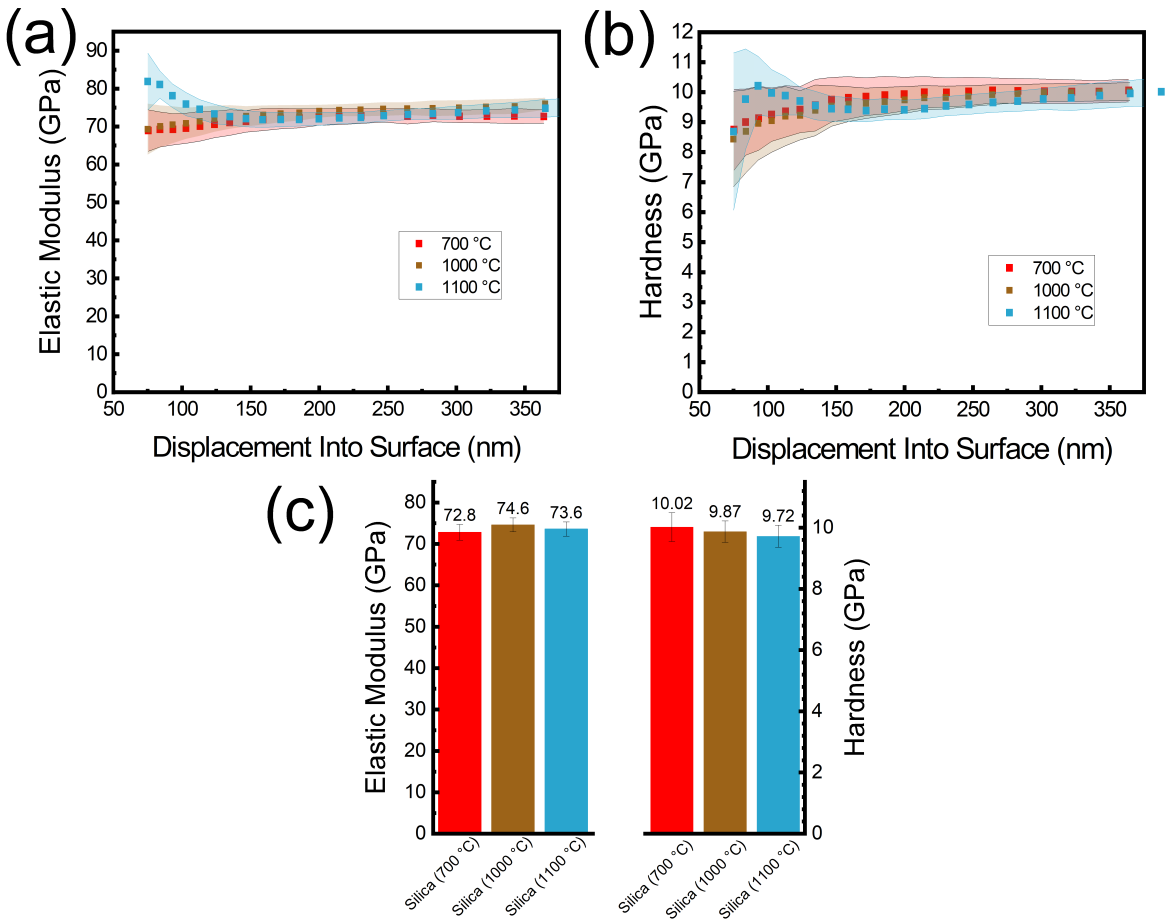

Fig. 2.7. The (a) elastic modulus, (b) hardness as a function of indentation depth, and (c) average value comparison of the 3D printed silica under different processing temperatures.

The 3D printed silica processed at $1000\,^{\circ}\mathrm{C}$ and $1100\,^{\circ}\mathrm{C}$ shows toughness values of $0.68\,\mathrm{MPa}\sqrt{\mathrm{m}}$ and $0.67\,\mathrm{MPa}\sqrt{\mathrm{m}}$, respectively, which is slightly higher than that of silica sintered at $700\,^{\circ}\mathrm{C}$ ($0.60\,\mathrm{MPa}\sqrt{\mathrm{m}}$). Nevertheless, all values fall within the typical range reported for fused silica in the reference. As discussed in the Chapter 2.3.2, the crack propagation resistance of the brittle amorphous silica is governed primarily by its microstructure and the atomic bonding energy. The consistent elastic modulus and the hardness results confirm that the heating process below the glass transition temperature does not alter the short-range atomic structure of fused silica, leading to comparable fracture toughness across all samples.

It is worth noting that the scatter between the individual test becomes more pronounced as the processing temperature increases to $1100\,^{\circ}\mathrm{C}$. The may be attributed to localized structural relaxation process occurring near the glass transition temperature. Although the global glass network remains amorphous and the overall ring statistics are largely preserved,

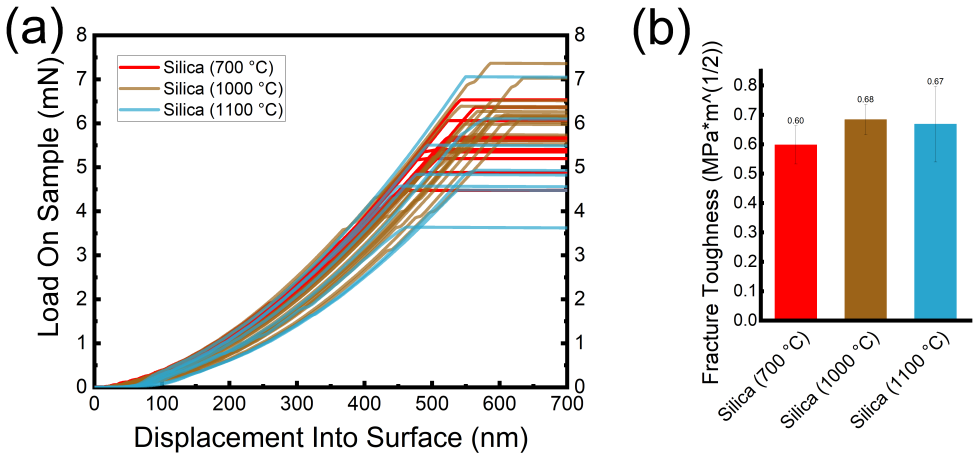

Fig. 2.8. (a) Representative load-displacement curves, (b) average fracture toughness comparison of the 3D printed micro silica under different processing temperatures.

the higher thermal energy facilitates a limited number of irreversible atomic rearrangements or bond reconfigurations [156]. These subtle, localized variations do not significantly affect the bulk mechanical response but can influence crack initiation and propagation, making the fracture behavior slightly more sensitive to local bonding heterogeneity.

2.4 | Conclusion

In this chapter, the intrinsic nanomechanical properties of sinterless silica fabricated via two-photon polymerization and subsequent pyrolysis were systematically investigated and benchmarked against commercial silica wafer where the micro pillars were produced by lithography and focused ion beam milling. Using CSM nanoindentation and the micro-pillar splitting method, the elastic modulus, hardness, and fracture toughness of microscale silica were quantitatively established across multiple fabrication routes.

The fracture toughness of the 3D printed sinterless silica, measured using a cube-corner indenter, was determined to be $0.598 \pm 0.066\,\mathrm{MPa}\sqrt{\mathrm{m}}$, which lies within the established literature range for fused silica and is fully comparable to that of lithography-fabricated silica pillars ($0.637 \pm 0.059\,\mathrm{MPa}\sqrt{\mathrm{m}}$). This close agreement unambiguously validates the mechanical equivalence of the sinterless TPP-derived silica to conventionally processed silica, despite the drastically reduced processing temperature. Furthermore, the consistent densification-driven increase in apparent fracture toughness to values approaching $3\,\mathrm{MPa}\sqrt{\mathrm{m}}$ under Berkovich

indentation demonstrates that the deformation and crack evolution mechanisms of the printed silica remain fundamentally identical to those of traditional fused silica.

By extending the pillar splitting measurements to silica pillars with radii ranging from $2.91\,\mu\mathrm{m}$ down to $0.98\,\mu\mathrm{m}$, and by applying the appropriate corrections to mitigate the error from the position precision of ex-situ for the small pillars, this study further demonstrates that the intrinsic fracture toughness of sinterless silica is essentially size-independent over the investigated micrometer-scale regime. In addition, silica samples pyrolyzed at $1000\,^{\circ}\mathrm{C}$ and $1100\,^{\circ}\mathrm{C}$ exhibit nearly identical elastic modulus, hardness, and fracture toughness, confirming the robustness of the glass network formation process and the thermal stability of the resulting mechanical properties.

Collectively, these results establish that sinterless TPP-derived silica possesses intrinsic mechanical properties, elastic modulus, hardness, and fracture resistance, that are indistinguishable from those of conventionally fabricated fused silica, while offering unprecedented geometric freedom and significantly reduced processing temperatures. This combination is particularly significant for microsystems, micro-optics, and nanophotonics, where mechanical reliability must be ensured alongside structural complexity and integration compatibility.

CHAPTER 3

The fracture toughness enhancement of silica via ALD stress engineering

3.1 | Introduction

Micro- and nano-architected metamaterials represent a transformative approach in the design of lightweight, ultra-stiff, and ultra-strong materials. At reduced scales, size effects and enhanced structural control enable unique mechanical and functional behaviors, providing unprecedented opportunities for material optimization in a wide range of applications [157]. For example, glassy carbon (GC) with micro-architected structures fabricated using two-photon lithography followed by pyrolysis achieve strengths up to $3\,\mathrm{GPa}$ [17] and approach theoretical limits of strength and stiffness [18]. Structures such as bending-dominated lattices, honeycomb configurations, bow-tie designs, and hierarchical woven architectures offer precise control over stiffness, strength, energy absorption, and unconventional properties such as negative Poisson's ratios [6, 21, 22, 158].

The application of ceramic or metallic films using techniques such as conformal atomic layer deposition (ALD), electroless plating, and magnetron sputtering significantly enhances the mechanical and functional performance of these metamaterials. For example, the integration of metallic thin films, such as Ni alloys or high-entropy alloys via magnetron sputtering, has demonstrated substantial improvements in load-bearing capacity and resilience [43, 54, 55]. Compared with other coating techniques, ALD stands out for its exceptional ability to produce films with unparalleled uniformity and atomic-scale thickness control, facilitating precise engineering of material interfaces [159]. For instance, Al_2O_3 films deposited via ALD have been shown to strengthen polymer-based [28] and glassy carbon-based [17] nano- and

micro-lattice scaffolds, even with thicknesses of 10–50 nm. Surface roughness, flaws, and processing-related imperfections often render GC metamaterials sensitive to environmental conditions such as humidity and temperature fluctuations [160]. The use of coating films as barriers against environmental degradation can substantially improve reliability. However, one universal byproduct of these deposition techniques, particularly ALD and sputtering, is the generation of residual stresses within the film–substrate system. These stresses, often inherent to growth mechanisms and thermal mismatch, can profoundly influence fracture behavior.

Residual stress in thin films has been widely investigated. It is well established that compressive residual stress can enhance the apparent toughness of films by suppressing crack opening and delaying crack propagation, while tensile residual stress often accelerates crack growth and reduces mechanical reliability [161, 162]. Most of these investigations focus on the fracture behavior of the film itself, often considering relatively thick coatings or planar geometries. Much less attention has been given to how ultrathin films, on the order of tens of nanometers, modify the fracture resistance of the underlying substrate, especially in microscale architectures where surface effects are amplified.

The mechanical response of architected materials built from brittle constituents often depends on the behavior of their load-bearing elements. In realistic microarchitectures, failure is not a purely global event, but typically initiates locally at regions of elevated stress or geometric imperfections. Recent work by Shaikeea et al. [36] has shown that in ideal elastic-brittle lattices such as the octet-truss, failure strength rather than fracture toughness controls the onset of collapse, due to the absence of damage zones and the discrete nature of load transfer across struts. Their results, which are held in systems where the characteristic strut size is small relative to the critical flaw size, highlight the limitations of continuum fracture mechanics in describing the structural response at the lattice scale. However, in practical implementations of brittle micro-lattices, individual struts often exhibit manufacturing-induced flaws, surface damage, or non-negligible residual stress fields. Under such conditions, local failure may no longer be governed solely by the intrinsic strength of the material but instead becomes sensitive to crack initiation and propagation criteria. Experimental studies have shown that introducing flaws in brittle lattice components can shift the failure mechanism toward a toughness-limited regime, even in nominally strength-dominated architectures [41].

Furthermore, thin-film coatings have been demonstrated to modulate crack resistance in brittle micro-architectures by altering surface stress and fracture behavior [163].

In this work, we investigate how residual stress introduced by conformal ALD coatings affects the apparent fracture toughness of micro-ceramic elements. By isolating individual coated pillars and subjecting them to controlled fracture experiments (Figure 3.1), we quantify the influence of interface properties and internal stress fields on crack resistance in fused silica and glassy carbon. These materials, being archetypal brittle systems with process zones much smaller than the feature size, provide a suitable platform for assessing coating-induced modifications in local fracture behavior. The focus is placed on the mechanics of damage initiation in coated struts, which remains relevant to the overall failure evolution in architected materials, even when strength-based metrics ultimately describe the global failure. To achieve this, Plasma-enhanced (PE) and Thermal (TH) Atomic Layer Deposition (ALD) was employed to fabricate Al_2O_3 and ZnO thin films on two types of ceramic substrates—fused quartz and glassy carbon micropillars. The details can be seen in Table 3.1. Special attention was given to the effects of the residual stress state in the deposited thin films on the crack propagation mechanisms. Two main advanced analysis techniques were employed: (i) high-resolution focused ion beam–digital image correlation (FIB-DIC) [123, 126, 127, 164], enabling precise residual stress measurements at localized regions, providing a powerful tool for analyzing the stress level in ultra-thin films (Figure 3.1b); (ii) pillar splitting [105], which is exhibited in Figure 3.1c, to evaluate the apparent fracture toughness of the coated systems in an efficient, geometrically convenient and statistically reliable way. The experimental campaign is crucially accompanied by Cohesive Zone Finite Element Method (FEM) simulations offering detailed insights into stress distributions and deformation mechanisms, thereby providing a more comprehensive understanding of the fracture behavior in these systems. By integrating experimental and computational approaches, this work seeks to provide new insights into the role of surface modifications and residual stress in enhancing the mechanical reliability of micro-architected metamaterials, offering guidance for the design of next-generation materials with tailored properties by fine-tuning the interface stress level.

Table 3.1
Overview of micro-pillars fabricated via two different lithographic techniques and ALD coating method. The table details the substrate material, deposited oxide, ALD thickness, and process parameters, including deposition type and temperature.

Microfabrication Method	Micro-Pillar Material	Coating Material	Coating Thickness* (nm)	ALD Process Type	Process Temperature (°C)
Two-Photon Lithography and Pyrolysis	Glassy Carbon	Al_2O_3	50 (50.9)	Plasma-enhanced	200
		Al_2O_3	50 (50.9)	Thermal	200
		Al_2O_3	50 (44.4)	Thermal	350
Deep Reactive Ion Etching Lithography	Fused Quartz	Al_2O_3	50 (45.7)	Plasma-enhanced	250
		Al_2O_3	50 (50.5)	Thermal	200
		Al_2O_3	50 (53.7)	Thermal	300
		Al_2O_3	100 (96.4)	Thermal	300
		ZnO	50 (55)	Thermal	100

* The values inside the parentheses represent the actual coating thickness, which was used for experimental data analysis. For simplicity, the nominal values of 50 and 100 were used in the main text description.

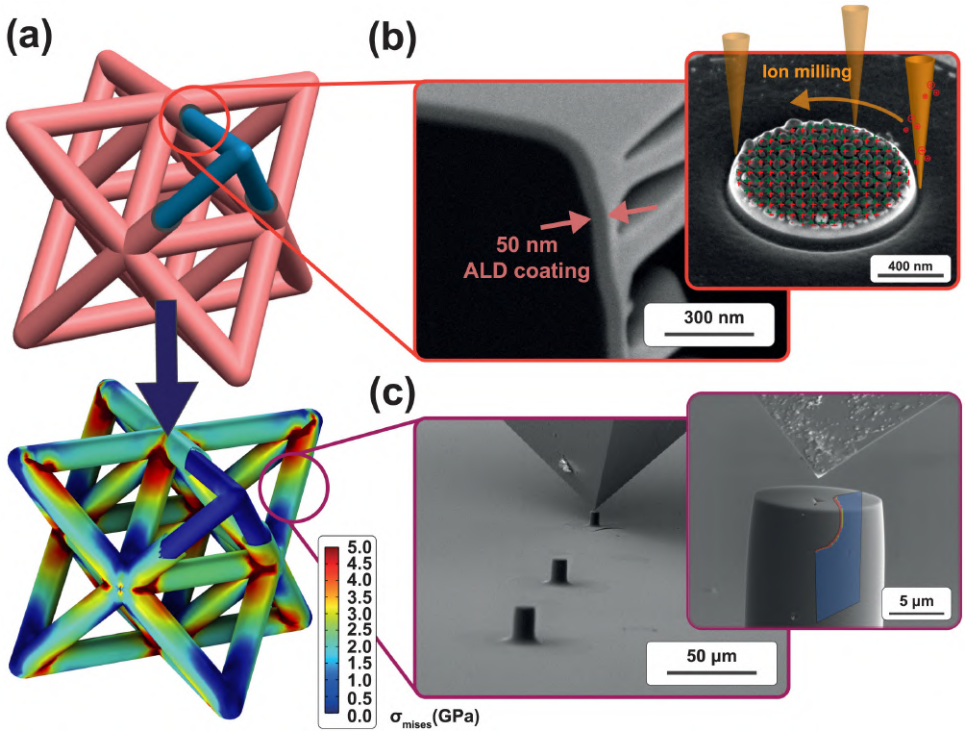

Fig. 3.1. (a) Exemplificative illustration of an octet-truss unit cell coated with a thin film (top, film in reddish color) and the anisotropic compressive stress distribution (superimposed on the residual stresses from the film) from finite element simulation (bottom); (b) Al_2O_3 ALD coating on glassy carbon and Focused ion beam-digital image correlation method (FIB-DIC) for accurate residual stress measurement; (c) Pillar splitting method with a sharp indenter to evaluate the apparent fracture toughness of coated micro-pillar with the insert cross-section exhibiting crack geometry simulated through cohesive zone finite element model.

3.2 | Materials and methods

3.2.1 Description of the finite element model

The primary objective of the finite element simulations is to analyze crack propagation behavior during pillar indentation and to examine how residual stress in the film affects the crack resistance of a ceramic substrate across various crack configurations. Based on this ambition, the commercial package ABAQUS/Standard is used for the cohesive zone finite element simulations [165]. As shown in Figure 3.2a, a three-dimensional, six-fold symmetric finite element model with the rigid Berkovich pyramidal indenter tip, characterized by a centerline-to-face angle of $65.3°$, was generated because of the symmetric boundary conditions. Crack planes with cohesive elements were positioned perpendicular to the free surface and aligned with the edges of the indenter (Figure 3.2a) due to the fact that the cracks are generated along the indenter edges only irrespective of three-sided indenter if the symmetric conditions are maintained [166].

Due to the limitation of the cohesive element model that the crack length was at least 10 times greater than the cohesive zone, a micro-pillar with a $150\,\mu m$ radius and a $300\,\mu m$ height was used to simulate the uncoated substrate. To replicate experimental conditions, thin films with thicknesses of $3\,\mu m$ and $6\,\mu m$ were added to the top and side surfaces of the substrate, corresponding to the real tests with $50\,nm$ and $100\,nm$ films, respectively (R:t = 300:1 and 300:2). Over 30,000 fully integrated elements (C3D6 and C3D8) were employed, with the mesh refined near the contact interface and coating regions to ensure accurate results. The constitutive behavior of the elements was characterized by three key material properties: elastic modulus (E), Poisson's ratio (ν), and yield strength (Y), as summarized in Table 3.2. The parameter settings follow the previous work of Johanns and Bruns [140, 166], which established conditions to induce distinctly different crack geometries during indentation. The substate, when $E/Y = 9.3$, is expected to create median crack, what $E/Y = 102.77$ will induce Palmqvist crack [166]. The behavior of fused quartz which develops median cracks was modeled using the Drucker-Prager Cap plasticity model to account for densification effects,

which are typically present for such materials [140]. This modeling approach enables a detailed investigation of how residual stress influences crack propagation under different fracture modes.

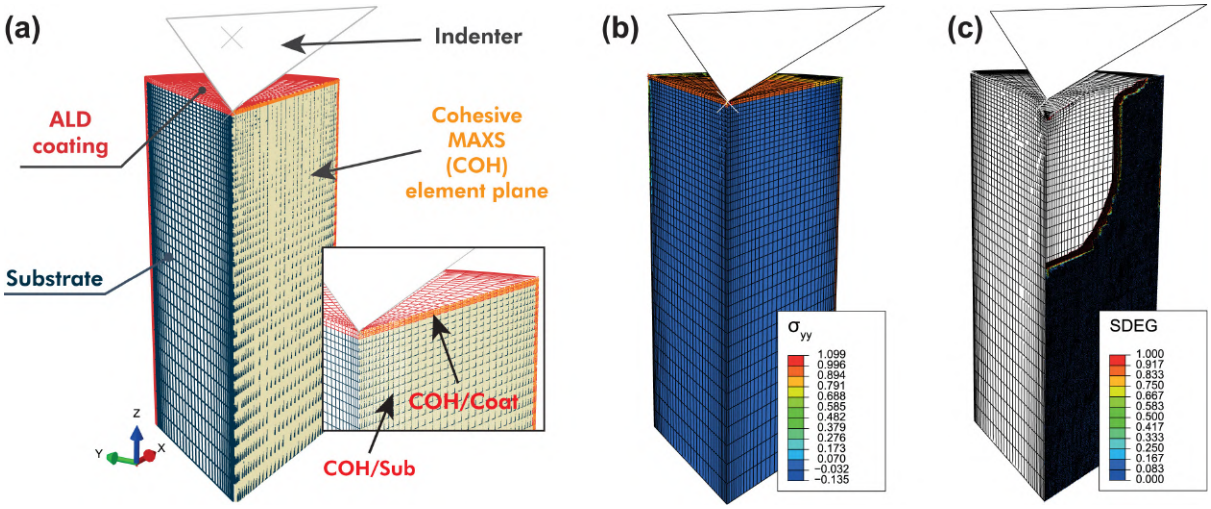

Fig. 3.2. Finite element model utilized for this work: (a) model characteristics; (b) thermalization step for residual stress equilibrium; (c) indentation and cracking process.

Firstly, residual stress was introduced via a predefined temperature and thermal step, allowing control over the temperature difference to replicate experimental conditions (Figure 3.2b). Different thermal expansion coefficients were assigned to substrate and film materials to create thermal strain. The simulated stress value (σ_{th}) was determined using the relationship [124]:

$$\sigma_{\text{th}} = f(E_f, E_s, \nu_s, \nu_f; (T_D - T_M), (\alpha_f - \alpha_s); R/t) \tag{3.1}$$

where E_f is the elastic modulus of the film, ν_f is the Poisson's ratio of the film, α_f and α_s are the thermal expansion coefficients of the film and substrate, T_{D} and T_{M} are the deposition and room temperature, which are achieved as predefined temperature and final temperature in thermal step respectively. It is important to note that the residual stress in the actual experiment results not only from the thermal mismatch during cooling but is primarily due to intrinsic stress generated during the film growth, which is more complex. Here, a simplified thermal step was employed to approximate the final residual stress value.

Crack extension in the current simulations was modeled with Abaqus bi-linear traction-separation-based cohesive elements(COH3D8) with zero initial thickness. The debonding initiation was governed by a MAXS criterion, and crack nucleation was defined using a fracture

energy parameter. Under the condition of linear elastic fracture mechanism (LEFM), the fracture energy (G_{Ic}) can be related to fracture toughness through:

$$K_{Ic} = \sqrt{\frac{EG_{Ic}}{1-\nu^2}} \tag{3.2}$$

The value can be checked in Table 3.2. Please note that the G_{Ic} in Equation 3.2 would be two times of the fracture energy shown in the table since only one COH plane was simulated in the six-fold model. Material properties, loading conditions, and pillar geometry dictated crack growth. Still, it was constrained to remain within the defined crack plane, noting that crack growth in the experiments may have more complex geometries. More details about the cohesive zone model can be checked in previous work [105, 166]. The contact between the Berkovich tip and the material surface was modeled as frictionless. The indentation step was performed under displacement control. Crack propagation along the cohesive plane is visualized using the parameter SDEG [165], which represents the stiffness degradation of a cohesive element on a scale from 0 to 1, with 1 indicating complete failure (Figure 3.2c). The first load drop represented the material fracture. The value is defined as P_c, the critical instability load. The material-dependent relationship can be described by Equation 1.27. The dimensionless constant γ has been determined for various material and tip combinations through cohesive zone finite element modeling [105, 107, 120]. When testing the same material under different conditions, the ratio of critical loads (P_c) directly reflects variations in crack propagation resistance, independent of the calibration constant γ. Given this relationship, the critical load, P_c, will be used as a representative parameter for the apparent fracture toughness of the film-substrate micro-pillar system.

Table 3.2
Constitutive parameters in finite element simulations

Materials	Elastic modulus (GPa)	FE Poisson's ratio	FE Yield strength (GPa)	Fracture energy (GPa μm)	Fracture toughness (MPa$\sqrt{\text{m}}$)
Substrate (median crack)	70	0.18	7.5	0.0125	1.34
Substrate (Palmqvist crack)	185	0.22	1.8	0.01	1.927
Film	180	0.25	5.4	0.00368, 0.02503	1.19, 3.1

3.2.2 Micro-pillars fabrication

The fabrication of fused silica micro-pillars followed methods primarily based on the seminal work by Bruns et al. [138], involving lithography-assisted deep reactive ion etching (DRIE). A $500\,\mu m$ thick, 10 mm diameter fused silica wafer was processed, utilizing a hard aluminum mask due to the low etch selectivity of silica against photoresists. The aluminum mask was patterned using a direct laser writer and an optimized Cl_2/BCl_3 plasma etch. Pillar structures were etched into the silica substrate with a high-rate plasma etch using C_4F_8 and O_2 gases. Subsequent dicing and coating steps protected the pillars, with a diameter of $5.16\,\mu m$ and a taper angle of 6°. Further details align closely with Bruns et al.'s work.

Pyrolytic carbon micro-pillars were fabricated via two-photon polymerization direct laser writing (TPP-DLW) followed by pyrolysis, as previously described [160]. The TPP-DLW process employed a Photonic Professional GT system (Nanoscribe GmbH) with a 63×1.4 oil objective (Carl Zeiss AG) and a FemtoFiber pro NIR laser (TOPTICA Photonics AG). Polymeric templates were printed from IP-Dip photoresist (Nanoscribe GmbH) on silicon substrates in a layer-by-layer manner, using a galvanometric scanning mode, $19\,mV$ laser power, and $20\,000\,\mu m\,s^{-1}$ speed. Circular pillars with height-to-diameter ratios of 2 and nominal diameters of $20\,\mu m$ and $40\,\mu m$ were constructed with $0.1\,\mu m$ hatching and $0.2\,\mu m$ slicing distances. Post-printing, templates were cleaned in propylene glycol monomethyl ether acetate (PGMEA) and isopropanol before critical point drying (Autosamdri-931, Tousimis). Pyrolysis was conducted at $900\,°C$ for $1\,h$ in a vacuum furnace with a ramp rate of $3\,°C\,min^{-1}$, causing 70% isotropic shrinkage. Final pillar diameters, measured via SEM (FEI Helios NanoLab™ 600), were $5.3\,\mu m$ and $11.8\,\mu m$.

3.2.3 ALD coatings

Atomic layer deposition (ALD) was employed to produce conformal ceramic thin coatings on micro-pillars under different process conditions (Table 3.1 (b)) using Beneq TFS200 equipment. Al_2O_3 thin films were deposited using TriMethylAluminium (TMA) as the precursor with O_2 as the oxidant, while ZnO films were deposited using Diethylzinc (DEZ) with H_2O as the oxidant. Fused quartz micro-pillars were coated with Al_2O_3 using plasma-enhanced ALD at

$250\,^{\circ}\mathrm{C}$ with a biasing configuration (up to $300\,\mathrm{W}$ at $13.56\,\mathrm{MHz}$) applied in the plasma module between the source and a grid. No bias was applied to the substrate to prevent coating damage from accelerated species. Additionally, thermal ALD was performed at $200\,^{\circ}\mathrm{C}$ and $300\,^{\circ}\mathrm{C}$ for Al_2O_3 deposition. ZnO films were deposited on fused quartz micro-pillars using thermal ALD at $100\,^{\circ}\mathrm{C}$. To ensure consistency in mechanical property measurements of the thin films, flat silicon wafers ($1.2\,\mathrm{cm} \times 4\,\mathrm{cm} \times 0.04\,\mathrm{cm}$) were coated under the same conditions as the fused quartz micro-pillars. For glassy carbon micro-pillars, Al_2O_3 coatings were deposited using plasma-enhanced ALD at $200\,^{\circ}\mathrm{C}$, along with thermal ALD at $200\,^{\circ}\mathrm{C}$ and $350\,^{\circ}\mathrm{C}$. The targeted film thicknesses were $50\,\mathrm{nm}$ or $100\,\mathrm{nm}$ for Al_2O_3 and $50\,\mathrm{nm}$ for ZnO, depending on the deposition conditions. All thicknesses were confirmed by ellipsometry.

3.2.4 Nanoindentation testing

Nanoindentation tests were performed under ambient conditions using a G200 (KLA Corporation) system and an iNano (KLA-Nanomechanics) system. For all Continuous Stiffness Measurement (CSM) and pillar splitting tests on GC micro-pillars, a Berkovich tip was employed, while a cube corner diamond tip was used for pillar splitting tests on fused quartz micro-pillars to minimize the densification effects associated with a blunt tip. Machine compliance and the indenter area function were calibrated on a fused quartz reference sample before and after each test, following the procedure outlined by Oliver and Pharr [78].

The mechanical properties of the ALD coatings were characterized by nanoindentation using the continuous stiffness measurement (CSM) technique on coated silicon wafers. Indentation tests were performed using the iNano system at a constant strain rate of $0.2\,\mathrm{s}^{-1}$, with a maximum penetration depth of $100\,\mathrm{nm}$. For each coating, a 4 × 6 array of indents was performed. After excluding outliers due to surface effects or shallow-depth instability, at least 16 valid measurements were used to extract the elastic modulus and hardness. The elastic modulus was extracted using the Doerner–Nix model [88], while the film hardness was corrected for substrate effects using the Korsunsky model [90], as described in the Supporting Information. A Poisson's ratio of 0.26 was assumed for the coatings [167]. To enable accurate application of these models, the mechanical properties of the bare silicon substrate were independently measured. Nanoindentation was performed on uncoated silicon wafers using the

same instrument and strain rate, with a maximum depth of $500\,\mathrm{nm}$ and a 4×4 indentation array. A minimum of 12 valid indentations was retained to determine the substrate's modulus and hardness, which were then used as input parameters in the composite analysis of the coated films. For fused quartz, indentation was performed on uncoated substrate regions prior to film deposition using the G200 nanoindenter, at a strain rate of $0.05\,\mathrm{s}^{-1}$ and a depth of $500\,\mathrm{nm}$, also in a 4×4 array with at least 12 valid data points. The mechanical properties of glassy carbon were taken from prior work by the authors [160] and the Poisson's ratio of 0.17 was used from reported value [168].

The crack propagation resistance of micro-pillars with various coatings was evaluated through pillar-splitting experiments. This technique involved applying an indentation load to the pillars until fracture occurred, eliminating the need for post-test crack length measurements [105, 107, 120]. To ensure consistency in the splitting tests, a brand-new cube corner tip (MicroStar Technologies, nominal radius $\leq$20 nm) was used. Tip sharpness was regularly monitored, and the area function recalibrated to confirm stability over the entire test campaign. This minimizes the influence of tip blunting on crack initiation loads, as discussed in previous studies [108, 139]. As outlined in the FEM section, apparent fracture toughness (K_c) was calculated using the relationship provided in Equation (1.27). Nanoindentation pillar splitting tests were conducted on ALD-coated GC and fused quartz micro-pillars at a constant strain rate of $0.05\,\mathrm{s}^{-1}$ to assess their apparent fracture toughness. The surface roughness of both fused silica and pyrolytic glassy carbon pillars is in the nanometer range, and the conformal ALD coating further reduces surface asperities. Given that the coating thickness and the estimated process zone exceed the roughness scale by at least one order of magnitude, surface roughness is not expected to influence the measured fracture response. Uncoated GC and fused quartz micro-pillars were also tested as reference samples, with uncoated diameters of $5.3\,\mu\mathrm{m}$ and $5.16\,\mu\mathrm{m}$, respectively. The specific calibration coefficient (γ) for the materials was determined through polynomial interpolation of the γ versus E/H ratio function, as established in previous work by the authors [105]. To ensure accuracy in tip positioning [108], only experiments with indenter tips precisely centered on the pillar surface, within $0.5\,\mu\mathrm{m}$, were considered. The centering was verified through post-experiment scanning electron microscopy (SEM) imaging of residual marks on the substrate.

3.2.5 Residual stress measurement

Residual stress measurements were conducted on $12\,\mu\mathrm{m}$ GC micro-pillars and the unetched zone of fused quartz wafer using the Helios 5 CX system (Thermo Fischer Scientific). The ring-core FIB-DIC procedure developed by the authors in their prior works [123, 126, 127, 164] was utilized after ALD coating process. Tests were also performed on uncoated GC samples to establish a baseline for comparison. Several modifications to the published method were implemented to enhance both in-depth and lateral resolution, enabling stress measurements in thin films with an average thickness of $50\,\mathrm{nm}$.

For all cases studied, surface preparation involved the deposition of an ultra-thin sputter-coated gold layer using a $15\,\mu\mathrm{A}$ current for $20\,\mathrm{s}$ to enhance the DIC analysis. The gold layer was subsequently irradiated at low ion currents to achieve dewetting, as detailed by Winiarasky [169], utilizing a current of $1.5\,\mathrm{pA}$ at $30\,\mathrm{kV}$. Incremental material removal in the ring-core geometry was performed via a semi-automated procedure, ensuring precision and repeatability.

This modified method provides high sensitivity for stress measurements in the normalized depth range of $h/D = 0.015 - 2$ [123, 127]. To accommodate the film thickness, an annular trench with an inner diameter of $1\,\mu\mathrm{m}$ for GC samples and $0.7\,\mu\mathrm{m}$ for fused quartz samples was employed. Each milling step typically achieved a depth of approximately $2\,\mathrm{nm}$, except for the $100\,\mathrm{nm}$ coated samples where a milling depth of $4\,\mathrm{nm}$ per step was used to reduce the total number of milling steps required. These milling depths were achieved using a low ion milling current and, through precise calibration of milling depth versus ion dose, explicitly performed for each material via cross-sectional measurements of the milled geometries. Maintaining a consistent milling rate throughout the process ensured uniform partial depths after each incremental material removal. A total of 30 milling steps were utilized, corresponding to the film thickness and enabling evaluation of the residual stress depth profile from the surface to the substrate interface.

During the process, five high-resolution SEM micrographs were captured: one before testing and one after each material removal increment. These images were acquired under consistent contrast conditions, using an acceleration voltage of $2\,\mathrm{kV}$, a beam current of $43\,\mathrm{pA}$, and in immersion mode. Each image was integrated over 32 frames at a dwell time of $100\,\mathrm{ns}$

per frame. Cross-sectional depth measurements were performed on SEM high-resolution images of the lateral surfaces of the milled geometries to verify the final depth. Following image acquisition, a MATLAB-based digital image correlation (DIC) routine was used to track the incremental strain evolution by comparing each milled-step image to the initial, unprocessed surface. The obtained strain distribution was then utilized to reconstruct the residual stress profile based on the inverse problem approach of the FIB-DIC method, as detailed in Supporting information.

3.3 | Results

3.3.1 Finite element simulation of film stress effect on crack propagation during pillar splitting

The study focuses on the relative changes of crack propagation resistance in micro-pillars after adding films with various stress levels. Given the specific materials and indenter geometry used, the apparent fracture toughness is associated with the critical instability load, P_c, occurring during sharp nanoindentation of a micro-pillar, through the relationship described at Equation 1.27 [105]. Given this, the same γ value could be used for the simulations with various film stress levels. To quantify the variation in splitting load (φ), which serves as an indicator of relative changes in crack propagation resistance, the following expression is used:

$$\varphi = ((P_c - P_{\text{cref}})/P_{\text{cref}}) \tag{3.3}$$

where P_{cref} represents the critical load of the uncoated substrate pillar simulation. This approach aligns with experimental conditions, where uncoated samples serve as the reference. To understand the basic mechanisms, FEM simulations allow for the investigation of substrates with films that have no residual stress, isolating the influence of the film's mechanical properties. In practice, films with predefined residual stress states are applied to the substrate following the ALD process. This highlights the advantage of using simulations to systematically analyze the impact of film stress and mechanical properties on crack resistance.

3.3.1.1 Median crack geometry

The median mode crack propagation behavior can be observed in more detail in the supplementary video (Movie S1), where the crack originated beneath the contact area with the indenter and propagate vertically. Figure 3.3 shows how the thin film affects the apparent fracture toughness of the coated pillars. Since median crack propagation is predominantly governed by the substrate's bulk properties, the addition of coating with zero stress has a limited effect (Figure 3.S1). Specifically, $50\,\mathrm{nm}$ and $100\,\mathrm{nm}$ coatings with zero residual stress show minimal impact on the fracture resistance of the coated pillars, with the φ value varying within $\pm 2\%$. Compressive residual stress leads to a reduction in critical load, showing a clear linear trend. In contrast, tensile residual stress increases the system's apparent fracture toughness in a more parabolic fashion: apparent fracture toughness initially increases with tensile residual stress but eventually peaks and declines beyond a certain point. The thicker film (Figure 3.3b) exhibits a similar trend, albeit with a more significant slope. At the same tensile stress level, the thicker film can provide a higher toughening effect than the thin film. Furthermore, simulations with two levels of fracture energy for the film demonstrate that while compressive residual stress consistently reduced apparent toughness, higher fracture energy in the film leads to a greater increase in toughness under tensile stress.

It is important to note that the simulated tensile residual stress was capped at approximately $1000\,\mathrm{MPa}$. This limitation was set because, in the simulations at higher tensile stress levels, cracks would likely initiate and propagate within the film itself during the thermal step. However, in the model, the cohesive element plane was positioned based on the assumption that cracks from indentation would propagate along the indenter edge, which does not accurately capture crack behavior driven by residual stress alone. Therefore, results related to high tensile stress were excluded, as they do not accurately represent realistic conditions.

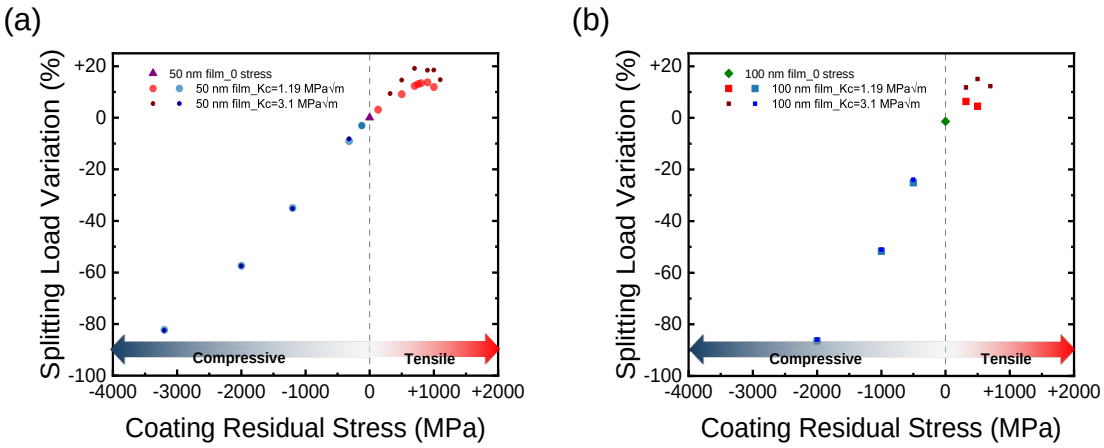

Fig. 3.3. The splitting load variation of the coated system with (a) $50\,\mathrm{nm}$ and (b) $100\,\mathrm{nm}$ ALD film on the ceramic substrate which develops median cracks as a function of the film residual stress.

3.3.1.2 Palmqvist crack geometry

When changing the property of the substrate material to develop Palmqvist crack, the Palmqvist cracks initiate near the free surface and propagate laterally within the coating (Movie S2). In our simulations, this behavior is captured by lateral crack growth confined to the film, with no interface decohesion, as perfect adhesion is assumed throughout. As a result, residual stress influences the cracking mechanism distinctly. To isolate the effect of the coating film's mechanical properties, the initial analysis considered a stress-free condition (Figure 3.S2). The addition of a $50\,\mathrm{nm}$ film significantly reduces the splitting load by approximately 12%, whereas the $50\,\mathrm{nm}$ film has minimal impact on the critical load (Figure 3.4). For thinner films, the substrate primarily dictates the mechanical response of the system due to its greater volume and structural dominance. Consequently, a low-toughness film provides minimal resistance to crack propagation, reducing the critical load required for crack initiation. However, as film thickness increases, the film's mechanical properties, particularly its strength and hardness, become more influential in resisting crack propagation. Thus, a thicker, stronger film enhances the system's overall fracture resistance, requiring a higher external load for crack initiation and propagation. The more detailed results are exhibited in the Supporting Information.

Unlike median cracks, both compressive and tensile residual stresses in the film reduce the system's apparent resistance to crack propagation. Notably, while thinner stressed films exhibit a greater relative reduction in fracture toughness, they also display a shallower slope in this

trend. This suggests that in the $50\,\mathrm{nm}$ film system, the primary reduction in fracture resistance arises from the film's lower mechanical toughness rather than the residual stress itself. In contrast, for thicker films, the residual stress plays a more significant role in influencing crack propagation resistance.

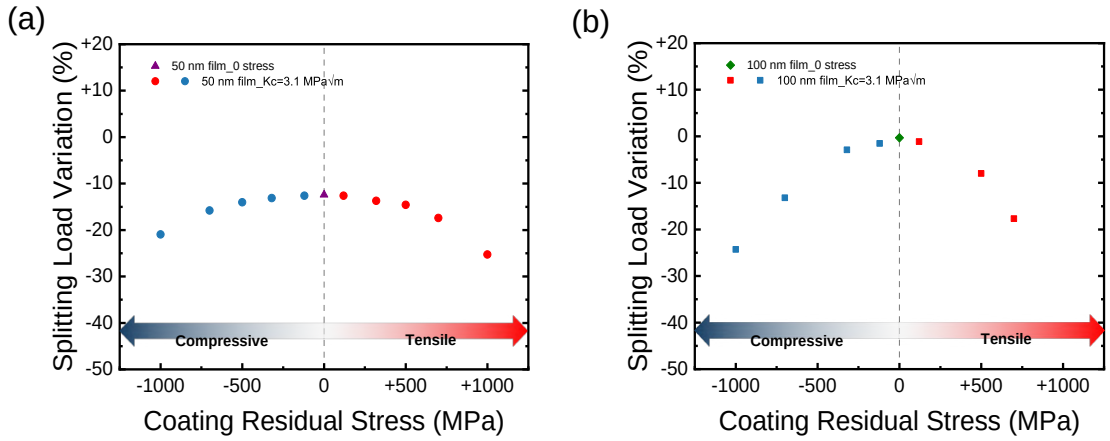

Fig. 3.4. The splitting load variation of the coated system with (a) $50\,\mathrm{nm}$ and (b) $100\,\mathrm{nm}$ ALD film on the ceramic substrate, which develops Palmqvist cracks as a function of the film residual stress.

3.3.1.3 Fracture mechanism of the coated system

The simulation results indicate that surface residual stress state influences crack systems differently, as the driving force responsible for crack opening varies between systems. As illustrated in Figure 3.5a, the median crack system typically forms beneath the plastic deformation zone under the indenter and propagates parallel to the loading axis. The primary driving force for crack propagation at the crack tip is the tensile stress surrounding the plastic deformation zone [170, 171]. In terms of stress equilibrium across the whole system, tensile stress in the film induces a corresponding compressive stress within the substrate pillar. As a result, a higher external load is required to initiate and propagate the crack. Conversely, compressive stress within the film generates a tensile stress field in the substrate, which significantly weakens the system's resistance to crack propagation.

This apparent reduction in toughness with increasing compressive residual stress may seem counterintuitive when compared to classical multilayer systems, where compressive surface stress typically reduces crack driving forces. However, this effect arises from the specific geometry and constraint conditions of our system. In our case, the micropillar is coated

conformally and constrained at its base, which imposes circumferential compatibility. As a result, compressive hoop stress in the ALD film induces a tensile stress field in the pillar core, enhancing the driving force for radial crack propagation. This mechanism differs fundamentally from planar multilayers under bending, as discussed in [161, 162], where residual stress acts near the surface and shields the crack tip. In contrast, the high surface-to-volume ratio of our pillars leads to stress penetration into the full cross-section, and the observed trend is a direct consequence of the confined geometry.

However, since the film cannot indefinitely sustain tensile residual stress, the toughening effect provided by residual stress is ultimately limited by the film's intrinsic fracture resistance (Figure 3.S3, 3.S4). When the residual stress approaches the failure threshold of the film, damage may accumulate during the thermal step, even if no visible cracking occurs. This pre-damaged state can trigger early crack initiation at the start of indentation, reducing the effectiveness of toughening. Additional simulations confirm that films with higher fracture toughness are better able to retain residual stress without early failure, allowing for greater stress transfer into the substrate. The details were shown in Supporting Information. Therefore, the extent of the toughening effect is not only governed by the magnitude of residual stress but also constrained by the crack resistance capability of the film itself.

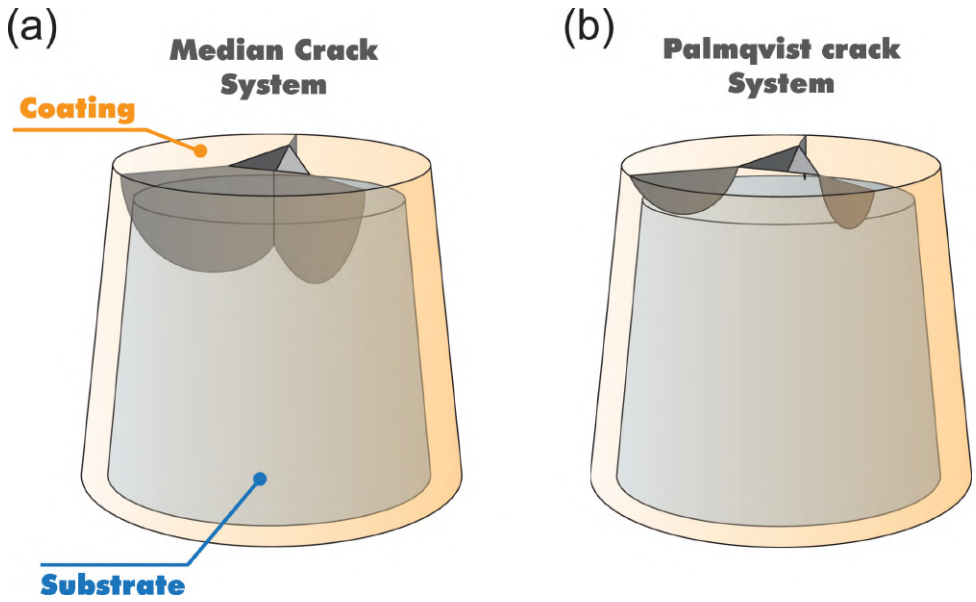

Fig. 3.5. Two cracking mechanisms achieved in ALD-coated pillars: (a) Median crack system develops through the substrate and reaches the coating; (b) Palmqvist crack system develops through the coating.

In contrast to the median crack, the maximum tensile stress for the Palmqvist crack system is located near the surface rather than along the indentation axis, which makes the crack originate close to the surface and propagate laterally (Figure 3.5b). When tensile residual stress is present in the film, it amplifies the tensile field near the surface, accelerating crack propagation and leading to complete fracture (Movie S3 and Figure 3.S5). This effect reduces the critical load required for crack initiation, as the surface tensile stress makes the crack more likely to open and extend laterally (as shown in the Figure 3.S5c-iv). Conversely, compressive residual stress in the film generates an opposing tensile stress within the substrate, which shifts the crack initiation zone from the surface to the subsurface region (Movie S4 and Figure 3.S5c-iii). This shift indicates a transition from a Palmqvist to a median crack, driven by the inward tensile field. Consequently, compressive stress within the film detrimentally affects crack resistance by promoting subsurface crack development.

To isolate the geometric effect of the coating from the influence of residual stress, additional simulations were performed with coatings of varying thickness but zero residual stress (Supporting Information, Figure 3.S1, 3.S2). These results show that film thickness alone does not significantly alter the splitting load in the absence of residual stress. However, when residual stress is introduced (Figure 3.3-3.4), the thicker films show a more pronounced reduction (in compressive cases) or increase (in tensile cases) in splitting load. This occurs because thicker coatings store more elastic energy and impose a stronger constraint or driving force onto the substrate, depending on the sign of the residual stress. The larger volume of stressed material in the thick coating amplifies the stress redistribution into the substrate, which in turn affects the crack driving force. This explains the observed trend of higher splitting-load sensitivity to residual stress in thicker films.

The simulation results show that the interaction between residual stress and crack propagation mechanisms is highly dependent on crack geometry, stress distribution, and film thickness. Stress equilibrium across the substrate-film system influences median cracks, while the surface stress fields influence Palmqvist cracks. These findings highlight the complex role of thin film residual stress in governing crack initiation and propagation, emphasizing the importance of tailoring stress levels and film properties to enhance system resistance against fracture. This is of predominant prevalence in the case of coated micro-architectures.

3.3.2 Experimental validation

3.3.2.1 Fused quartz

The residual stresses of ultra-thin ALD films on the two substrates were measured as a function of deposition parameters using the FIB-DIC method. Details of the stress calculation process are provided in Supporting information. Among the samples, only the $50\,\mathrm{nm}$ ZnO film on the fused quartz substrate exhibited compressive residual stress, measured at $-3100 \pm 610\,\mathrm{MPa}$ (Figure 3.6a). In contrast, all Al_2O_3 films on fused quartz exhibited tensile residual stress (Figure 3.6a). The highest residual stress, $2233 \pm 763\,\mathrm{MPa}$, was observed for the $50\,\mathrm{nm}$ Al_2O_3 film grown at $200\,^{\circ}\mathrm{C}$ on the fused quartz substrate. The thicker Al_2O_3 films grown at $300\,^{\circ}\mathrm{C}$ showed slightly lower residual stress values than the $50\,\mathrm{nm}$ Al_2O_3 film.

As shown in Figure S9, the loading curves of different tests for each sample show consistent tendencies, indicating that the position error coming from ex-situ tests was in the acceptable range for the pillar splitting method [108]. The scatter of critical instability load mainly depends on the individual differences between tested pillars. A slight pop-in plateau was observed for uncoated fused quartz samples before the completed failure, which only happened on the ZnO-coated fused quartz and Al_2O_3 grown using the plasma-enhanced technique. The pop-in event in ZnO-coated fused quartz occurred even earlier than in the uncoated fused quartz.

In this study, we considered the uncoated substrate to be the primary contributor to the mechanical response of the coated system, due to its significantly larger volume compared to the $50\,\mathrm{nm}$ thick ALD film. As a result, we applied the same γ coefficient, 0.56 for fused quartz to both the uncoated and coated samples. This γ value was determined from the modulus and hardness of the uncoated substrate using CSM measurements. While the presence of a thin coating may slightly influence the near-surface mechanical response, its impact on the overall E/H ratio is minimal in this configuration. Even when Palmqvist cracks initiate partially within the coating, the path of the crack and the energy dissipation are largely dictated by the substrate. This assumption is supported by Xia et al [116], who demonstrated that the composite E/H ratio remains effectively unchanged for coated systems when the thickness of the coating is small relative to the indentation depth and the dimensions of the substrate. Since we are focused on the apparent fracture toughness of the coated system, rather than the

intrinsic properties of the film, we maintained a constant γ value to ensure consistency across different coating conditions. The apparent fracture toughness was calculated from Equation (1.27). All the samples with ALD coatings exhibited higher apparent fracture toughness compared to the uncoated fused quartz (Figure 3.6b), except the $50\,\mathrm{nm}$ ZnO film resulted in a reduction. The samples with a $100\,\mathrm{nm}$ Al_2O_3 film grown at $300\,^{\circ}\mathrm{C}$ demonstrated nearly three times the apparent fracture toughness of the uncoated fused quartz. The $50\,\mathrm{nm}$ Al_2O_3 film, grown at the same temperature, showed lower apparent fracture toughness than the thicker coating but exhibited the biggest scatter in the critical load values. For a pillar coated with a $50\,\mathrm{nm}$ Al_2O_3 film at $300\,^{\circ}\mathrm{C}$, a splitting test was intentionally halted before fracture by setting the maximum load lower than the critical load. Indentation marks and focused ion beam (FIB) cross-section analysis of the residual indentation imprints revealed the presence of median cracks in the fused quartz substrate (Movie S5, Figure 3.7a). These cracks were observed in the cross-sectional view perpendicular to the indenter edge, where the crack openings extend beneath the contact surface with the indenter.

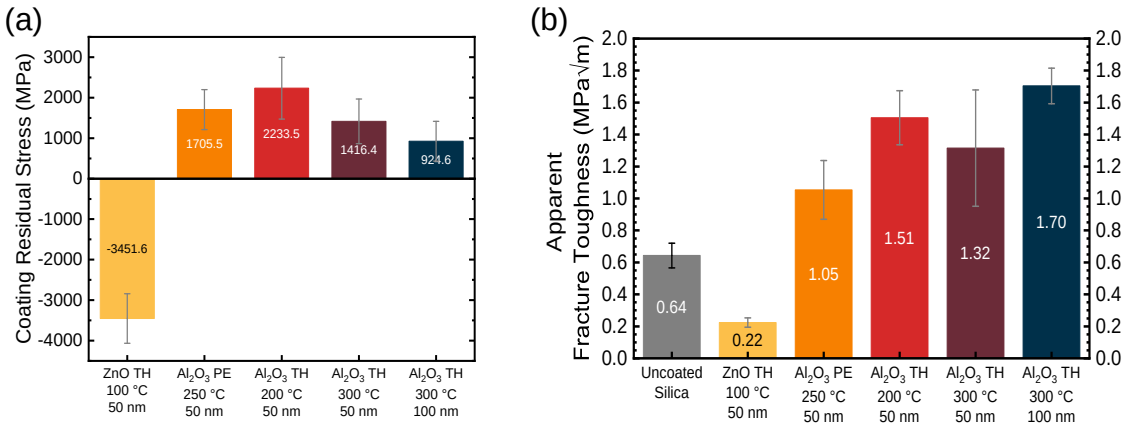

Fig. 3.6. (a) The residual stress of the ALD coating on fused quartz substrates; and (b) the apparent fracture toughness of ALD-coated fused quartz as a function of the deposition parameters. Error bars represent the standard deviation from multiple measurements, and are presented in the same manner for the figures below.

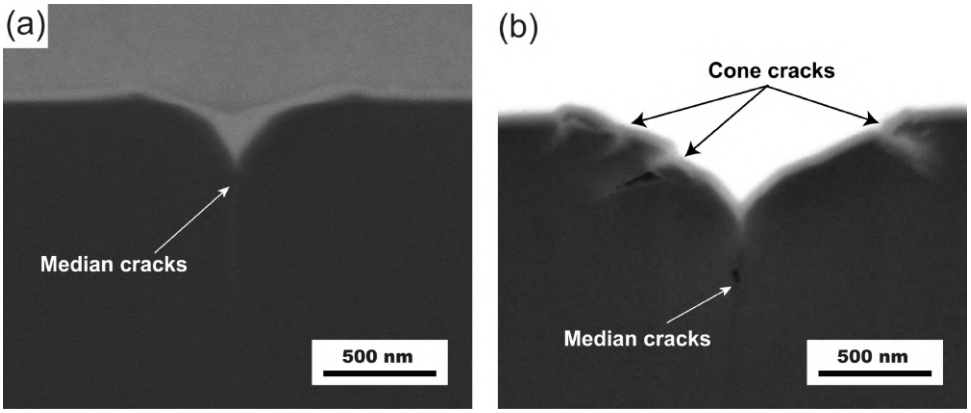

Fig. 3.7. FIB cross-section of the indent just before splitting failure of the (a) fused quartz coated with $50\,\mathrm{nm}$ Al_2O_3 at $300\,^{\circ}\mathrm{C}$; (b) glassy carbon coated with $50\,\mathrm{nm}$ Al_2O_3 via PE-ALD

3.3.2.2 Glassy carbon

Figure 3.8a illustrates the residual stress profiles for different coating parameters on the GC substrate. A similar trend was observed with the fused quartz substrate: the $50\,\mathrm{nm}$ Al_2O_3 film grown at $200\,^{\circ}\mathrm{C}$ exhibited the highest tensile residual stress. However, the stress reached only around $870\,\mathrm{MPa}$, approximately one-third of the value observed on the fused quartz substrate under identical deposition conditions. The other Al_2O_3 films also exhibited lower residual stress when deposited on the glassy carbon substrate compared to those on fused quartz. Furthermore, Al_2O_3 films fabricated using plasma-enhanced ALD showed lower tensile stress compared to their thermally deposited counterparts at the same deposition temperature.

In contrast to the performance of ALD-coated fused quartz, the pop-in plateau was observed in most of the ALD-coated samples but not the pristine glassy carbon pillars (Figure S10), indicating the early crack during the pillar splitting tests after adding the ultra-thin Al_2O_3 film. As clarified in Section 3.2.1, here the gamma coefficient of 0.19 was used to calculate the apparent fracture toughness of the uncoated and coated glassy carbon sample [160]. Each type of coating film led to a reduction of K_c value compared with the uncoated status (Figure 3.8b). The $50\,\mathrm{nm}$ Al_2O_3 film grown at $200\,^{\circ}\mathrm{C}$ caused the most significant loss. The other two Al_2O_3 films, deposited by plasma-enhanced ALD at $200\,^{\circ}\mathrm{C}$ and thermal ALD at $350\,^{\circ}\mathrm{C}$, resulted in slight reductions in fracture toughness. Figure 3.7b shows not only median cracks, but also cone cracks in the contact surface of the GC micro-pillar coated with Al_2O_3 film, which is consistent with the crack geometry of uncoated GC [160].

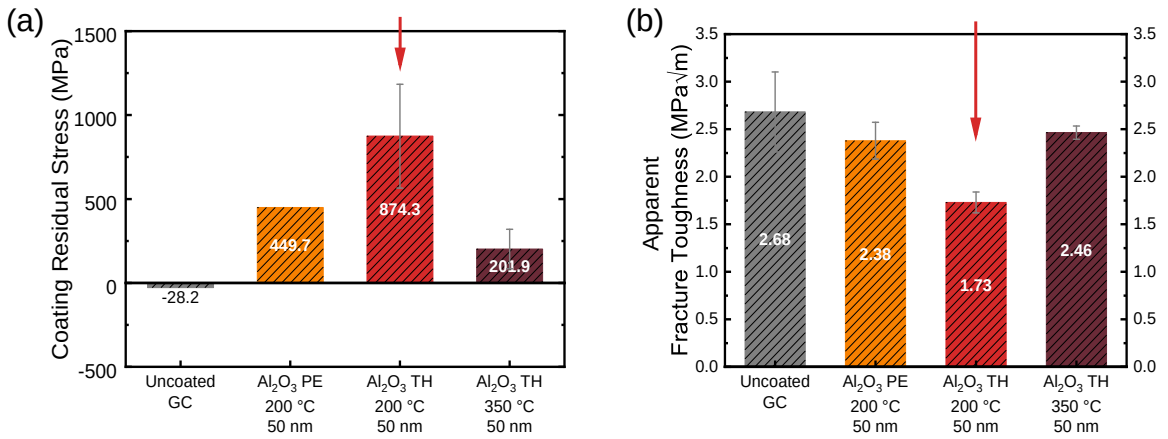

Fig. 3.8. (a) The residual stress of the ALD coating on glassy carbon substrates; and (b) the apparent fracture toughness of ALD coated glassy carbon as a function of the deposition parameters. (The red arrow was used to highlight the sample showing highest stress level and lowest apparent fracture toughness)

Figure 3.9 illustrates the relationship between apparent fracture toughness and residual stress, with the right axis indicating the relative change in apparent fracture toughness compared to the uncoated sample. For the $50\,\mathrm{nm}$ Al_2O_3 film on a fused quartz substrate, the apparent fracture toughness increases with tensile residual stress. The Al_2O_3 film deposited at $200\,^{\circ}\mathrm{C}$ exhibited the highest tensile residual stress, leading to an approximate 140% improvement in system fracture toughness. Interestingly, the $100\,\mathrm{nm}$ Al_2O_3 film deposited at $300\,^{\circ}\mathrm{C}$ showed the lowest tensile strength than other films but provided the highest toughen effect, demonstrating a substantial 165% increase in fracture toughness compared to uncoated fused quartz. In contrast, ZnO films, which exhibited compressive stress, displayed a different behavior. "Pop-in" events were observed around $300\,\mathrm{nm}$ in the load-displacement curves, indicating the initiation of early cracks during pillar splitting tests. From Figure 3.9b, all the tensile stresses in Al_2O_3 film resulted in a reduction in the fracture toughness of ALD-coated GC compared with the uncoated one, showing a reverse tendency for the fused quartz. Although the apparent fracture toughness values for the PE $200\,^{\circ}\mathrm{C}$ and TH $350\,^{\circ}\mathrm{C}$ Al_2O_3-coated samples show only modest reductions compared to the uncoated glassy carbon and fall within the bounds of experimental scatter, they remain fully consistent with the monotonic trend observed in both the normalized toughness plot (Figure 3.9b) and the FEM simulations. The PE $200\,^{\circ}\mathrm{C}$ and TH $350\,^{\circ}\mathrm{C}$ coatings induce moderate tensile residual stresses that, while lower in magnitude, still contribute to an increase in the crack driving force. In glassy carbon, which exhibits

flaw-sensitive fracture, the influence of residual stress on toughness becomes increasingly apparent only when the stress field reaches a scale comparable to the crack tip energy release rate. This explains why the largest reduction is observed in the TH $200\,^{\circ}\mathrm{C}$ sample, which exhibits the highest tensile stress ($874\,\mathrm{MPa}$). The overall behavior confirms that the effect of residual stress on fracture is progressive and mechanically driven, even if not all intermediate steps are statistically resolved in isolation.

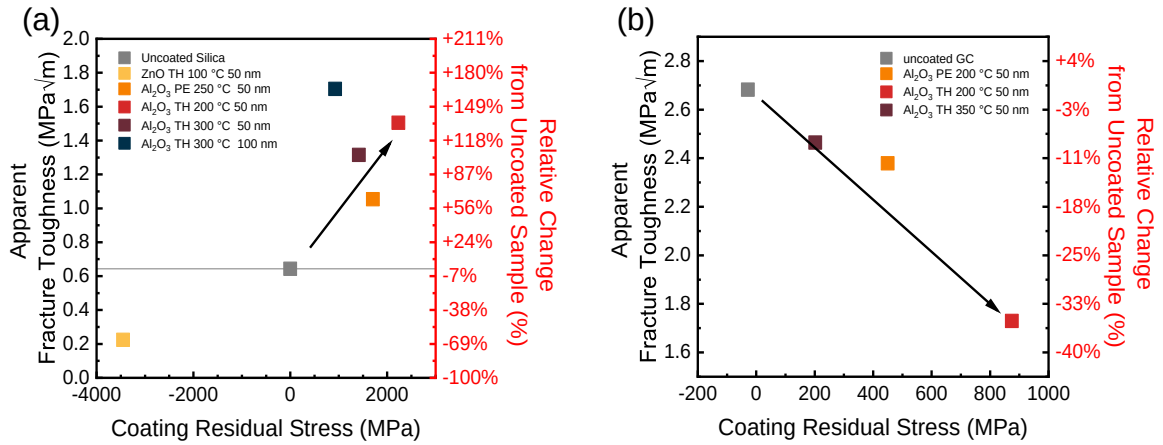

Fig. 3.9. The apparent fracture toughness as a function of the residual stress of ALD film on (a) fused quartz and (b) GC substrate. Error bars are omitted for clarity, as they have been presented in Figure 3.6 and Figure 3.8 above.

3.4 | Discussion

3.4.1 Residual stress from ALD coating process

Importantly, ALD-deposited Al_2O_3 films are more accurately represented as amorphous AlO_xH_y, especially when deposited at lower temperatures (e.g., ~$200\,^{\circ}\mathrm{C}$). These films are hydroxyl-rich and exhibit incomplete network formation due to low atomic mobility during deposition, leading to limited structural relaxation. This chemical and structural nature plays a central role in the development of intrinsic tensile stresses [57]. Residual stress in ALD coatings originates primarily from two mechanisms: growth-induced stress and thermal stress. Growth-induced stress is dominant and stems from ALD's self-limiting, layer-by-layer deposition process, where each cycle incrementally introduces strain that accumulates with increasing film thickness. This stress is exacerbated in thinner films due to fewer opportunities for relaxation. Strategies such as plasma-enhanced ALD, thermal ALD at high temperature,

and increased film thickness can improve network condensation, reduce hydroxyl content, enhance film densification, and facilitate stress relaxation—all of which contribute to reducing growth-induced stress, as corroborated by our FIB-DIC results. In comparison, thermal stress arises from mismatches in the thermal expansion coefficients between the film and the substrate during cooling from deposition temperatures. This can be estimated through Equation (3.1). Using representative thermal expansion values, fused quartz ($\alpha_{s1} \approx 0.5 \times 10^{-6}\mathrm{K}^{-1}$) [172], glassy carbon ($\alpha_{s2} \approx 4.3 \times 10^{-6}\mathrm{K}^{-1}$) [173], and ALD-grown Al_2O_3 ($\alpha_f \approx 4.2 \times 10^{-6}\mathrm{K}^{-1}$) [57], and considering deposition temperatures between $200\,^{\circ}\mathrm{C}$ to $300\,^{\circ}\mathrm{C}$, the resulting thermal stress is estimated at ~$130\,\mathrm{MPa}$ to $250\,\mathrm{MPa}$ on fused quartz and near-zero on glassy carbon. Since this accounts for only 10–20% of the total tensile stress observed, it confirms that growth-induced stress is the dominant component in our films. It is important to note that the residual stresses measured in each film are not microstructurally independent quantities. On the contrary, they arise from the intrinsic evolution of density, porosity, hydrogen incorporation, and interfacial bonding during ALD growth, as discussed in prior studies [57, 61]. In this sense, residual stress functions as a microstructurally-integrated parameter that captures the net mechanical effect of these nanoscale features. Cross-sectional TEM confirmed that all coatings were fully amorphous and well adhered to the substrate (Figure 3.S6, supporting the use of residual stress as a robust, quantitative descriptor linking film structure to fracture behavior.

The experimental results align with these mechanisms. The plasma in PE-ALD of Al_2O_3 promotes more complete surface reactions and enhances film densification of Al_2O_3, leading to reduced residual stress levels compared with those in thermally grown films [62]. Films deposited at $300\,^{\circ}\mathrm{C}$ exhibited the lowest residual stress, attributed to improved growth uniformity and enhanced stress relaxation enabled by the elevated deposition temperature. Conversely, the $50\,\mathrm{nm}$ Al_2O_3 film deposited at $200\,^{\circ}\mathrm{C}$ displayed the highest residual stress, reaching nearly $2233\,\mathrm{MPa}$. This elevated stress level likely arises from incomplete film densification and greater strain accumulation due to the lower deposition temperature, which limits stress relaxation. The measured residual stress values in this study significantly exceed those reported in previous works [57, 59, 62, 174], a discrepancy that can be attributed to the unique properties of ultra-thin films. Ultra-thin Al_2O_3 films deposited via ALD are well-known for their exceptional mechanical performance, which allows them to sustain extraordinarily high residual stresses

without failure. For instance, these films can endure residual stresses of up to $6\,\mathrm{GPa}$ [175] and demonstrate strengths of approximately $5.5\,\mathrm{GPa}$ in bulge tests [176], values that are nearly 20 times higher than those of bulk Al_2O_3. This remarkable resilience is primarily due to the unique mechanical characteristics of ultra-thin films. Unlike bulk materials, these films exhibit elevated elastic limits and improved resistance to crack propagation, arising from their nanoscale dimensions and geometrical constraints. While ALD's layer-by-layer growth offers excellent control over film thickness and uniformity, the resulting structure is not necessarily densely packed. Elastic strain and the presence of hydroxyl groups can lead to slight structural openness or nanoporosity. Nevertheless, the high uniformity and low defect density achieved in ALD films contribute to their impressive mechanical robustness, enabling them to sustain stress levels far exceeding those of bulk Al_2O_3. These findings emphasize the critical interplay between thickness, deposition temperature, and growth mechanisms in determining the stress behavior of ALD-grown films.

Since glassy carbon has a lower elastic modulus compared to fused quartz, the GC substrate can undergo more significant elastic deformation under stress. This enhanced deformability allows GC to accommodate better and dissipate stresses that develop during film deposition and subsequent thermal cycling, reducing the buildup of residual stress within the film. Additionally, the thermal expansion coefficient mismatch between GC and Al_2O_3 is smaller than that between fused quartz and Al_2O_3. As a result, Al_2O_3 films on GC substrates exhibit the same trend in residual stress behavior but with consistently lower values compared to films on fused quartz substrates.

At low temperatures, ZnO tends to grow in an amorphous state, especially when the film thickness is thin, as thinner layers inhibit crystallinity [177]. In this study, an ultra-thin amorphous ZnO film was created under the low-temperature deposition ($100\,^\circ\mathrm{C}$). Unlike Al_2O_3 films, ZnO has a relatively higher atomic packing density compared to many substrates, which induces compressive residual stress. This compressive stress becomes more pronounced as film thickness decreases due to limited relaxation pathways in thinner films [178].

3.4.2 Fracture mechanism of ALD coated glassy-carbon and fused quartz

Figure 3.9 illustrates the distinct effects of residual stress on the fracture mechanisms of fused quartz and glassy carbon, which is related to their different crack geometry in Figure 3.7. The observed trends align well with FEM simulation results, where the median-mode cracking in fused quartz was influenced by stress distribution. Tensile stress in the Al_2O_3 film contributes to compressive stress in the substrate, leading to a toughening effect for the entire system in the case of median crack geometry. Conversely, compressive stress in the film induces tensile stress in the substrate, which can trigger early cracks, as seen in the ZnO-coated samples during pillar splitting tests. Notably, the $100\,\mathrm{nm}$ -thick Al_2O_3 coating deposited at $300\,^{\circ}\mathrm{C}$ exhibits a significantly higher apparent fracture toughness compared to the $50\,\mathrm{nm}$ coating at similar residual stress levels. While FEM simulations predict a modest increase in splitting load (less than 5%) due to geometric effects alone, the experimentally observed enhancement is substantially larger. This suggests that additional energy dissipation mechanisms may be active in thicker coatings. Possible contributors include localized plasticity, partial interface sliding, or distributed microcracking within the amorphous Al_2O_3 film. Such effects can redistribute stress near the crack tip, thereby delaying the onset of fracture. Although not explicitly modeled in the present framework, these mechanisms are plausible under high constraint and tensile stress in thicker films and likely contribute to the enhanced crack resistance observed experimentally.

However, the experimentally observed gains in fracture toughness for samples under tensile stress were significantly higher than those predicted by FEM simulations. This discrepancy arises because the simulation employs restricted constraint conditions, such as simplified fracture energy and critical plane assumptions, to streamline the analysis. These simplifications, while necessary for computational feasibility, can introduce artificial artifacts that deviate from real-world behavior. For instance, ultrathin Al_2O_3 films may exhibit enhanced crack resistance at the nanoscale [175, 176], allowing them to sustain higher tensile stress and, in turn, enabling greater compressive stress to be transferred into the pillar, thereby further toughening the system, while this is limited in the simulation (Figure 3.S3, 3.S4). Furthermore, additional complexities such as interfacial sliding, distributed microcracking, or time-dependent

stress relaxation were not implemented in the current model to maintain a well-controlled and interpretable simulation framework, which would make the simulation underestimate the toughening effect in real situation.

In the simulation, the toughening effect begins to diminish at higher tensile stress levels (Figure 3.3), primarily due to the film approaching its fracture limit and accumulating pre-damage, this trend was not evident in the experimental data within the tested stress range. One possible explanation is that the fracture toughness of the actual ALD film may exceed the conservative values used in the simulation, allowing it to withstand greater tensile stress without initiating early failure. As a result, the toughening effect in experiments continued to increase, whereas the simulation predicted an eventual plateau or decline.

Another noteworthy point is the noticeable variation observed in the sample with a $50\,\mathrm{nm}$ film deposited at $300\,^{\circ}\mathrm{C}$ highlighting the system's sensitivity to processing conditions and local stress states. This sample lies in a transitional regime, combining moderate tensile residual stress (around $1150\,\mathrm{MPa}$) with intermediate film toughness. Although neither parameter is extreme, their interplay creates a stress-sensitive condition where small variations in thickness, interfacial quality, or film properties can significantly alter crack initiation and stress redistribution. This underscores the need for further studies on the size- and processing-dependent fracture behavior of ultrathin films and the development of models capable of capturing spontaneous cracking and complex failure processes.

Different from the fused quartz, the cone crack system in the near-surface of the coated GC micro-pillars makes the residual stress play a different role in the mechanism. In the cone crack system, ring cracks initiate due to high tensile stress near the contact edge, which can be observed on the contact surface. Given the similarities between cone cracks and Palmqvist cracks, that both of them initiate near the free surface and are driven by tensile hoop stress, the GC is expected to behave similarly to a substrate that develops Palmqvist cracks under residual stress. So, the tensile stress in the film would result in the early cracks and speed up the fracture behavior, leading to embrittlement.

It is also worth noting that while localized densification of the amorphous $\mathrm{AlO}_x\mathrm{H}_y$ coating under indentation is theoretically possible—particularly under the high stress concentration of a cube-corner indenter, its effect is expected to be limited in fused quartz samples. In

these cases, fracture occurs predominantly within the substrate (via median cracking), and the coating primarily modulates the residual stress environment. However, for glassy carbon substrates, where surface-initiated cracks (e.g., Palmqvist or cone-like) dominate, the stress field from indentation may interact more significantly with the coating. Local densification of the amorphous layer could reduce compressive constraint in the vicinity of the indentation site, thereby contributing to the observed reduction in apparent toughness enhancement in coated GC samples.

3.4.3 Generalization to complex shaped coated architectures

In this study, core-shell pillars were selected as a simplified 3D model to analyze the effects of residual stress through a pillar splitting test, which offers a well-controlled experimental approach to understanding the fracture mechanism. The test results indicate that multiple factors, including substrate mechanical properties, crack geometry, film thickness, and surface residual stress govern crack propagation resistance. In particular, crack geometry plays a critical role in determining how residual stress affects crack propagation, as different crack shapes and orientations can lead to varying fracture behaviors.

While simple pillar structures provide fundamental insights, real-world applications demand the use of more complex micro-architectures, often realized through advanced fabrication techniques such as 3D printing. In these architected materials, residual stress interacts with geometric features to create unique mechanical responses. Unlike homogeneous materials, micro-lattices feature nodes and trusses with varying stress concentrations. Stress concentrations influence the mechanical behavior of nanolattice architectures and crack initiation sites, which predominantly occur at structural junctions. For example, In rigid stretching-dominated architectures, such as octet-truss lattices, nodes experience higher stress concentrations due to force transmission across multiple trusses, making them the most vulnerable points for crack initiation. Optimizing stress distribution at these locations is crucial for improving the mechanical resilience of the structure. This work provides another potential approach regarding interface engineering, aside from topology design, to improve mechanical reliability.

Building upon the results from the pillar splitting test, it is evident that different residual stress states can significantly affect crack resistance. By controlling the residual stress

distribution within micro-architectured metamaterials, it is possible to enhance mechanical properties strategically. For instance, introducing beneficial compressive stress at the weakest points through surface tensile residual stress, such as nodes in rigid stretching-dominated structures, can enhance their toughness. Simultaneously, leaving less advantageous stress states in non-critical regions minimizes potential failure risks without compromising the overall performance of the material.

Future advancements should focus on integrating computational modeling and experimental approaches to engineer residual stress distributions in these complex architectures precisely. By leveraging advanced fabrication techniques, such as controlled thermal treatments and stress-engineered deposition processes, tailored stress states can be achieved. This approach holds significant promise for designing high-performance, damage-tolerant metamaterials suitable for structural, aerospace, and biomedical applications.

3.5 | Conclusions

This study investigated the influence of ALD coatings on the crack propagation resistance of core-shell 3D-printed fused quartz and glassy carbon micro-ceramics, with a specific focus on Al_2O_3 and ZnO coatings produced via thermal and plasma-enhanced ALD. High-resolution FIB-DIC measurements provided critical data on residual stress evaluation. By utilizing the pillar splitting method, it was observed that ALD coatings can either enhance or degrade apparent fracture toughness depending on the material and stress level. CZ-FEM models were used to incorporate with the experiment and help understand fracture mechanisms deeper.

Firstly, FEM simulations highlight the dual effects of ALD-induced residual stress on crack behavior. Tensile stress in the coating is shown to enhance the apparent fracture toughness of the system when median cracks are present since it induces compressive stress in the underlying material, whereas compressive stress causes a reduction. Conversely, both tensile and compressive residual stresses lead to embrittlement when Palmqvist cracks develop in the substrate.

Experimental synthesis demonstrates that fused quartz micro-pillars achieved remarkable toughness gains of 134% with $50\,\mathrm{nm}$ Al_2O_3 coatings at $200\,^{\circ}\mathrm{C}$, driven by the large tensile

residual stress in the film. In contrast, $100\,\mathrm{nm}$ Al_2O_3 coatings at $300\,^{\circ}\mathrm{C}$ led to a 165% increase in toughness, attributed to the thicker film compensating for the smaller residual stress. On the contrary, the ZnO coating film with compressive stress induced the early crack of fused quartz micropillars. However, glassy carbon micro-pillars exhibited a reduction in apparent fracture toughness due to the tensile stress of Al_2O_3 coating and its cone crack geometry. This underscores the material-specific responses to ALD coatings and residual stress effects.

By integrating experimental and computational approaches, this work advances the understanding of residual stress and its role in the fracture behavior of micro-ceramic systems. This observation highlights the tremendous potential of stress engineering via ALD coatings to fine-tune the fracture toughness and improve mechanical reliability. The next step would be to promote these strategies to micro-architected metamaterials and take into account both the interface engineering and the topology structures.

3.6 | Supporting information

3.6.1 Finite element simulation

3.6.1.1 The interplay of film and substrate via mechanical properties

To investigate the role of inherent mechanical properties on the fracture behavior of ALD-coated micro-ceramic pillars, pillar splitting simulations were conducted under zero residual stress with varying film thicknesses. The results are presented in Figure 3.S1 and Figure 3.S2. The fracture behavior of coated systems in pillar splitting is predominantly governed by the interplay between film toughness, film thickness, and the mechanical mismatch between the film and substrate.

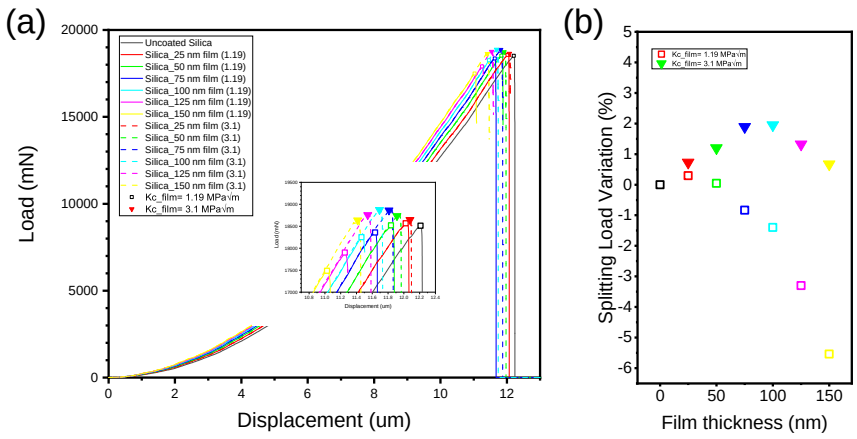

Fig. 3.S1. (a) Load–displacement curves from FEA simulations of pillar splitting for a substrate developing median cracks, coated with films of various thicknesses under zero residual stress. (b) Splitting load variation of the coated system as a function of film thickness. The thickness values are scaled to match the simulated reference condition.

As shown in Figure 3.S1, where the substrate develops median cracks, ultra-thin films have only a slight influence on the system's fracture toughness. This is because median cracks are stress-driven and propagate from the substrate bulk toward the surface under indentation. As film thickness increases, the coating provides limited shielding of the substrate, resulting in a modest enhancement of toughness. However, with further increase in thickness, especially when the film has a significantly higher E/Y ratio than the substrate, the stored elastic energy increases. This additional energy contributes to crack initiation and propagation, leading to a more brittle response. Despite this, the variation in fracture toughness remains within a

relatively small range (<2%) since median crack formation is largely governed by the substrate properties. Additionally, when a softer film (Kc = 1.19 $\mathrm{MPa}\sqrt{\mathrm{m}}$) is applied, its inability to effectively shield the substrate and its tendency to act as a stress concentrator further reduces the system's effective toughness.

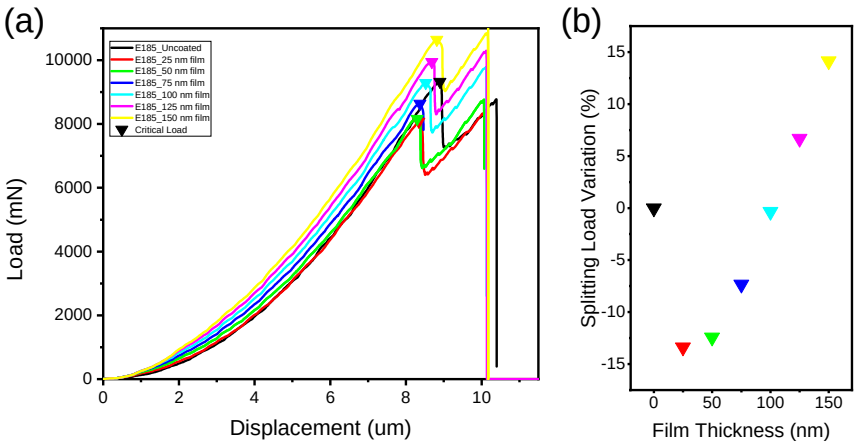

Fig. 3.S2. (a) Load–displacement curves from FEA simulations of pillar splitting for a substrate developing median cracks, coated with films of various thicknesses under zero residual stress. (b) Splitting load variation of the coated system as a function of film thickness. The thickness values are scaled to match the simulated reference condition.

In contrast, Figure 3.S2 illustrates the behavior of substrates that develop Palmqvist cracks, a surface-dominated cracking mode. In this case, ultra-thin hard films introduce stress localization at the film-substrate interface due to mechanical mismatch, promoting crack initiation. Since Palmqvist cracks are more sensitive to surface stress distribution, these effects are more pronounced. However, as the film thickness increases to $100\,\mathrm{nm}$ and beyond, the tougher coating begins to bear more load and effectively redistributes stress. This delay in crack propagation results in system performance that approaches, or even surpasses, that of the uncoated substrate at $50\,\mathrm{nm}$ thickness. These results are consistent with the surface crack-dominated mechanism observed in Palmqvist fracture behavior.

3.6.1.2 Median crack geometry

Figure 3.S3 illustrates the variation in crack propagation behavior for substrates developing median cracks, coated with $50\,\mathrm{nm}$ films under different levels of residual tensile stress. As the residual stress increases from $700\,\mathrm{MPa}$ to $1100\,\mathrm{MPa}$, the film approaches its failure limit. Although no cracking occurs during the thermal step, a high SDEG region emerges at

1100 MPa, indicating significant damage accumulation within the film. This pre-damaged state leads to crack initiation at the very onset of indentation, with initial propagation occurring along the film. As a result, the fracture toughness gain is reduced to 14%, compared to 19% observed at 700 MPa.

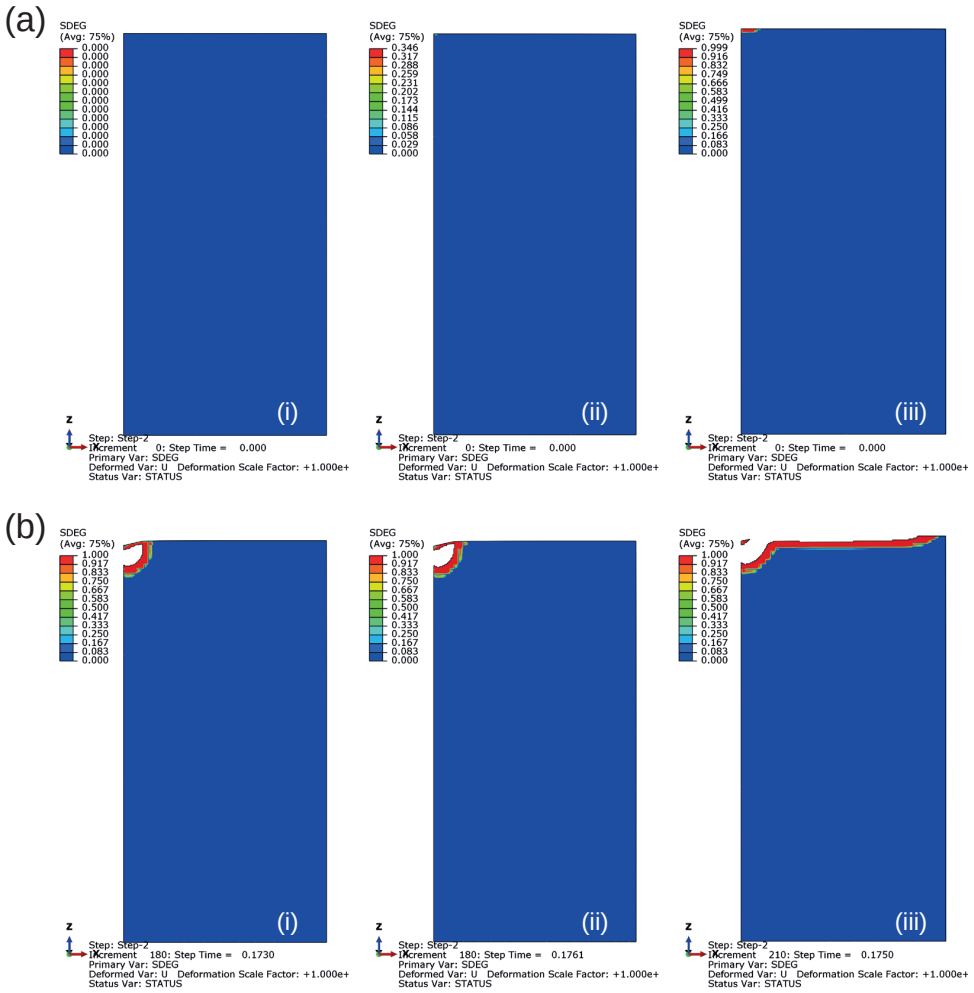

Fig. 3.S3. SDEG parameter distribution showing (a) the initial condition of the indentation step, and (b) crack propagation in micro-ceramic pillars coated with 50 nm ALD film (Kc = 3.10 MPa$\sqrt{m}$). The residual stress in the coating is (i) 700 MPa, (ii) 900 MPa, (iii) 1100 MPa. The substrate is modeled to develop median cracks.

To further investigate the effect of film properties on system toughening, 50 nm films with varying fracture energies were applied to micro-ceramic pillars designed to develop median cracks, all subjected to a tensile residual stress of 1200 MPa. As shown in Figure 3.S4, the less tough films exhibit early crack initiation during the thermal step (Figure 3.S4a-i, ii), whereas no cracking is observed in the tougher film. In this case, the residual stress remains well distributed throughout the film and along the interface (Figure 3.S4b-iii), and a higher level

of compressive stress is introduced into the substrate, leading to a splitting load variation to be 16%, which is higher than the 2% of other two cases in Figure 3.S4-i and 3.S4-ii. These results demonstrate that a tougher film can sustain higher tensile stress without premature failure and suggest that increased compressive stress can be more effectively transferred into the substrate under such conditions.

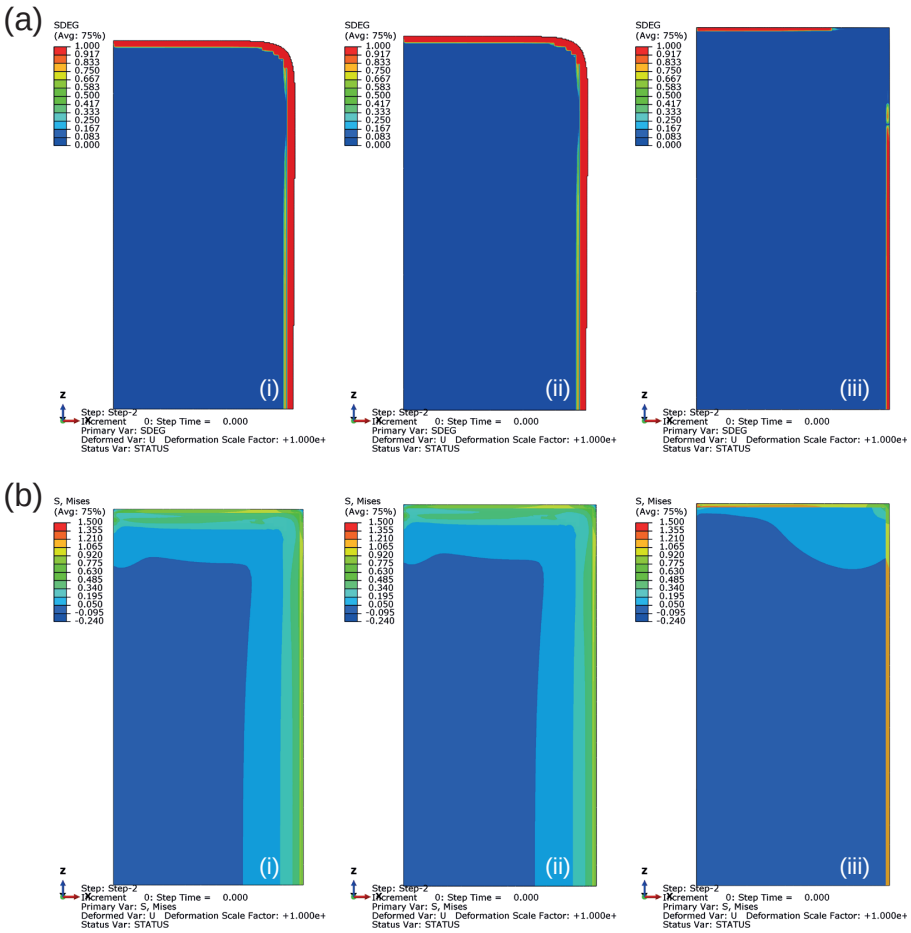

Fig. 3.S4. Comparison of (a) SDEG parameter showing crack state and (b) corresponding von Mises stress distribution at the beginning of the indentation step in $50\,\mathrm{nm}$ ALD-coated micro-ceramic pillars with $1200\,\mathrm{MPa}$ tensile residual stress. The simulations consider different film fracture toughness values: (i) $1.19\,\mathrm{MPa}\sqrt{\mathrm{m}}$, (ii) $3.10\,\mathrm{MPa}\sqrt{\mathrm{m}}$, (iii) $4.38\,\mathrm{MPa}\sqrt{\mathrm{m}}$. The substrate is modeled to develop median cracks.

3.6.1.3 Palmqvist crack geometry

The effect of different residual stress conditions on substrates developing Palmqvist cracks is illustrated in Figure 3.S5. Tensile residual stress in the film promotes crack propagation along the free surface, whereas compressive stress tends to redirect the crack path from the surface into the substrate interior.

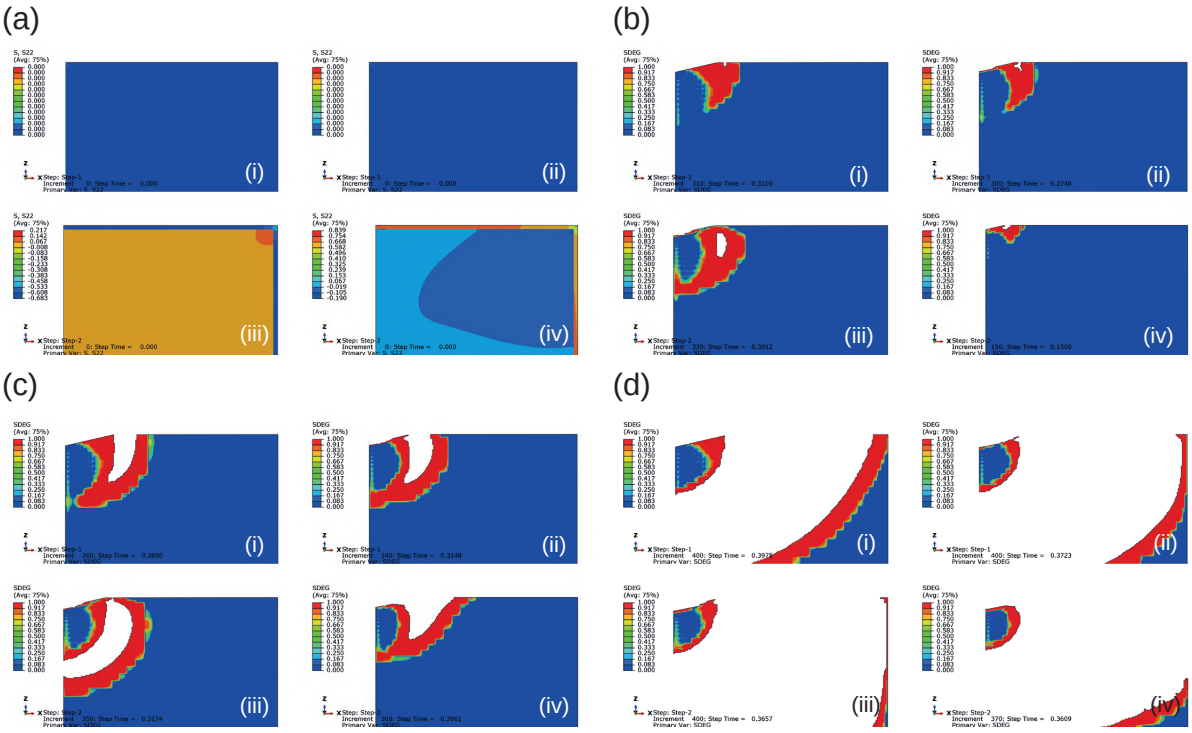

Fig. 3.S5. (a) Residual stress distribution among the whole structure (S22 represents σ_{yy}). SDEG parameter and showing fracture evolution for a substrate developing Palmqvist cracks under different residual stress conditions: (b) Crack initiation, (c) Crack propagation, (d) Crack reaching the pillar edge leading to complete failure.Each subfigure represents a different coating configuration: (i) uncoated pillar, pillar coated with a $50\,\mathrm{nm}$ film under (ii) zero residual stress, (iii) – $700\,\mathrm{MPa}$ residual stress (compressive), (iv) + $700\,\mathrm{MPa}$ residual stress (tensile).

3.6.2 Experiment validation

3.6.2.1 ALD coatings

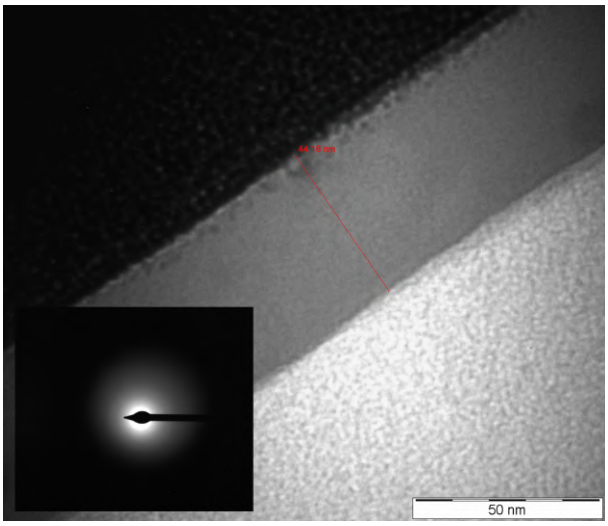

Fig. 3.S6. Cross-sectional TEM image of an Al_2O_3-coated glassy carbon pillar, with SAED inset. The absence of diffraction rings confirms the amorphous structure of the ALD film. The coating is continuous and well adhered to the substrate, with no visible defects or delamination.

3.6.2.2 Deconvolution of Mechanical properties of Ultra Thin Films

Based on the CSM results for various coating films on silicon wafers (Figure 3.S7), the effect of the substrate was considered through Doerner and Nix's model [88], and Korsunsky's model [90] to get the elastic modulus and hardness of the thin films [87].

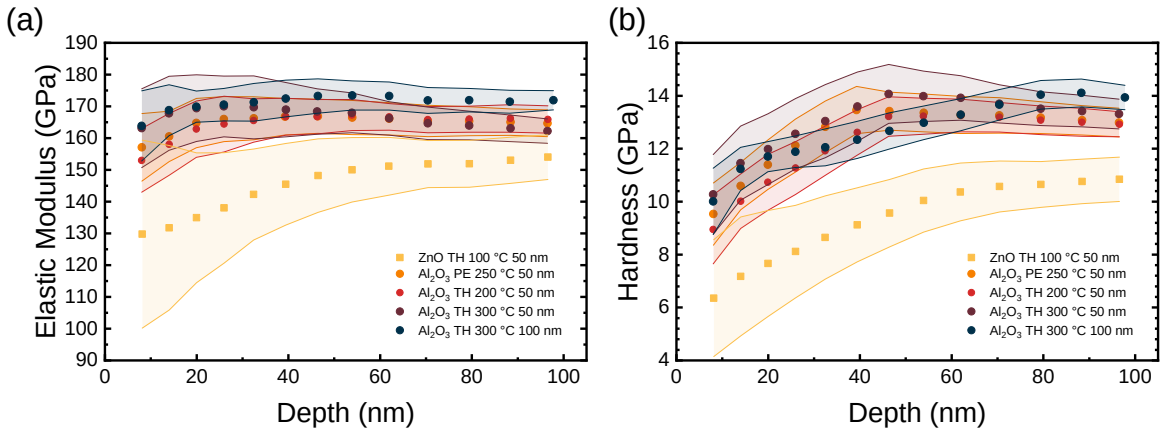

Fig. 3.S7. The (a) elastic modulus, and (b) hardness of different ALD coated silicon as a function of indentation depth.

The effect of the substrate on the elastic modulus of thin films was first addressed by Doerner and Nix through their proposed relationship [88]:

$$E_r = \left[\frac{1-\nu_f^2}{E_f}\left(1-e^{-\alpha t/h_c}\right) + \frac{1-\nu_s^2 e^{-\alpha t/h_c}}{E_s} + \frac{1-\nu_i^2}{E_i} \right]^{-1}, \tag{3.4}$$

where E_r is the reduced modulus, ν_i and E_i are the Poisson's ratio and elastic modulus of the indenter (0.07 and $1140\,\mathrm{GPa}$, respectively), t is the film thickness, and α is an empirical constant. To treat the film-substrate system as a composite material, the following equation is used:

$$\frac{1-\nu_c^2}{E_c} = \frac{1-\nu_f^2}{E_f}\left(1-e^{-\alpha t/h_c}\right) + \frac{1-\nu_s^2 e^{-\alpha t/h_c}}{E_s}. \tag{3.5}$$

Here, ν_c and E_c represent the Poisson's ratio and elastic modulus of the composite system, where ν_c =0.26 and E_c is the measured modulus obtained from CSM tests using the iNano instrument (Figure 3.S7 (a)). For the substrate, which is silicon in this work, E_s=$172\,\mathrm{GPa}$ and ν_s = 0.27. The film's Poisson's ratio ν_f is 0.23. The elastic modulus of the film E_f and

the empirical constant α were determined by curve fitting the experimental data of E_c as a function of the contact depth h_c.

Korsunsky et al [90] proposed a model to describe the influence of the substrate on the hardness of thin films:

$$H_c = H_s + \frac{H_f - H_s}{1 + \left[\left(\frac{h_c}{t}\right)/\beta_0\right]^X}, \tag{3.6}$$

where H_f and H_s are the intrinsic substrate and film hardness, respectively, β_0 and X are two fitted constants. The H_f can be obtained by curve fitting the experimental data of H_c plotted against contact depth h_c.

The final result after curves fitting from the models of the elastic modulus and hardness for different thin film was shown in Figure 3.S8. The ZnO film displayed a lower elastic modulus and hardness compared to the Al_2O_3 film. Additionally, as the deposition temperature increased, a slight enhancement in both elastic modulus and hardness was observed for the Al_2O_3 film. The result would be used in the residual stress calculation for the FIB-DIC method.

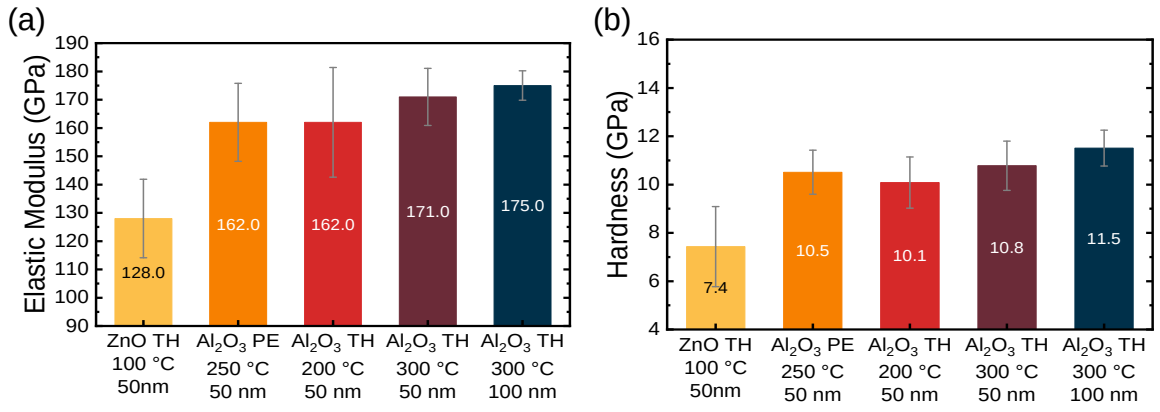

Fig. 3.S8. The (a) elastic modulus, and (b) hardness of different coating films as a function of deposition parameters.

3.6.2.3 Residual Stress Calculation

As detailed in the main text experimental section 3.2, a series of images were recorded during the FIB milling process. A Matlab-based DIC routine was employed to automatically evaluate the average strain change at each milling step relative to the initial image of the material surface before milling. The average strain measured by DIC is typically calculated

within a confined region, referred to as the effective area, rather than across the entire surface of the ring-core micro-pillar. This refinement is necessary because the periphery of the ring-core micro-pillar is often affected by artifacts from FIB milling or drilling, which can compromise the reliability of DIC measurements. In this study, the reduction factor was set to 80%. The evolution of strain relief with milling depth was extracted, and the master influence function was applied to invert the strain relief profile data to derive the eigenstrain depth profile [123]:

$$f\left(\frac{h}{D}\right) = \exp^{-\alpha\left(\frac{h}{D}\right)}\left[\alpha - \beta + \alpha\beta\left(\frac{h}{D}\right) + 2\gamma\left(\frac{h}{D}\right) - \alpha\gamma\left(\frac{h}{D}\right)^2\right]. \tag{3.7}$$

$$\epsilon^* = \frac{\epsilon}{\left(\frac{h}{D}\right) f\left(\frac{h}{D}\right)}. \tag{3.8}$$

where parameters α, β and γ are equal to 8.813, 6.647, and 53.852, respectively, for a reduction factor of 0.8. Here h represent the milling depth, D the inner diameter of the milled annular trench, ϵ^* the eigenstrain, and ϵ the strain obtained from the strain relief profile. Given the high sensitivity of the influence function and the potential measurement errors associated with the milling depth in such an ultra-thin range, the strain value at 80% of the film thickness was selected to calculate the residual stress in the film. The underlying residual stress within was then determined using the Hooke's law:

$$\sigma = E_f \epsilon^* / (1 - \nu). \tag{3.9}$$

3.6.3 Pillar splitting

The load-displacement curves of the pillar splitting tests are shown in Figure 3.S9 and Figure 3.S10.

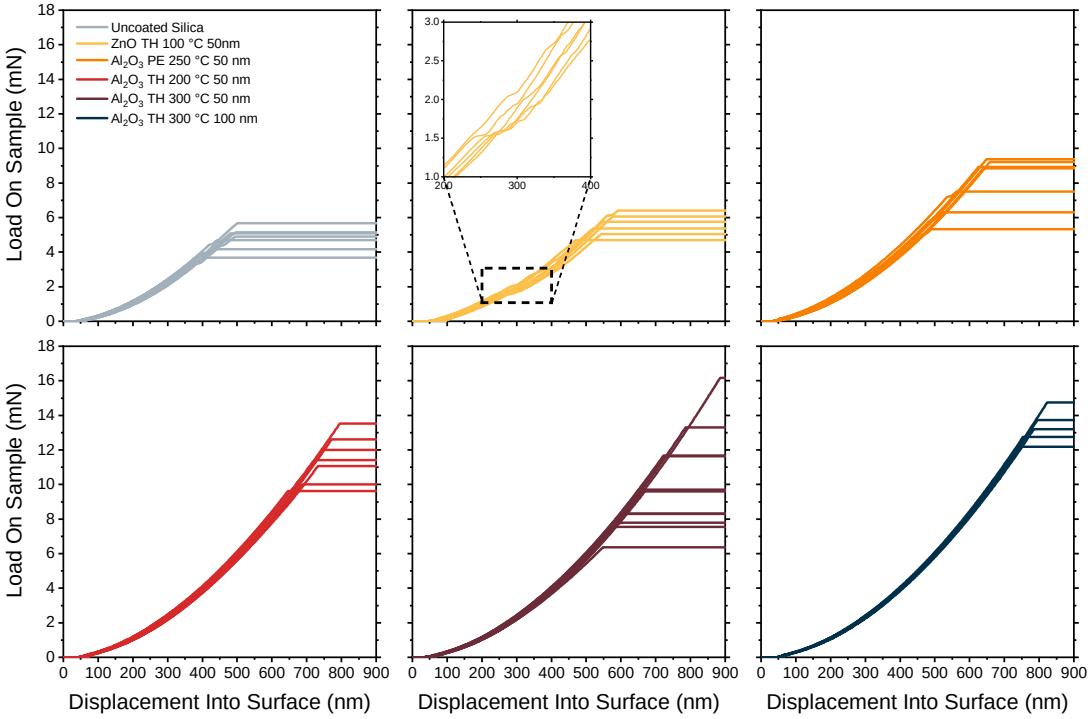

Fig. 3.S9. Representative load-displacement curves obtained on the ALD coated fused quartz samples.

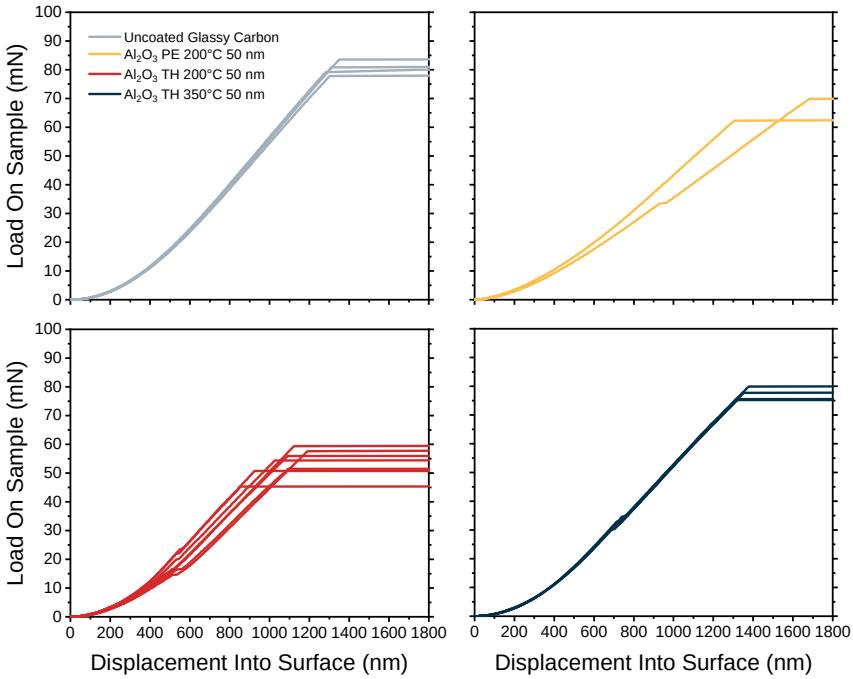

Fig. 3.S10. Representative load-displacement curves obtained on the ALD coated glassy carbon samples during the pillar splitting tests.

CHAPTER 4

Deformation behavior of optical ceramic nanomultilayers: the role of aperiodicity

4.1 | Introduction

Nanomultilayers (NMs) are thin-film coating architectures composed of alternating layers with individual thicknesses on the nanometer scale. The high density of interfaces intrinsic to these systems provides an expanded design space for tailoring functional properties beyond what is achievable in monolithic coatings. In particular, ceramic nanomultilayers composed of materials such as AlN, Al_2O_3, SiO_2, Ta_2O_5, TiO_2, and ZrO_2 have attracted significant interest due to their broadband optical transparency across the ultraviolet, visible, and near-infrared (UV–Vis–NIR) spectrum, combined with excellent chemical inertness, thermal stability, and high hardness [179, 180]. These attributes have enabled widespread application of ceramic NMs as optical windows, mirrors, antireflection coatings, and protective layers in harsh environments [181–183].

Beyond optical functionality, the mechanical performance of ceramic NMs is increasingly recognized as a critical factor governing coating reliability and lifetime. Prior studies largely motivated by tribological applications have demonstrated that hardness, elastic modulus, and wear resistance can be enhanced by tuning bilayer thickness, interface density, and layer morphology [184–187]. In selected systems, epitaxial growth at critical bilayer thicknesses has resulted in superlattice nanomultilayers with hardness values exceeding those of the constituent

materials [188–190]. Independently, optical performance has been shown to be highly sensitive to layer thickness distributions, where aperiodic architectures enable optimized broadband transmittance and reduced reflection losses [115, 191–195].

Despite these advances, the relationship between optical optimization strategies, especially the aperiodic layer stacking, and mechanical deformation or fracture remains poorly understood. In service, degradation of optical coatings is often initiated by mechanically driven damage arising from thermal cycling, irradiation, abrasion, or particle impact, which can trigger crack initiation, interfacial delamination, or stress-assisted oxidation, ultimately leading to optical scattering or loss [196, 197]. Consequently, the design of ceramic NMs for optical applications cannot rely solely on spectral performance; fracture resistance and deformation mechanisms must be considered concurrently to ensure functional durability.

Motivated by this gap, this chapter focuses on the mechanical response of optically relevant ceramic nanomultilayers synthesized by physical vapor deposition. Three material systems, AlN/Al_2O_3, YSZ/Al_2O_3 (YSZ is 8 mol% yttria-stabilized zirconia), and AlN/YSZ, were selected to represent crystalline/amorphous (C/A) and crystalline/crystalline (C/C) interface combinations while maintaining similar overall constituent volume fractions. Within each system, both optically optimized aperiodic architectures and non-optimized configurations were investigated. For the optically optimized coatings, a minimum average transmittance of 90% across the UV–Vis–NIR spectrum was achieved, whereas the non-optimized multilayers serve as mechanically relevant comparators with distinct layer thickness distributions.

The scope of this chapter is intentionally focused on mechanical performance rather than optical design methodology, which is discussed deeply in the publication [76]. Elastic modulus and hardness were measured by nanoindentation, while fracture resistance and deformation mechanisms were evaluated through a combination of micropillar splitting, Vickers indentation, and postmortem scanning and transmission electron microscopy. By comparing multilayers with similar compositions but different stacking sequences and interface types, this work aims to elucidate how aperiodicity, local volume fraction variations, and crystallinity contrast influence crack initiation, propagation, and overall fracture toughness.

Through this approach, the chapter establishes mechanistic links between nanomultilayer architecture and mechanical reliability, providing insights that complement optical optimization

strategies. These results highlight how surface and interface engineering via multilayer design can be leveraged to achieve optomechanically robust ceramic coatings, thereby enabling informed materials selection and architectural tuning for advanced optical applications.

4.2 | Materials and methods

4.2.1 Coating synthesis

AlN/Al_2O_3, AlN/YSZ, and YSZ/Al_2O_3 NMs and single-layered AlN, Al_2O_3, and YSZ coatings were synthesized via magnetron sputtering on Corning Eagle 2000 boro-aluminosilicate substrates (Delta Technologies, Colorado), $25\,\mathrm{mm}$ in diameter and $0.5\,\mathrm{mm}$ in thickness. All single layer and NM coatings were deposited with targeted overall thicknesses of $1\,\mu\mathrm{m}$. Figure 4.1 provides a visual representation of the aperiodic distribution of layers for the NMs. Following the sputtering direction, which begins at the bottom of each schematic and moves upwards through the layers, local variations of volume fraction can be observed based on groupings of layers, herein referred to as layer stacks. For instance, in AlN/Al_2O_3 MBI 78, the stack of layers 1–16 are modeled with a locally high Al_2O_3 volume fraction stack of 0.94; this is topped by a stack (layers 17–20) in which the AlN volume fraction is 0.73. The layer stacking for YSZ/Al_2O_3 78 and AlN/YSZ 78 is similarly distributed. In contrast, YSZ/Al_2O_3 MBI 74 and AlN/YSZ MBI 82 are modeled with five and three distinct layer stacks, respectively.

Firstly, substrates were cleaned with a 1:1 isopropanol and acetone mixture. Before deposition, the sputtering chamber was evacuated to a base pressure less than $1.0 \times 10^{-4}\,\mathrm{Pa}$. AlN layers were deposited via reactive DC sputtering with a $33\,\mathrm{mm}$ $(1.3\,\mathrm{in})$, 99.99% Al target (Plasmaterials, California). Power was set to $150\,\mathrm{W}$, and the argon (Ar) and nitrogen (N_2) gas flow rates were 37.5 and $12.5\,\mathrm{sccm}$, respectively, resulting in a working pressure of $1.2\,\mathrm{Pa}$. Al_2O_3 layers were deposited via radio frequency sputtering with $33\,\mathrm{mm}$ $(1.3\,\mathrm{in})$, 99.99% Al_2O_3 target. Power settings were fixed at $40\,\mathrm{W}$ with a tune of 38% and load of 76%. Inert Ar pressure was set at $0.67\,\mathrm{Pa}$. The synthesis parameters for AlN and Al_2O_3 follow sputtering conditions in previous works [115, 198]. YSZ layers were deposited with a 99.7% $(ZrO_2)92(Y_2O_3)08$ mol% target, using the same power and gas settings as Al_2O_3. All oxide layers were deposited with the same stoichiometry as the target. All targets were manufactured

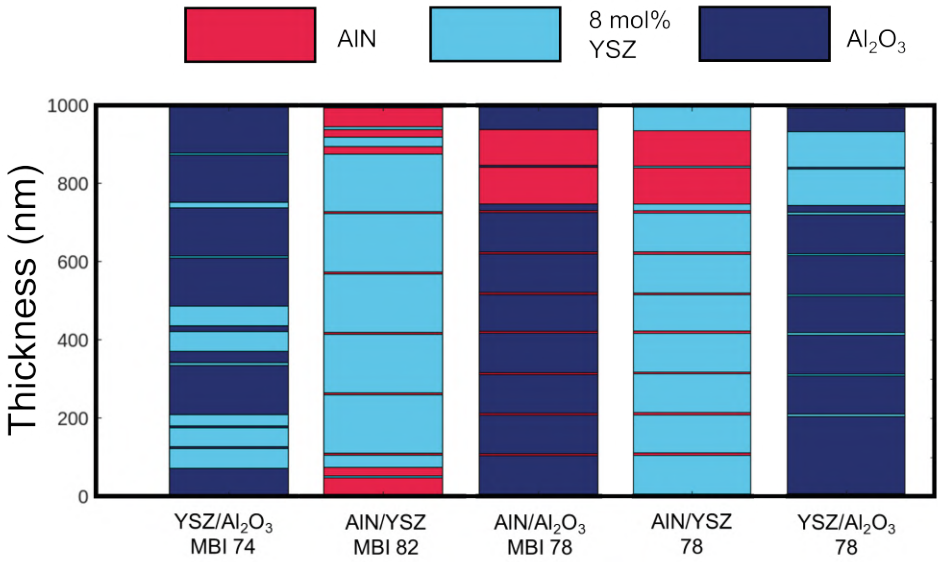

Fig. 4.1. Schematic of layer stacking for the aperiodic ceramic NMs. The numerical portion of the multilayer sample name indicates the modeled % volume fraction of the second layer constituent, whereas "MBI" refers to a layer configuration that was designed to yield a minimum UV-Vis-NIR transmittance of 90%.

by Plasmaterials (California). Regarding the sputtering configuration for NM coatings, the chamber was equipped with two sources, and power was alternately routed to one of two targets, with $5\,\mathrm{min}$ allotted between the deposition of each layer for vapor evacuation.

4.2.2 Microstructure characterization

To prepare as-sputtered NM cross-sections, a Helios 5CX Dual Beam Microscope (Thermo Fischer Scientific, Massachusetts) was used. The procedure for lamellae extraction and STEM imaging followed a standard lift-out and thinning approach to achieve a final lamella thickness of less than $80\,\mathrm{nm}$. Initially, the region of interest was coated with a protective layer to preserve near-surface features. A $200\,\mathrm{nm}$ thick platinum (Pt) layer was deposited using electron beam deposition at $5\,\mathrm{kV}$ and $1.4\,\mathrm{nA}$. Subsequently, a $2\,\mu\mathrm{m}$ thick tungsten (W) layer was deposited using ion beam deposition at $30\,\mathrm{kV}$ and $0.79\,\mathrm{nA}$. Trenches were milled using the ion beam at $30\,\mathrm{kV}$ and $0.79\,\mathrm{nA}$ to define the lamella dimensions of around $15 \times 5\,\mu\mathrm{m}$ (depth) with an initial thickness of $1.5\,\mu\mathrm{m}$ for extraction. The lamella was then lifted out and attached to a copper grid for subsequent thinning in three sequential steps to achieve electron transparency: 1) coarse thinning was conducted at $30\,\mathrm{kV}$ and $0.23\,\mathrm{nA}$, 2) fine polishing was carried out at $30\,\mathrm{kV}$ and $80\,\mathrm{pA}$, and 3) low-energy polishing at $5\,\mathrm{kV}$ and $15\,\mathrm{pA}$ was applied to minimize

surface damage and achieve a final thickness of less than $80\,\mathrm{nm}$. The analysis of the lamellae was performed in STEM mode (STEM 3+ detector) using an acceleration volt of $30\,\mathrm{kV}$ and a current of $0.34\,\mathrm{nA}$, in both brightfield and darkfield, with a dwell time of $30\,\mu\mathrm{s}$ and a line integration of 2.

4.2.3 Nanoindentation

For the single-layered coatings, load-controlled nanoindentation was performed in a 10 × 10 array with a Hysitron 950 Triboindenter (Bruker Corporation, Massachusetts) and a Berkovich diamond probe at a constant loading rate of $1000\,\mu\mathrm{N\,s^{-1}}$ to obtain reduced modulus and hardness, where reduced modulus was converted to elastic modulus [199]. For NMs, continuous stiffness measurement (CSM) nanoindentation was performed using a Berkovich probe at a constant strain rate of $0.05\,\mathrm{s^{-1}}$ to measure hardness H and elastic modulus E via an iNano nanoindenter (KLA, California) [78]. The 6 × 6 indent array with a maximum load of $50\,\mathrm{mN}$ was applied to each sample. Machine compliance and the tip area function were calibrated on a fused quartz reference sample before and after each test, following the procedure outlined by Oliver and Pharr [78]. Nix's model and Korsunsky's model were used to correct the influence of the substrate on the elastic modulus and hardness, respectively, using an averaged Poisson's ratio of 0.27 for the NM samples [87, 88, 90]. The properties of the substrate have been independently measured via the CSM technique, showing the elastic modulus as $67.01\,\mathrm{GPa}$ and hardness as $7.79\,\mathrm{GPa}$, which was used for the deconvolution of the measured data. For both nanoindentation configurations, the elastic modulus and Poisson's ratio of the indenter are 0.07 and $1140\,\mathrm{GPa}$, respectively. The more details about the deconvulution can be checked in Chapter 1.3.1.3.

4.2.4 Micropillar splitting

Arrays of at least fifteen micropillars (nominal top diameter of $1\,\mu\mathrm{m}$) were prepared for each sample by focused ion beam (FIB) milling with the Helios 5CX Dual Beam Microscope, as shown in Figure 4.2. A previously developed preparation procedure was used to minimize FIB-induced damage on the edge of pillars: five coarse milling steps have been employed using an ion current of $0.28\,\mathrm{nA}$ followed by a final refinement and shaping process involving a

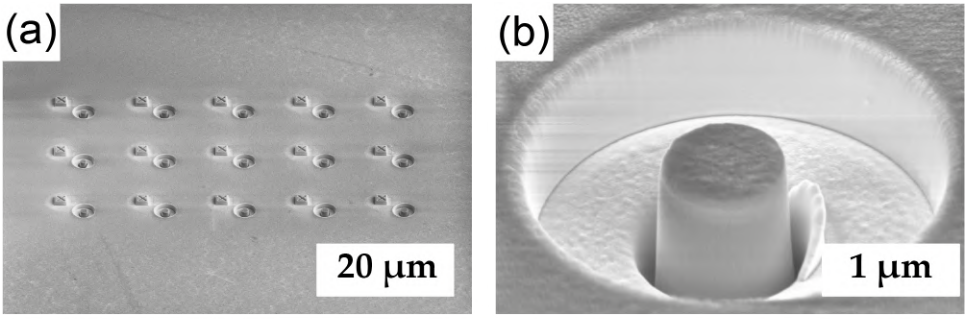

Fig. 4.2. FIB milled micropillars of AlN/YSZ 78 NMs: (a) overall view of the micropillars array, (b) the micropillar with diameter nearly $1\,\mu\mathrm{m}$.

current of $7.7\,\mathrm{pA}$ [108]. The distance between each pillar is set to $10\,\mu\mathrm{m}$. The aspect ratio (height-to-diameter) of the pillars was ensured to be greater than one, guaranteeing complete relaxation of the residual stress, if present, within the probing volume. Sharp indentation using a diamond tip with a cube-corner geometry on the center of each pillar was performed at a constant loading rate of around $0.033\,\mu\mathrm{N\,s^{-1}}$ until unstable propagation of a crack is achieved, thereby attaining the critical splitting load P_c, which appears as a burst in the load-displacement curve. The accurate positioning of the indenter at each pillar center was achieved in situ using a KLA nanoFLIP system equipped inside a FEI Helios NanoLab 600 Microscope. E-beam was used during positioning and switched off during testing to avoid possible beam damage [138]. From the attained crack propagation and failure, fracture toughness was computed through Equation 1.27. The radius r of each pillar was measured from the SEM image such as Figure 4.2b to provide a precise evaluation. Since γ coefficients were calculated assuming average film E/H ratios, the use of Equation 1.27 results in the estimation of "apparent" fracture toughness for the multilayer systems. Based on postmortem fracture morphology, only those pillars that were well centered (within the 10 % threshold of the pillar-measured radius as described by Lauener et al. [108] and split into three parts were selected to calculate the apparent fracture toughness of the coatings.

4.2.5 Vickers indentation and deformed cross-section preparation

A minimum of five Vickers indents per sample were carried out using a LM-100 Microindentation Hardness Tester (Leco, Michigan) at a $0.245\,\mathrm{N}$ $(25\,\mathrm{gf})$ load. Samples for cross-sectional STEM were prepared using Helios G4 UXe PFIB Dual Beam system, following the procedure

outlined in the "Optical Design and as-Sputtered Characterization" Section. A Cressington 108 Manual Sputter Coater (Ted Pella, Inc., California) was used for Pt-Pd protective coating. The lamellae were extracted using the Helios 5 Ga FIB UX DualBeam FIB, and TEM imaging was carried out using the Talos F200C G2 STEM.

4.3 | Results and discussion

As illustrated in Figure 4.1, optically optimized nanomultilayers are denoted as YSZ/Al_2O_3 MBI 74, AlN/YSZ MBI 82, and AlN/Al_2O_3 MBI 78, where "MBI" identifies an optically optimized multilayer configuration. The numerical suffix corresponds to the modeled volume fraction of the second constituent in the multilayer stack. For example, YSZ/Al_2O_3 MBI 74 is designed to exhibit an overall Al_2O_3 volume fraction of 0.74.

In addition to these optically optimized coatings, non-optimized nanomultilayers were fabricated within the AlN/YSZ and YSZ/Al_2O_3 material systems. These non-optimized samples were designed with layer thickness distributions similar to that of the AlN/Al_2O_3 MBI 78 configuration, enabling a direct comparison of optical transmittance and mechanical deformation behavior as a function of multilayer architecture rather than constituent chemistry alone.

4.3.1 The multilayer microstructure of optical ceramic

Figure 4.3 shows the X-ray diffraction data for single-layered coatings of AlN, Al_2O_3, and 8 mol% YSZ. For the AlN film, a hexagonal (1 0 1 1) texture is visible, whereas the YSZ coating exhibits the cubic phase, with no preferential orientation of the (1 1 1), (2 0 0), (2 2 0), or (3 1 1) planes, and Al_2O_3 is X-ray amorphous. Additionally, all patterns exhibit a diffuse peak in the 20°–30° 2θ range due to scattering from the glass substrate. The observed X-ray patterns are supported by microstructural characterization in prior studies and representative of the individual layers within the NMs of the current study [198, 200, 201]. Henceforth, AlN/Al_2O_3 and YSZ/Al_2O_3 NMs will be noted as having C/A layers, and AlN/YSZ, C/C layers.

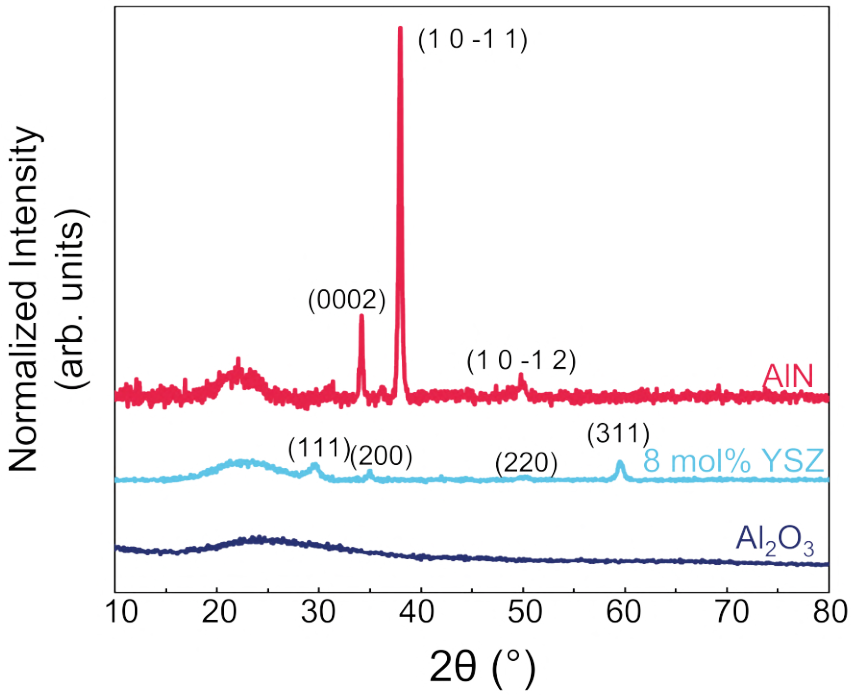

Fig. 4.3. X-ray diffraction plots of AlN, 8 mol % YSZ, and Al_2O_3 single layered coatings.

Figure 4.4 shows representative cross-sectional scanning TEM (STEM) images for the YSZ/Al_2O_3, AlN/YSZ, and AlN/Al_2O_3 NMs that were deposited under the same conditions as the single-layered coatings. While the as-sputtered NM layer thicknesses deviate slightly from the coating designs (Figure 4.1), the aperiodic layer distribution within each coating is preserved. Additionally, the cross-sectional images demonstrate sharp layer termination, although the C/C AlN/YSZ NMs exhibit more layer roughness than the C/A systems. Similar observations of interface roughness have been reported in various C/C NM systems and attributed to deposition conditions [202, 203]. It also was observed that a higher degree of interface/surface roughness can lower optical functionality, and therefore, the transmittance of the C/C NMs may be affected, which is most important for optically optimized samples [191, 192]. However, since the indices of refraction for the individual layers of AlN, Al_2O_3, and YSZ are 2.18, 1.77, and 1.63, respectively, optical optimization can be achieved by alternating layers of high- and low-indices of refraction or by having low refractive indices for both layers.

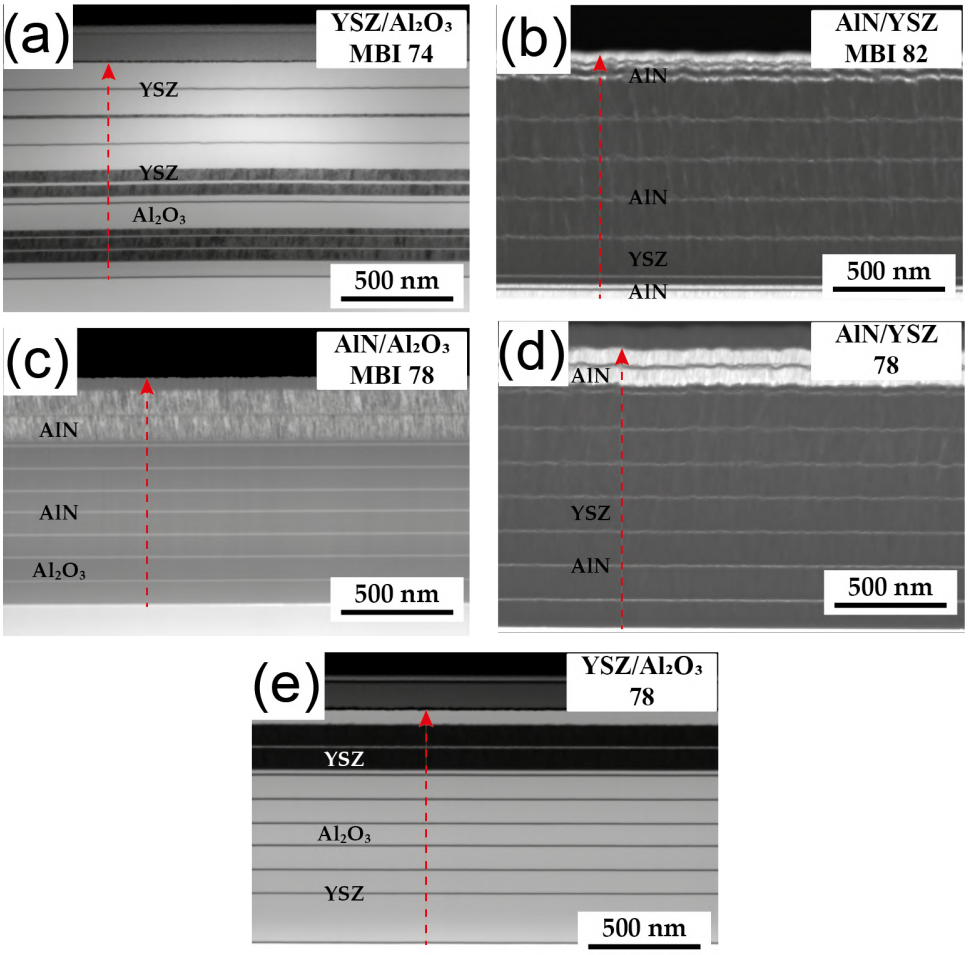

Fig. 4.4. As-sputtered cross-section of (a) YSZ/Al_2O_3 MBI 74, (b) AlN/YSZ MBI 82, (c) AlN/Al_2O_3 MBI 78, (d) AlN/YSZ 78, and (e) YSZ/Al_2O_3 78 NMs.

4.3.2 Mechanical behavior: deformation and properties

Table 4.1 sum up the testing results for both single-layered and NM coatings, with the columns showing the residual stress, elastic modulus, hardness, and fracture toughness for both single-layered and NM coatings. Here, the single-layered samples are used as baselines for comparison to the rule of mixtures (RoM) [204].

4.3.2.1 E&H comparison

Nanoindentation was performed to assess the elastic modulus and hardness of the single-layer and NM coatings. For the NMs, the elastic modulus ranges from 142.5 to 174.8 GPa, with all values being statistically significant (two-sided, two-sample t-test, $P = 0.001$) [209]. Figure 4.5 summarizes the elastic modulus and hardness of the different multilayer configurations, complementing the values listed in Table 4.1.

Table 4.1
Residual stress, elastic modulus, hardness, and fracture toughness of ceramic single layers (from literature) and aperiodic NMs (experimental).

Sample	Residual stress (MPa)	E (GPa)	H (GPa)	K_c (MPa$\sqrt{\text{m}}$)
AlN	−17.2	148.8 ± 4.6	9.1 ± 0.7	1.5–1.8 [205]
Al_2O_3	89.6	109.4 ± 3.7	6.4 ± 0.5	2.5–3.8 [205, 206]
YSZ	−2.5	172.4 ± 19.0	11.1 ± 2.4	≈ 1.2–1.7 [207, 208]
YSZ/Al_2O_3 MBI 74	−787.6	152.2 ± 3.4	12.9 ± 1.3	3.4 ± 0.5
AlN/YSZ MBI 82	2.2	142.5 ± 8.1	10.9 ± 0.7	1.6 ± 0.3
AlN/Al_2O_3 MBI 78	−38.3	161.2 ± 3.7	13.8 ± 0.5	2.9 ± 0.2
AlN/YSZ 78	−139.6	174.8 ± 6.9	16.0 ± 1.8	1.7 ± 0.2
YSZ/Al_2O_3 78	−612.7	166.9 ± 3.6	15.6 ± 0.8	3.5 ± 0.2

The elastic modulus and hardness values were extracted from CSM nanoindentation using the Doerner–Nix substrate correction model [86, 88] to minimize substrate influence. Details of the deconvolution procedure are provided in Chapter 1.3.1.3. The resulting values therefore represent the apparent mechanical response of the nanomultilayer coating systems, rather than intrinsic properties of individual constituent layers. Among all configurations, AlN/YSZ 78 and AlN/YSZ MBI 82 exhibit the highest and lowest elastic moduli, respectively. Compared with the single-layer coatings, the elastic moduli of YSZ/Al_2O_3 MBI 74, AlN/YSZ MBI 82, AlN/YSZ 78, and YSZ/Al_2O_3 78 fall within the bounds predicted by the rule of mixtures (RoM) [204].

The hardness of the nanomultilayers varies from 10.9 to 16.0 GPa, with all differences being statistically significant except between AlN/YSZ 78 and YSZ/Al_2O_3 78 [209]. Notably, YSZ/Al_2O_3 MBI 74 and YSZ/Al_2O_3 78 possess similar constituent volume fractions but exhibit markedly different hardness values (12.9 GPa vs. 15.6 GPa). A similar trend is observed for AlN/YSZ MBI 82 and AlN/YSZ 78 (10.9 GPa vs. 16.0 GPa), indicating that hardness is strongly influenced by multilayer architecture rather than composition alone.

The depth-dependent elastic modulus and hardness profiles are shown in Figure 4.6, providing further insight into the influence of stacking configuration. As the indentation depth increases toward the total coating thickness, both elastic modulus and hardness progressively approach the substrate response. The hardness exhibits a slight increase at shallow depths for most configurations, whereas the elastic modulus decreases monotonically with depth.

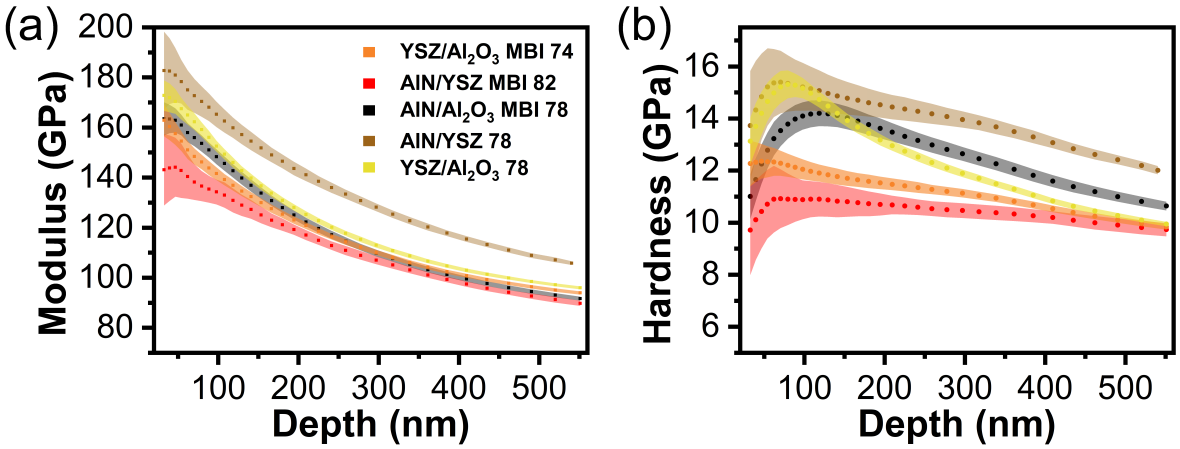

Fig. 4.6. The (a) elastic modulus, and (b) hardness obtained from the aperiodic NMs coated samples as a function of indentation depth(experimental).

AlN/Al_2O_3 MBI 78, AlN/YSZ 78, and YSZ/Al_2O_3 78 consistently show higher hardness than the other configurations. These coatings share a smaller repeating period in the mechanically dominant region, resulting in a higher effective interface density within the indentation-induced plastic zone. The increased frequency of interfaces provides more effective barriers to plastic deformation, thereby enhancing hardness, particularly for AlN/YSZ 78, which incorporates hard YSZ layers. In contrast, AlN/YSZ MBI 82 consists of relatively thick YSZ blocks separated by ultrathin AlN layers, together with thicker AlN segments near the top and bottom of the coating. As the plastic zone develops under indentation, the reduced interface density within the plastically deformed volume facilitates localized plastic flow, leading to a lower measured hardness.

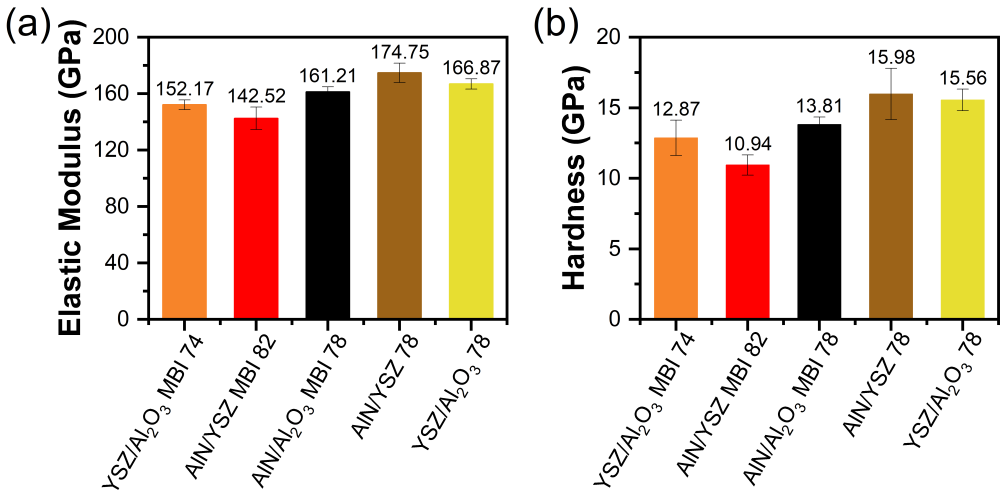

Fig. 4.5. The measured (a) elastic modulus, and (b) hardness of the aperiodic NMs (experimental).

As discussed in Section 1.3.1, hardness obtained from sharp nanoindentation is a plastic-zone-dominated parameter, governed primarily by the materials and interfaces within the plastically deformed volume at a given indentation depth. By contrast, the elastic modulus extracted from CSM reflects the elastic response of a much larger material volume, as elastic strain energy is stored well beyond the plastic zone. Consequently, the measured modulus represents a weighted average of the elastic properties of the entire multilayer stack and, at larger depths, increasingly incorporates substrate contributions.

Therefore, further tunability of mechanical behavior in aperiodic ceramic nanomultilayers may be achieved by systematically tailoring stacking architecture and by examining the contributions of individual layers using complementary mechanical characterization techniques, thereby strengthening the correlation between coating design parameters and deformation mechanisms.

4.3.2.2 Fracture mechanism

The evaluation of fracture toughness was performed on the YSZ/Al_2O_3, AlN/YSZ, and AlN/Al_2O_3 NMs via micropillar splitting, using the nanoindentation-derived elastic modulus and hardness for calculations based on Equation 1.27 [105]. It should be noted that the single-layered fracture toughness (K_c) values were derived from various and/or unspecified loading modes, whereas the nanomultilayered fracture toughness values are correlated to mode I loading (opening, K_{Ic}). The fracture toughness values are shown in the last column of Table 4.1 and further discussed in Figure 4.7, where the load-displacement curves for each NM are shown with representative SEM image insets of postmortem pillars. It is observed that YSZ/Al_2O_3 78 exhibits the highest apparent fracture toughness of $3.5\,\mathrm{MPa}\sqrt{\mathrm{m}}$ followed by $3.4\,\mathrm{MPa}\sqrt{\mathrm{m}}$ for YSZ/Al_2O_3 MBI 74 and $2.9\,\mathrm{MPa}\sqrt{\mathrm{m}}$ for AlN/Al_2O_3 MBI 78. AlN/YSZ 78 and AlN/YSZ MBI 82 exhibit relatively lower fracture toughness values of 1.7 and $1.6\,\mathrm{MPa}\sqrt{\mathrm{m}}$, respectively (Table 4.1). These values also are depicted in a bar graph in Figure 4.7f. Since the fracture toughness for ceramic materials typically spans from 1 to $3\,\mathrm{MPa}\sqrt{\mathrm{m}}$, the attained values for all NMs are expected, and separately, are intermediate to those of their constituents, with the YSZ/Al_2O_3 NMs presenting the highest values [204]. Specifically for the NMs, apparent fracture toughness was derived from an equation based on the critical splitting load,

pillar radius, and γ, a coefficient influenced by the E/H ratio, Poisson's ratio, and the indenter angle (see Equation 1.27 in Chapter 1.3.2). It was previously reported for ceramic NMs that, when comparing the weight of various factors, the critical splitting load is a direct parameter to evaluate fracture toughness. Hence, the fracture behavior of the aperiodic ceramic NMs is further analyzed through their load-displacement curves, where the critical pillar splitting load is defined as the load at which unstable crack growth occurs, characterized by a displacement burst and discontinuity at relatively shallow depths [139]. In all, YSZ/Al_2O_3 MBI 74 and YSZ/Al_2O_3 78 exhibit the highest critical splitting loads, averaging 2.0 and $1.9\,\mu N$, respectively. These are followed by AlN/Al_2O_3 MBI 78 ($1.7\,\mu N$), AlN/YSZ 78 ($1.2\,\mu N$), and AlN/YSZ MBI 82 ($0.8\,\mu N$). A displacement burst for AlN/ YSZ MBI 82 (Figure 4.7b), AlN/Al_2O_3 MBI 78 (Figure 4.7c), and AlN/YSZ 78 (Figure 4.7d) occurs $200\,nm$ into the coating and at a depth of $300\,nm$ for YSZ/Al_2O_3 78 (Figure 4.7e). Interestingly, although similar critical loads were observed in the YSZ/Al_2O_3 NMs, an inflection point rather than a displacement burst is noted for YSZ/Al_2O_3 MBI 74 (Figure 4.7a), which is an uncharacteristic behavior for pillar splitting and can be indicative of stable crack growth.

The post fracture SEM image insets of Figure 4.7 indicate that the C/C AlN/YSZ NMs failed by intergranular fracture (Figure 4.7b,d), where the step-like features on the fracture surfaces for AlN/YSZ 78 suggest crack deflection at the interfaces, a behavior known as a toughening mechanism for NMs [210]. For C/A AlN/Al_2O_3 MBI 78, the intergranular fracture mode is confined to the layer stack with a locally high AlN volume fraction (Figure 4.7c). However, the fracture surfaces for the C/A YSZ/Al_2O_3 NMs are relatively featureless (Figure 4.7a,e). Overall, when comparing measured values and post-mortem images of the C/C and C/A NMs, the latter seems more suitable for mechanical functionality, although the opportunity for improvement remains.

Specifically, previous studies on C/A NMs and nanolaminates reported that failure modes can be controlled through the amorphous layer thickness [211–213]. Thus, the C/A NMs in this work were selected for additional testing, through which the link of aperiodicity to deformation could be further developed.

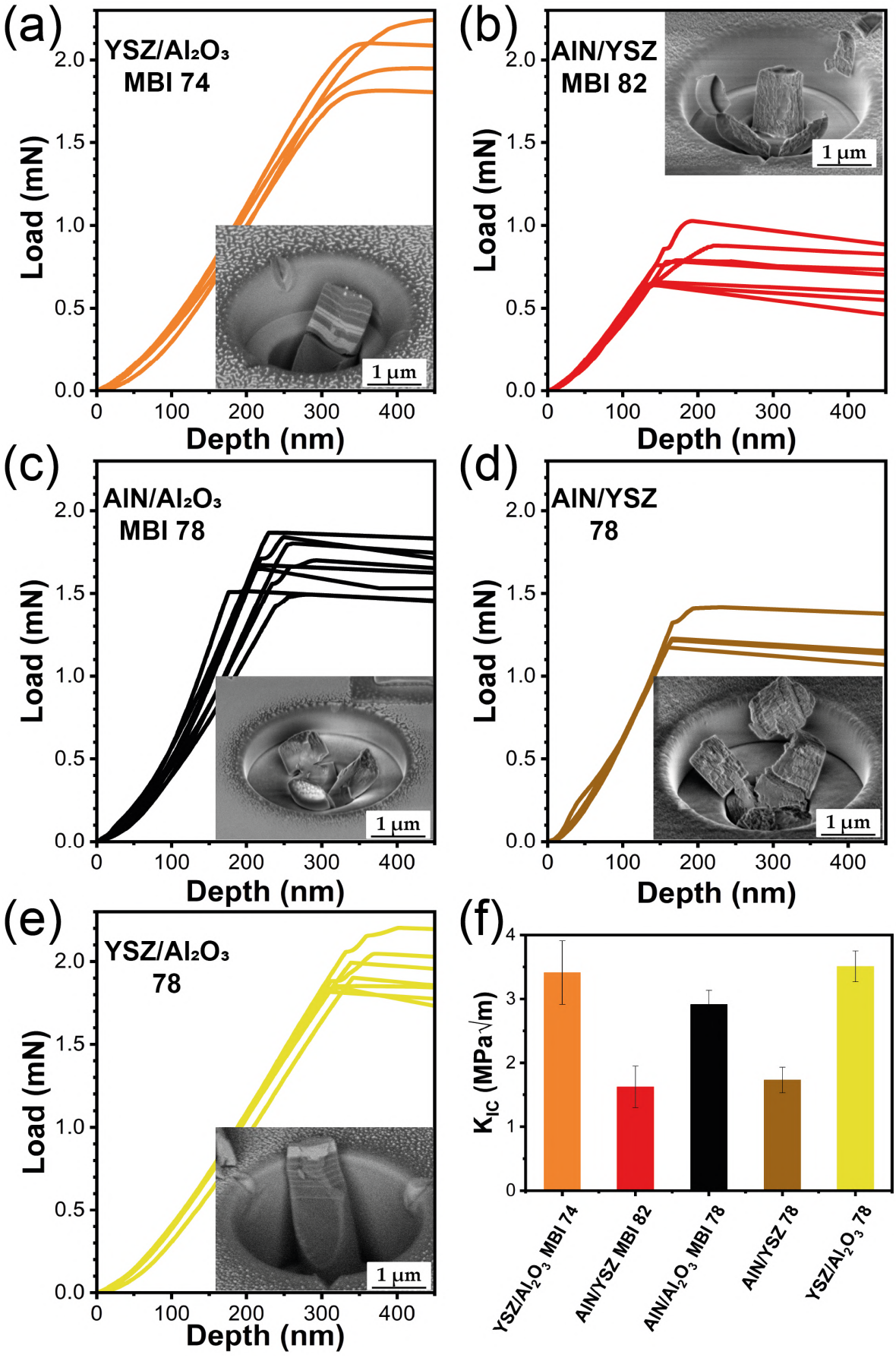

Fig. 4.7. Pillar splitting. Representative load-displacement curves obtained for aperiodic (a) YSZ/Al_2O_3 MBI 74, (b) AlN/YSZ MBI 82, (c) AlN/Al_2O_3 MBI 78, (d) AlN/YSZ 78, and (e) YSZ/Al_2O_3 78 NMs during pillar splitting tests with corresponding postfracture SEM micrographs as insets. (f) Bar graph of average apparent fracture toughness for all NMs.

To explore the qualitative effects of aperiodic configurations, Vickers microindentation was performed at a $0.245\,\mathrm{N}$ $(25\,\mathrm{gf})$ load, as shown in Figure 4.8 for the three C/A NMs, which includes representative top-surface SEM indent images (Figure 4.8a), cross-sectional high-angle annular dark-field (HADDF-STEM) micro-graphs (Figure 4.8b), and magnified views of the cross-sections (Figure 4.8c).

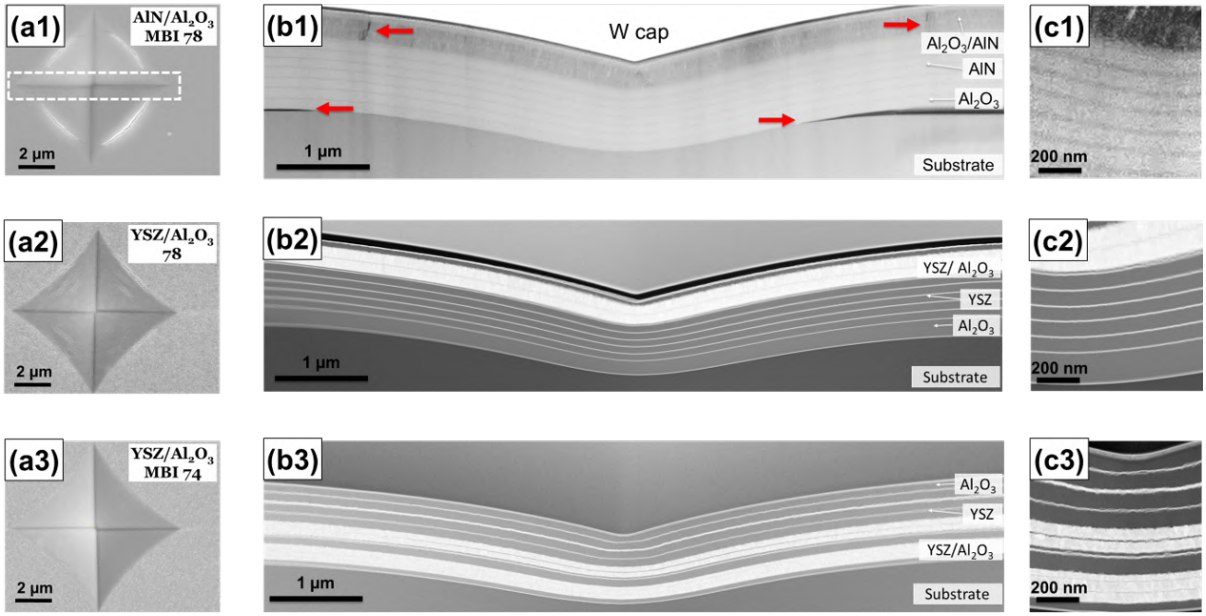

Fig. 4.8. Vickers indentation and cross-sectional analysis. Representative micrographs post Vickers indentation at $25\,\mathrm{gf}$ for aperiodic ceramic NMs. Planview SEM of (a1) AlN/Al_2O_3 MBI 78, a2) YSZ/Al_2O_3 78, and a3) YSZ/Al_2O_3 MBI 74 indents. b1–b3) Corresponding cross-sectional HAADF-STEM micrographs along the indent diagonal, as marked by the dashed box in (a1). Red arrows in (b1) indicate areas of deformation or delamination. (c1–c3) Magnified views of corresponding samples.

From the SEM images in Figure 4.8 a, fracture features are observed for AlN/Al_2O_3 MBI 78 (Figure 4.8 a1) and YSZ/Al_2O_3 78 (Figure 4.8a2), with cracks formed around the indent edge. In contrast, no distinct fracture features are noted for YSZ/Al_2O_3 MBI 74, which is the only NM with a locally high amorphous volume fraction stack near the surface of the coating (see Figure 4.1). This is consistent with the unique yielding of YSZ/Al_2O_3 MBI 74 observed during the pillar splitting tests. To connect top-surface indentation observations with layer-specific deformation and local volume fractions, electron-transparent cross-sections were prepared under the horizontal indent diagonals for the C/A NMs (as outlined in Figure 4.8a1), with STEM micrographs of the cross-sections provided in Figure 4.8b,c. From these images, it is observed that the substrates and coatings bend in response to the applied load,

confirming flexure of the coating. For AlN/Al_2O_3 MBI 78, delamination, reoriented grains, and intergranular fracture are observed within a locally high AlN volume fraction stack (Figure 4.8b1). Whereas, YSZ/Al_2O_3 78 and YSZ/Al_2O_3 MBI 74 do not exhibit any fracture features within its layers (Figure 4.8b2,b3). These observations are consistent with a previous study on TiAlN coatings which suggested that larger compressive stresses (see Table 4.1) allow for greater compensation of strain [214]. Furthermore, independent of magnitude and compressive stresses are known to retard crack propagation and counter the effects from tensile loads [183].

4.4 | Conclusion

In this work, aperiodic ceramic NMs were studied to explore the role of various layer arrangements on optical transmittance and mechanical behavior. NMs with similar and distinct layer stacks across the AlN/Al_2O_3, YSZ/Al_2O_3, and AlN/YSZ systems were synthesized to enable this investigation, with one configuration for each system designed for optical optimization. A minimum 90% transmittance across the UV-Vis-NIR wavelength spectrum was achieved for the optically optimized aperiodic NMs, highlighting opportunities to further increase transmittance and examine the mechanical behavior through the scope of aperiodicity. By performing mechanical tests at various length scales, the influences of aperiodic layer stacking, C/C and C/A interfaces, and localized volume fractions were evident when comparing properties, such as hardness and fracture toughness, within and across the systems. Samples with amorphous Al_2O_3 layers and C/A interfaces generally demonstrated the best mechanical performance, and specifically for the YSZ/Al_2O_3 MBI 74 NM coating, indications of stable crack propagation and strain accommodation without fracture were noted. Thus, the scope and span of the mechanical behavior presented in this study elucidate the correlation between aperiodicity and deformation in optical ceramic NMs, where variations in local volume fraction within aperiodic configurations can be tailored to control the fracture mode. This demonstrates that, although interface characteristics and layer composition influence deformation, aperiodicity can be implemented as a design factor for optomechanical multifunctionality.

CHAPTER 5

Summary and outlook

This thesis systematically investigates the mechanical behavior and fracture mechanisms of micro ceramic systems enabled by advanced additive manufacturing, ALD, and multilayer nano-architecture design. By combining quantitative experiments with mechanics-based modeling, the work establishes clear structure–property–mechanism relationships across multiple material platforms and length scales, demonstrating how processing routes, residual stress engineering, and coating configurations can be leveraged to tailor fracture resistance and mechanical reliability.

First, the intrinsic mechanical properties of sinterless silica fabricated via TPPDLW and subsequent pyrolysis were established and benchmarked against conventionally processed fused silica. Through complementary nanoindentation and micropillar splitting measurements, this work demonstrates that sinterless TPP-derived silica exhibits elastic modulus, hardness, and fracture toughness values that are indistinguishable from those of lithography- and FIB-fabricated silica. Crucially, the agreement across fabrication routes confirms that the glass network formed during low-temperature pyrolysis is mechanically equivalent to traditional fused silica, despite the absence of high-temperature sintering. The observed size-independent fracture toughness over the investigated micrometer-scale regime further indicates that the measured values reflect intrinsic material behavior rather than extrinsic geometric or testing artifacts. Together, these findings validate sinterless TPP-derived silica as a mechanically robust structural material, while simultaneously enabling unprecedented geometric freedom and compatibility with temperature-sensitive microsystems.

Building on this foundation, the second part of the thesis explores fracture toughness modulation through residual stress engineering using ALD coatings on micro-ceramic systems. By integrating high-resolution FIB–DIC measurements, pillar splitting experiments, and cohesive-

zone finite element modeling, this work reveals how ALD-induced residual stresses fundamentally alter crack initiation and propagation pathways. The results demonstrate that tensile residual stresses in the coating can significantly enhance apparent fracture toughness when median cracking dominates, due to the generation of compressive stresses in the substrate, whereas compressive residual stresses generally reduce crack resistance. Importantly, the fracture response is shown to be crack-geometry-dependent: both tensile and compressive stresses can induce embrittlement when Palmqvist cracking occurs. These findings clarify previously ambiguous experimental observations and highlight that the effectiveness of ALD-based stress engineering depends critically on the material system, coating thickness, deposition conditions, and crack morphology. The study thus establishes residual stress as a powerful design parameter for tuning fracture behavior in micro-ceramics.

Finally, the thesis extends the investigation of fracture and deformation mechanisms to optically functional aperiodic ceramic nanomaterials. By systematically varying layer arrangements and interface types across multiple material systems, this work demonstrates that aperiodicity introduces local variations in volume fraction and constraint that strongly influence mechanical response, which is governed by the interplay between amorphous versus crystalline layers, interface chemistry, and local structural heterogeneity. In particular, nanomaterials incorporating amorphous Al_2O_3 layers and ceramic/amorphous interfaces exhibit superior fracture resistance and, in some cases, evidence of stable crack propagation and strain accommodation. These observations reveal that aperiodicity is not merely a photonic design strategy, but also a viable mechanical design variable that can be exploited to control fracture mode and deformation behavior in multifunctional ceramic systems.

Collectively, this thesis establishes a unified framework for understanding and tailoring fracture behavior in architected ceramics by linking processing-induced structure, residual stress states, and architectural complexity to underlying fracture mechanisms. The results demonstrate that advanced manufacturing techniques—when combined with stress engineering and architectural design—can overcome the traditional brittleness of ceramics without compromising intrinsic material performance. Looking forward, extending these strategies to fully micro-architected metamaterials, where residual stress, interface design, and topology can be

co-optimized, represents a promising pathway toward mechanically reliable, optomechanically multifunctional systems for applications in microsystems, micro-optics, and nanophotonics.

References

[1] L. J. Gibson and M. F. Ashby, *Cellular Solids: Structure and Properties*, 2nd ed. Cambridge, UK: Cambridge University Press, 1997.

[2] N. A. Fleck, V. S. Deshpande, and M. F. Ashby, "Micro-architectured materials: Past, present and future," *Proceedings of the Royal Society A: Mathematical, Physical and Engineering Sciences*, vol. 466, pp. 2495–2516, 2010. DOI: https://doi.org/10.1098/rspa.2010.0215.

[3] L. R. Meza et al., "Reexamining the mechanical property space of three-dimensional lattice architectures," *Acta Materialia*, vol. 140, pp. 424–432, 2017. DOI: https://doi.org/10.1016/j.actamat.2017.08.052.

[4] Y. Bai et al., "Programmable mechanical metamaterials with tailorable negative poisson's ratio and arbitrary thermal expansion in multiple thermal deformation modes," *ACS Applied Materials & Interfaces*, vol. 14, no. 31, pp. 35 905–35 916, 2022, PMID: 35880735. DOI: 10.1021/acsami.2c08270.

[5] X. Xin, L. Liu, Y. Liu, and J. Leng, "4D printing auxetic metamaterials with tunable, programmable, and reconfigurable mechanical properties," *Advanced Functional Materials*, vol. 30, no. 43, p. 2 004 226, 2020. DOI: https://doi.org/10.1002/adfm.202004226.

[6] L. Wang et al., "3D auxetic metamaterials with elastically-stable continuous phase transition," *Advanced Science*, vol. 9, 34 Dec. 2022. DOI: 10.1002/advs.202204721.

[7] N. Ma, Q. Han, S. Han, and C. Li, "Hierarchical re-entrant honeycomb metamaterial for energy absorption and vibration insulation," *International Journal of Mechanical Sciences*, vol. 250, p. 108 307, 2023. DOI: https://doi.org/10.1016/j.ijmecsci.2023.108307.

[8] X. Zhang et al., "Novel hierarchical interpenetrating lattice metamaterials with superior energy absorption," *Engineering Structures*, vol. 345, p. 121 549, 2025. DOI: https://doi.org/10.1016/j.engstruct.2025.121549.

[9] W. Lin, Y. Yan, S. Zhao, H. Qin, and Y. Liu, "Digital mechanical metamaterial with programmable functionality," *Advanced Materials*, vol. 36, no. 47, p. 2 406 263, 2024. DOI: https://doi.org/10.1002/adma.202406263.

[10] B. Haghpanah, H. Ebrahimi, D. Mousanezhad, J. Hopkins, and A. Vaziri, "Programmable elastic metamaterials," *Advanced Engineering Materials*, vol. 18, no. 4, pp. 643–649, 2016. DOI: https://doi.org/10.1002/adem.201500295.

[11] S. O'Halloran, A. Pandit, A. Heise, and A. Kellett, "Two-photon polymerization: Fundamentals, materials, and chemical modification strategies," *Advanced Science*, vol. 10, no. 7, p. 2 204 072, 2023. DOI: https://doi.org/10.1002/advs.202204072.

[12] A. Selimis, V. Mironov, and M. Farsari, "Direct laser writing: Principles and materials for scaffold 3D printing," *Microelectronic Engineering*, vol. 132, pp. 83–89, 2015. DOI: https://doi.org/10.1016/j.mee.2014.10.001.

[13] C. M. Kurpiers, S. Hengsbach, and R. Schwaiger, "Architectural tunability of mechanical metamaterials in the nanometer range," *MRS Advances*, vol. 6, no. 20, pp. 507–512, 2021. DOI: 10.1557/s43580-021-00094-1.

[14] J. Bauer, A. Guell Izard, Y. Zhang, T. Baldacchini, and L. Valdevit, "Programmable mechanical properties of two-photon polymerized materials: From nanowires to bulk," *Advanced Materials Technologies*, vol. 4, no. 9, p. 1 900 146, 2019. DOI: https://doi.org/10.1002/admt.201900146.

[15] A. Schroer, J. Bauer, R. Schwaiger, and O. Kraft, "Optimizing the mechanical properties of polymer resists for strong and light-weight micro-truss structures," *Extreme Mechanics Letters*, vol. 8, pp. 283–291, 2016. DOI: https://doi.org/10.1016/j.eml.2016.04.014.

[16] L. R. Meza, S. Das, and J. R. Greer, "Strong, lightweight, and recoverable three-dimensional ceramic nanolattices," *Science*, vol. 345, pp. 1322–1326, 6202 2014. DOI: https://doi.org/10.1126/science.1255908.

[17] J. Bauer, A. Schroer, R. Schwaiger, and O. Kraft, "Approaching theoretical strength in glassy carbon nanolattices," *Nature Materials*, vol. 15, pp. 438–443, 4 Apr. 2016. DOI: 10.1038/nmat4561.

[18] C. Crook et al., "Plate-nanolattices at the theoretical limit of stiffness and strength," *Nature Communications*, vol. 11, 1 Dec. 2020. DOI: 10.1038/s41467-020-15434-2.

[19] M. Diamantopoulou, C. C. Roth, T. Tancogne-Dejean, C. M. Lauener, and D. Mohr, "Ceramic/polymer microlattices: Increasing specific energy absorption through sandwich construction," *Extreme Mechanics Letters*, vol. 53, p. 101 708, 2022. DOI: https://doi.org/10.1016/j.eml.2022.101708.

[20] A. Guell Izard, J. Bauer, C. Crook, V. Turlo, and L. Valdevit, "Ultrahigh energy absorption multifunctional spinodal nanoarchitectures," *Small*, vol. 15, no. 45, p. 1 903 834, 2019. DOI: https://doi.org/10.1002/smll.201903834.

[21] W. P. Moestopo, A. J. Mateos, R. M. Fuller, J. R. Greer, and C. M. Portela, "Pushing and pulling on ropes: Hierarchical woven materials," *Advanced Science*, vol. 7, 20 Oct. 2020. DOI: 10.1002/advs.202001271.

[22] J. Bauer, J. A. Kraus, C. Crook, J. J. Rimoli, and L. Valdevit, "Tensegrity metamaterials: Toward failure-resistant engineering systems through delocalized deformation," *Advanced Materials*, vol. 33, 10 Mar. 2021. DOI: 10.1002/adma.202005647.

[23] Z. C. Eckel, C. Zhou, J. H. Martin, A. J. Jacobsen, W. B. Carter, and T. A. Schaedler, "Additive manufacturing of polymer-derived ceramics," *Science*, vol. 351, no. 6268, pp. 58–62, 2016. DOI: 10.1126/science.aad2688.

[24] L. Brigo, J. E. M. Schmidt, A. Gandin, N. Michieli, P. Colombo, and G. Brusatin, "3D nanofabrication of SiOC ceramic structures," *Advanced Science*, vol. 5, no. 12, p. 1 800 937, 2018. DOI: https://doi.org/10.1002/advs.201800937.

[25] J. Im et al., "Strategies for integrating metal nanoparticles with two-photon polymerization process: Toward high resolution functional additive manufacturing," *Advanced Functional Materials*, 2023. DOI: 10.1002/adfm.202211920.

[26] D. W. Yee, M. L. Lifson, B. W. Edwards, and J. R. Greer, "Additive manufacturing of 3D-architected multifunctional metal oxides," *Advanced Materials*, vol. 31, 33 Aug. 2019. DOI: 10.1002/adma.201901345.

[27] Q. Li et al., "Mechanical nanolattices printed using nanocluster-based photoresists," *Science*, vol. 378, no. 6621, pp. 768–773, 2022. DOI: 10.1126/science.abo6997.

[28] J. Bauer, A. Schroer, R. Schwaiger, and O. Kraft, "The impact of size and loading direction on the strength of architected lattice materials," *Advanced Engineering Materials*, vol. 18, pp. 1537–1543, 9 2016. DOI: 10.1002/adem.201600235.

[29] J. Bauer, S. Hengsbach, I. Tesari, R. Schwaiger, and O. Kraft, "High-strength cellular ceramic composites with 3D microarchitecture," *Proceedings of the National Academy of Sciences*, vol. 111, no. 7, pp. 2453–2458, 2014. DOI: 10.1073/pnas.1315147111.

[30] M. Mieszala et al., "Micromechanics of amorphous metal/polymer hybrid structures with 3D cellular architectures: Size effects, buckling behavior, and energy absorption capability," *Small*, vol. 13, no. 8, p. 1 602 514, 2017. DOI: https://doi.org/10.1002/smll.201602514.

[31] M. Ashby, "The properties of foams and lattices," *Philosophical Transactions of the Royal Society A: Mathematical, Physical and Engineering Sciences*, vol. 364, no. 1838, pp. 15–30, Nov. 2005. DOI: 10.1098/rsta.2005.1678.

[32] L. R. Meza, "Design, fabrication, and mechanical property analysis of 3D nanoarchitected materials," PhD thesis, California Institute of Technology, Pasadena, CA, 2016.

[33] S.-W. Lee, M. Jafary-Zadeh, D. Z. Chen, Y.-W. Zhang, and J. R. Greer, "Size effect suppresses brittle failure in hollow Cu60Zr40 metallic glass nanolattices deformed at cryogenic temperatures," *Nano Letters*, vol. 15, no. 9, pp. 5673–5681, 2015, PMID: 26262592. DOI: 10.1021/acs.nanolett.5b01034.

[34] R. Liontas and J. R. Greer, "3D nano-architected metallic glass: Size effect suppresses catastrophic failure," *Acta Materialia*, vol. 133, pp. 393–407, 2017. DOI: https://doi.org/10.1016/j.actamat.2017.05.019.

[35] L. C. Montemayor, W. H. Wong, Y. W. Zhang, and J. R. Greer, "Insensitivity to flaws leads to damage tolerance in brittle architected meta-materials," *Scientific Reports*, vol. 6, Feb. 2016. DOI: 10.1038/srep20570.

[36] A. J. D. Shaikeea, H. Cui, M. O'Masta, X. R. Zheng, and V. S. Deshpande, "The toughness of mechanical metamaterials," *Nature Materials*, vol. 21, no. 3, pp. 297–304, 2022. DOI: 10.1038/s41563-021-01182-1.

[37] M. Maurizi, B. W. Edwards, C. Gao, J. R. Greer, and F. Berto, "Fracture resistance of 3D nano-architected lattice materials," *Extreme Mechanics Letters*, vol. 56, Oct. 2022. DOI: 10.1016/j.eml.2022.101883.

[38] Y. Wang, K. Wu, X. Zhang, X. Li, Y. Wang, and H. Gao, "Superior fracture resistance and topology-induced intrinsic toughening mechanism in 3D shell-based lattice meta-materials," *Science Advances*, vol. 10, no. 35, eadq2664, 2024. DOI: 10.1126/sciadv.adq2664.

[39] Z. Gao et al., "Damage-programmable design of metamaterials achieving crack-resisting mechanisms seen in nature," *Nature Communications*, vol. 15, 1 Dec. 2024. DOI: 10.1038/s41467-024-51757-0.

[40] Z. Wang et al., "Strut-buckling transformation enabling anomalous density-scaling toughening law in ultralight lattice metamaterials," *Advanced Materials*, vol. 37, no. 27, p. 2 419 635, 2025. DOI: https://doi.org/10.1002/adma.202419635.

[41] A. J. Mateos, W. Huang, Y.-W. Zhang, and J. R. Greer, "Discrete-continuum duality of architected materials: Failure, flaws, and fracture," *Advanced Functional Materials*, vol. 29, no. 5, p. 1 806 772, 2019. DOI: https://doi.org/10.1002/adfm.201806772.

[42] R. Schwaiger, L. R. Meza, and X. Li, "The extreme mechanics of micro- and nanoarchitected materials," *MRS Bulletin*, vol. 44, pp. 758–765, 10 Oct. 2019. DOI: 10.1557/mrs.2019.230.

[43] X. Feng et al., "Microalloyed medium-entropy alloy (MEA) composite nanolattices with ultrahigh toughness and cyclability," *Materials Today*, vol. 42, pp. 10–16, Jan. 2021. DOI: 10.1016/j.mattod.2020.10.003.

[44] W. Cheng et al., "Unlocking superior fracture resistance in micro-ceramics for architected meta-materials via ALD stress engineering," *Acta Materialia*, vol. 301, p. 121 474, 2025. DOI: https://doi.org/10.1016/j.actamat.2025.121474.

[45] A. Maggi, H. Li, and J. R. Greer, "Three-dimensional nano-architected scaffolds with tunable stiffness for efficient bone tissue growth," *Acta Biomaterialia*, vol. 63, pp. 294–305, 2017. DOI: https://doi.org/10.1016/j.actbio.2017.09.007.

[46] X. Zheng et al., "Ultralight, ultrastiff mechanical metamaterials," *Science*, vol. 344, no. 6190, pp. 1373–1377, 2014. DOI: 10.1126/science.1252291.

[47] L. R. Meza, A. J. Zelhofer, N. Clarke, A. J. Mateos, D. M. Kochmann, and J. R. Greer, "Resilient 3D hierarchical architected metamaterials," *Proceedings of the National Academy of Sciences*, vol. 112, no. 37, pp. 11 502–11 507, 2015. DOI: 10.1073/pnas.1509120112.

[48] D. W. Abueidda, M. Elhebeary, C.-S. (Shiang, R. K. A. Al-Rub, and I. M. Jasiuk, "Compression and buckling of microarchitectured neovius-lattice," *Extreme Mechanics Letters*, vol. 37, p. 100 688, 2020. DOI: https://doi.org/10.1016/j.eml.2020.100688.

[49] A. Schroer, J. M. Wheeler, and R. Schwaiger, "Deformation behavior and energy absorption capability of polymer and ceramic-polymer composite microlattices under cyclic loading," *Journal of Materials Research*, vol. 33, no. 3, pp. 274–289, 2018. DOI: 10.1557/jmr.2017.485.

[50] A. Maggi, J. Allen, T. Desai, and J. R. Greer, "Osteogenic cell functionality on 3-dimensional nano-scaffolds with varying stiffness," *Extreme Mechanics Letters*, vol. 13, pp. 1–9, 2017. DOI: https://doi.org/10.1016/j.eml.2017.01.002.

[51] A. R. Garcia-Taormina, C. M. Kurpiers, R. Schwaiger, and A. M. Hodge, "Coatings for core–shell composite micro-lattice structures: Varying sputtering parameters," *Advanced Engineering Materials*, vol. 24, no. 4, p. 2 101 264, 2022. DOI: https://doi.org/10.1002/adem.202101264.

[52] X. Zhang et al., "Three-dimensional high-entropy alloy–polymer composite nanolattices that overcome the strength–recoverability trade-off," *Nano Letters*, vol. 18, no. 7, pp. 4247–4256, 2018. DOI: 10.1021/acs.nanolett.8b01241.

[53] L. Gao et al., "High-entropy alloy (HEA)-coated nanolattice structures and their mechanical properties," *Advanced Engineering Materials*, vol. 20, 1 Jan. 2018. DOI: 10.1002/adem.201700625.

[54] J. U. Surjadi, X. Feng, W. Zhou, and Y. Lu, "Optimizing film thickness to delay strut fracture in high-entropy alloy composite microlattices," *International Journal of Extreme Manufacturing*, vol. 3, 2 Apr. 2021. DOI: 10.1088/2631-7990/abd8e8.

[55] T. Juarez, A. Schroer, R. Schwaiger, and A. M. Hodge, "Evaluating sputter deposited metal coatings on 3D printed polymer micro-truss structures," *Materials and Design*, vol. 140, pp. 442–450, Feb. 2018. DOI: 10.1016/j.matdes.2017.12.005.

[56] R. W. Johnson, A. Hultqvist, and S. F. Bent, "A brief review of atomic layer deposition: From fundamentals to applications," *Materials Today*, vol. 17, no. 5, pp. 236–246, 2014. DOI: https://doi.org/10.1016/j.mattod.2014.04.026.

[57] O. M. Ylivaara et al., "Aluminum oxide from trimethylaluminum and water by atomic layer deposition: The temperature dependence of residual stress, elastic modulus, hardness and adhesion," *Thin Solid Films*, vol. 552, pp. 124–135, Feb. 2014. DOI: 10.1016/j.tsf.2013.11.112.

[58] P. O. Oviroh, R. Akbarzadeh, D. Pan, R. A. M. Coetzee, and T.-C. Jen, "New development of atomic layer deposition: Processes, methods and applications," *Science*

and Technology of Advanced Materials, vol. 20, no. 1, pp. 465–496, 2019, PMID: 31164953. DOI: 10.1080/14686996.2019.1599694.

[59] O. M. E. Ylivaara et al., "Aluminum oxide/titanium dioxide nanolaminates grown by atomic layer deposition: Growth and mechanical properties," *Journal of Vacuum Science & Technology A: Vacuum, Surfaces, and Films*, vol. 35, 1 Jan. 2017. DOI: 10.1116/1.4966198.

[60] L. Aarik, H. Mändar, A. Tarre, H.-M. Piirsoo, and J. Aarik, "Mechanical properties of crystalline and amorphous aluminum oxide thin films grown by atomic layer deposition," *Surface and Coatings Technology*, vol. 438, p. 128 409, 2022. DOI: https://doi.org/10.1016/j.surfcoat.2022.128409.

[61] O. M. Ylivaara et al., "Mechanical and optical properties of as-grown and thermally annealed titanium dioxide from titanium tetrachloride and water by atomic layer deposition," *Thin Solid Films*, vol. 732, p. 138 758, 2021. DOI: https://doi.org/10.1016/j.tsf.2021.138758.

[62] S. Shestaeva et al., "Mechanical, structural, and optical properties of PEALD metallic oxides for optical applications," *Applied Optics*, vol. 56, p. C47, 4 Feb. 2017. DOI: 10.1364/ao.56.000c47.

[63] P. Kelly and R. Arnell, "Magnetron sputtering: A review of recent developments and applications," *Vacuum*, vol. 56, no. 3, pp. 159–172, 2000. DOI: https://doi.org/10.1016/S0042-207X(99)00189-X.

[64] P. Borowski and J. Myśliwiec, "Recent advances in magnetron sputtering: From fundamentals to industrial applications," *Coatings*, vol. 15, no. 8, 2025. DOI: 10.3390/coatings15080922.

[65] R. Daniel and J. Musil, "Thin-film processing," in *Novel Nanocomposite Coatings: Advances and Industrial Applications*, CRC Press, 2014, ch. 2, pp. 27–60.

[66] J. U. Surjadi, X. Feng, R. Fan, W. Lin, X. Li, and Y. Lu, "Hollow medium-entropy alloy nanolattices with ultrahigh energy absorption and resilience," *NPG Asia Materials*, vol. 13, 1 Dec. 2021. DOI: 10.1038/s41427-021-00306-y.

[67] H. Holleck and V. Schier, "Multilayer PVD coatings for wear protection," *Surface and Coatings Technology*, vol. 76-77, pp. 328–336, 1995. DOI: https://doi.org/10.1016/0257-8972(95)02555-3.

[68] R. Ali, M. Sebastiani, and E. Bemporad, "Influence of Ti–TiN multilayer PVD-coatings design on residual stresses and adhesion," *Materials & Design*, vol. 75, pp. 47–56, 2015. DOI: https://doi.org/10.1016/j.matdes.2015.03.007.

[69] R. Daniel et al., "Fracture toughness enhancement of brittle nanostructured materials by spatial heterogeneity: A micromechanical proof for CrN/Cr and TiN/SiOx multilayers," *Materials & Design*, vol. 104, pp. 227–234, 2016. DOI: https://doi.org/10.1016/j.matdes.2016.05.029.

[70] C. Zhou et al., "Effects of modulation layer thickness on fracture toughness of a TiN/AlN-Ni multilayer film," *Materials & Design*, vol. 222, p. 111 097, 2022. DOI: https://doi.org/10.1016/j.matdes.2022.111097.

[71] M. Fallmann, Z. Chen, Z. Zhang, P. Mayrhofer, and M. Bartosik, "Mechanical properties and epitaxial growth of TiN/AlN superlattices," *Surface and Coatings Technology*, vol. 375, pp. 1–7, 2019. DOI: https://doi.org/10.1016/j.surfcoat.2019.07.003.

[72] J. Roa et al., "Contact damage and fracture micromechanisms of multilayered TiN/CrN coatings at micro- and nano-length scales," *Thin Solid Films*, vol. 571, pp. 308–315, 2014, Multilayers 2013. DOI: https://doi.org/10.1016/j.tsf.2014.04.018.

[73] K. Rzepiejewska-Malyska, M. Parlinska-Wojtan, K. Wasmer, K. Hejduk, and J. Michler, "In-situ SEM indentation studies of the deformation mechanisms in TiN, CrN and TiN/CrN," *Micron*, vol. 40, no. 1, pp. 22–27, 2009. DOI: https://doi.org/10.1016/j.micron.2008.02.013.

[74] A. Azizpour, R. Hahn, F. F. Klimashin, T. Wojcik, E. Poursaeidi, and P. H. Mayrhofer, "Deformation and cracking mechanism in CrN/TiN multilayer coatings," *Coatings*, vol. 9, no. 6, 2019. DOI: 10.3390/coatings9060363.

[75] M. Stueber, H. Holleck, H. Leiste, K. Seemann, S. Ulrich, and C. Ziebert, "Concepts for the design of advanced nanoscale PVD multilayer protective thin films," *Journal of Alloys and Compounds*, vol. 483, no. 1, pp. 321–333, 2009, 14th International Symposium on Metastable and Nano-Materials (ISMANAM-2007). DOI: https://doi.org/10.1016/j.jallcom.2008.08.133.

[76] D. E. White, W. Cheng, K. Jagadish, E. Rossi, Y.-T. Shao, and A. M. Hodge, "Deformation behavior of optical ceramic nanomultilayers: The role of aperiodicity," *Advanced Engineering Materials*, vol. 27, no. 21, e202501269, 2025. DOI: https://doi.org/10.1002/adem.202501269.

[77] I. N. Sneddon, "The relation between load and penetration in the axisymmetric boussinesq problem for a punch of arbitrary profile," *International Journal of Engineering Science*, vol. 3, no. 1, pp. 47–57, 1965. DOI: https://doi.org/10.1016/0020-7225(65)90019-4.

[78] W. Oliver and G. Pharr, "An improved technique for determining hardness and elastic modulus using load and displacement sensing indentation experiments," *Journal of Materials Research*, vol. 7, pp. 1564–1583, 6 Jun. 1992. DOI: 10.1557/jmr.1992.1564.

[79] A. C. Fischer-Cripps, *Nanoindentation* (Mechanical Engineering Series), 3rd. New York, NY, USA: Springer Science + Business Media, 2011. DOI: 10.1007/978-1-4419-9872-9.

[80] A. Bolshakov, W. C. Oliver, and G. M. Pharr, "Finite element studies of the influence of pile-up on the analysis of nanoindentation data," *MRS Proceedings*, vol. 436, p. 141, 1996. DOI: 10.1557/PROC-436-141.

[81] E. Rossi, D. Duranti, S. Rashid, M. Zitek, R. Daniel, and M. Sebastiani, "A high-throughput framework for pile-up correction in high-speed nanoindentation maps," *Materials / & Design*, vol. 251, p. 113 708, 2025. DOI: https://doi.org/10.1016/j.matdes.2025.113708.

[82] J. B. Pethica and W. C. Oliver, "Mechanical properties of nanometre volumes of material: Use of the elastic response of small area indentations," *MRS Proceedings*, vol. 130, p. 13, 1988. DOI: 10.1557/PROC-130-13.

[83] Agilent Technologies, *Nano indenter G200 user's guide*, Technical Manual, Part Number G2A-13192-1, Edition Rev D, 1601 California Street, Palo Alto, CA 94304, USA, 2013.

[84] T. Y. Tsui, C. A. Ross, and G. M. Pharr, "Nanoindentation hardness of soft films on hard substrates: Effects of the substrate," *MRS Proceedings*, vol. 473, p. 57, 1997. DOI: 10.1557/PROC-473-57.

[85] T. Y. Tsui and G. M. Pharr, "Substrate effects on nanoindentation mechanical property measurement of soft films on hard substrates," *Journal of Materials Research*, vol. 14, no. 1, pp. 292–301, 1999. DOI: 10.1557/JMR.1999.0042.

[86] R. Saha and W. D. Nix, "Effects of the substrate on the determination of thin film mechanical properties by nanoindentation," *Acta Materialia*, vol. 50, no. 1, pp. 23–38, 2002. DOI: https://doi.org/10.1016/S1359-6454(01)00328-7.

[87] Z. Wei, G. Zhang, H. Chen, J. Luo, R. Liu, and S. Guo, "A simple method for evaluating elastic modulus of thin films by nanoindentation," *Journal of Materials Research*, vol. 24, no. 3, pp. 801–815, 2009. DOI: 10.1557/jmr.2009.0126.

[88] M. F. Doerner and W. D. Nix, "A method for interpreting the data from depth-sensing indentation instruments," *Journal of Materials Research*, vol. 1, pp. 601–609, 4 1986. DOI: 10.1557/JMR.1986.0601.

[89] R. B. King, "Elastic analysis of some punch problems for a layered medium," 1987, pp. 1657–1664.

[90] A. Korsunsky, M. McGurk, S. Bull, and T. Page, "On the hardness of coated systems," *Surface and Coatings Technology*, vol. 99, no. 1, pp. 171–183, 1998. DOI: https://doi.org/10.1016/S0257-8972(97)00522-7.

[91] J. Tuck, A. Korsunsky, D. Bhat, and S. Bull, "Indentation hardness evaluation of cathodic arc deposited thin hard coatings," *Surface and Coatings Technology*, vol. 139, no. 1, pp. 63–74, 2001. DOI: https://doi.org/10.1016/S0257-8972(00)01116-6.

[92] T. L. Anderson, *Fracture Mechanics: Fundamentals and Applications*, 4th. Boca Raton: CRC Press, 2017, p. 684. DOI: 10.1201/9781315370293.

[93] A. A. Griffith, "VI. the phenomena of rupture and flow in solids," *Philosophical Transactions of the Royal Society of London. Series A, Containing Papers of a Mathematical or Physical Character*, vol. 221, no. 582-593, pp. 163–198, 1920. DOI: 10.1098/rsta.1921.0006.

[94] G. R. Irwin, "Fracture dynamics," in *Fracturing of Metals*, Cleveland: American Society for Metals, 1948, pp. 147–166.

[95] E. Orowan, "Fracture and strength of solids," *Reports on Progress in Physics*, vol. 12, p. 185, 1948.

[96] G. R. Irwin, "Onset of fast crack propagation in high strength steel and aluminum alloys," in *Sagamore Research Conference Proceedings*, vol. 2, 1956, pp. 289–305.

[97] G. R. Irwin, "Analysis of stresses and strains near the end of a crack traversing a plate," *Journal of Applied Mechanics*, vol. 24, no. 3, pp. 361–364, Jun. 1957. DOI: 10.1115/1.4011547.

[98] B. R. LAWN, A. G. EVANS, and D. B. MARSHALL, "Elastic/plastic indentation damage in ceramics: The median/radial crack system," *Journal of the American Ceramic Society*, vol. 63, no. 9-10, pp. 574–581, 1980. DOI: https://doi.org/10.1111/j.1151-2916.1980.tb10768.x.

[99] B. Lawn and R. Wilshaw, "Indentation fracture: Principles and applications," *Journal of Materials Science*, vol. 10, no. 6, pp. 1049–1081, Jun. 1975. DOI: 10.1007/BF00823224.

[100] G. ANSTIS, P. CHANTIKUL, B. LAWN, and D. MARSHALL, "A critical evaluation of indentation techniques for measuring fracture toughness: I, direct crack measurements," *Journal of the American Ceramic Society*, vol. 64, no. 9, pp. 533–538, 1981. DOI: https://doi.org/10.1111/j.1151-2916.1981.tb10320.x.

[101] P. CHANTIKUL, G. R. ANSTIS, B. R. LAWN, and D. B. MARSHALL, "A critical evaluation of indentation techniques for measuring fracture toughness: II, strength method," *Journal of the American Ceramic Society*, vol. 64, no. 9, pp. 539–543, 1981. DOI: https://doi.org/10.1111/j.1151-2916.1981.tb10321.x.

[102] B. R. LAWN and D. B. MARSHALL, "Hardness, toughness, and brittleness: An indentation analysis," *Journal of the American Ceramic Society*, vol. 62, no. 7-8, pp. 347–350, 1979. DOI: https://doi.org/10.1111/j.1151-2916.1979.tb19075.x.

[103] D. M. Marsh, "Plastic flow in glass," *Proceedings of the Royal Society of London. Series A, Mathematical and Physical Sciences*, vol. 279, no. 1378, pp. 420–435, 1964. DOI: 10.1098/rspa.1964.0114.

[104] I. N. Sneddon, "The distribution of stress in the neighbourhood of a crack in an elastic solid," *Proceedings of the Royal Society of London. Series A. Mathematical and Physical Sciences*, vol. 187, no. 1009, pp. 229–260, 1946. DOI: 10.1098/rspa.1946.0077.

[105] M. Sebastiani, K. E. Johanns, E. G. Herbert, F. Carassiti, and G. M. Pharr, "A novel pillar indentation splitting test for measuring fracture toughness of thin ceramic coatings," *Philosophical Magazine*, vol. 95, pp. 1928–1944, 16-18 Jun. 2015. DOI: 10.1080/14786435.2014.913110.

[106] M. Sebastiani, K. Johanns, E. Herbert, and G. Pharr, "Measurement of fracture toughness by nanoindentation methods: Recent advances and future challenges," *Current Opinion in Solid State and Materials Science*, vol. 19, no. 6, pp. 324–333, 2015, Recent Advances in Nanoindentation. DOI: https://doi.org/10.1016/j.cossms.2015.04.003.

[107] M. Ghidelli, M. Sebastiani, K. E. K. Johanns, and G. M. G. Pharr, "Effects of indenter angle on micro-scale fracture toughness measurement by pillar splitting," *Journal of the American Ceramic Society*, vol. 100, pp. 5731–5738, 12 Dec. 2017. DOI: 10.1111/jace.15093.

[108] C. M. Lauener, L. Petho, M. Chen, Y. Xiao, J. Michler, and J. M. Wheeler, "Fracture of silicon: Influence of rate, positioning accuracy, FIB machining, and elevated temperatures

on toughness measured by pillar indentation splitting," *Materials and Design*, vol. 142, pp. 340–349, Mar. 2018. DOI: 10.1016/j.matdes.2018.01.015.

[109] M. Z. Mughal, R. Moscatelli, H.-Y. Amanieu, and M. Sebastiani, "Effect of lithiation on micro-scale fracture toughness of LixMn2O4 cathode," *Scripta Materialia*, vol. 116, pp. 62–66, 2016. DOI: https://doi.org/10.1016/j.scriptamat.2016.01.023.

[110] A. N. Wang, J. F. Nonemacher, G. Yan, M. Finsterbusch, J. Malzbender, and M. Krüger, "Mechanical properties of the solid electrolyte Al-substituted Li7La3Zr2O12 (LLZO) by utilizing micro-pillar indentation splitting test," *Journal of the European Ceramic Society*, vol. 38, pp. 3201–3209, 9 Aug. 2018. DOI: 10.1016/J.JEURCERAMSOC.2018.02.032.

[111] J. F. Nonemacher, Y. Arinicheva, G. Yan, M. Finsterbusch, M. Krüger, and J. Malzbender, "Fracture toughness of single grains and polycrystalline Li7La3Zr2O12 electrolyte material based on a pillar splitting method," *Journal of the European Ceramic Society*, vol. 40, pp. 3057–3064, 8 Jul. 2020. DOI: 10.1016/J.JEURCERAMSOC.2020.03.028.

[112] G. Yan et al., "Fracture behavior of solid electrolyte LATP material based on micro-pillar splitting method," *Journal of the European Ceramic Society*, vol. 41, pp. 5240–5247, 10 Aug. 2021. DOI: 10.1016/J.JEURCERAMSOC.2021.04.026.

[113] W. Zhou et al., "Mechanical properties of BaCe0.65Zr0.2Y0.15O3-δ – Ce0.85Gd0.15O2-δ dual-phase proton-conducting material with emphasis on micro-pillar splitting," *Journal of the European Ceramic Society*, vol. 42, pp. 3948–3956, 9 Aug. 2022. DOI: 10.1016/J.JEURCERAMSOC.2022.03.020.

[114] L. Li, X. Zhen, R. Zheng, C. Ma, and C. Liu, "Further understanding of the improved mechanical properties for SiCf/BN/SiC composites prepared by CVI+PIP hybrid technique: Application of micro-mechanical methods," *Composites Part B: Engineering*, vol. 283, p. 111 633, Aug. 2024. DOI: 10.1016/J.COMPOSITESB.2024.111633.

[115] D. E. White, C. D. Appleget, E. Rossi, M. Sebastiani, and A. M. Hodge, "The mechanical performance of optically tuned ceramic nanomultilayers," *Materials & Design*, vol. 231, p. 112 014, 2023. DOI: https://doi.org/10.1016/j.matdes.2023.112014.

[116] Y. Xia et al., "Investigation of fracture toughness and microstructure of micro-scaled multilayer-DLC/silicon system via pillar splitting method," *Ceramics International*, vol. 49, no. 23, Part B, pp. 38 662–38 671, 2023. DOI: https://doi.org/10.1016/j.ceramint.2023.09.199.

[117] Y. Xia et al., "Toughness measurement of microscale coating/silicon MEMS system using pillar splitting method," *IEEE Transactions on Instrumentation and Measurement*, vol. 73, 2024. DOI: 10.1109/TIM.2024.3403192.

[118] J. P. Best, J. Wehrs, M. Polyakov, M. Morstein, and J. Michler, "High temperature fracture toughness of ceramic coatings evaluated using micro-pillar splitting," *Scripta Materialia*, vol. 162, pp. 190–194, Mar. 2019. DOI: 10.1016/J.SCRIPTAMAT.2018.11.013.

[119] A. Kanjilal et al., "Temperature-driven nanoscale brittle-to-ductile transition of the C15 CaAl2 laves phase," *Materials & Design*, vol. 244, p. 113 206, Aug. 2024. DOI: 10.1016/J.MATDES.2024.113206.

[120] T. Beirau, E. Rossi, M. Sebastiani, W. C. Oliver, H. Pöllmann, and R. C. Ewing, "Fracture toughness of radiation-damaged zircon studied by nanoindentation pillar-splitting," *Applied Physics Letters*, vol. 119, no. 23, p. 231 903, Dec. 2021. DOI: 10.1063/5.0070597.

[121] G. Bolelli et al., "Damage progression in thermal barrier coating systems during thermal cycling: A nano-mechanical assessment," *Materials & Design*, vol. 166, p. 107 615, Mar. 2019. DOI: 10.1016/J.MATDES.2019.107615.

[122] S. Bursich et al., "The effect of ceramic YSZ powder morphology on coating performance for industrial TBCs," *Surface and Coatings Technology*, vol. 476, p. 130 270, Jan. 2024. DOI: 10.1016/J.SURFCOAT.2023.130270.

[123] A. Korsunsky et al., "Nanoscale residual stress depth profiling by focused ion beam milling and eigenstrain analysis," *Materials & Design*, vol. 145, pp. 55–64, 2018. DOI: https://doi.org/10.1016/j.matdes.2018.02.044.

[124] J. O. Carneiro, V. Teixeira, and S. Azevedo, "Residual stresses in thin films evaluated by different experimental techniques," in *Encyclopedia of Thermal Stresses*, R. B. Hetnarski, Ed. Dordrecht: Springer Netherlands, 2014, pp. 4222–4231. DOI: 10.1007/978-94-007-2739-7_64.

[125] H. Oettel and R. Wiedemann, "Residual stresses in pvd hard coatings," *Surface and Coatings Technology*, vol. 76-77, pp. 265–273, 1995. DOI: https://doi.org/10.1016/0257-8972(95)02581-2.

[126] A. M. Korsunsky, M. Sebastiani, and E. Bemporad, "Focused ion beam ring drilling for residual stress evaluation," *Materials Letters*, vol. 63, no. 22, pp. 1961–1963, 2009. DOI: https://doi.org/10.1016/j.matlet.2009.06.020.

[127] E. Salvati, L. Romano-Brandt, M. Mughal, M. Sebastiani, and A. Korsunsky, "Generalised residual stress depth profiling at the nanoscale using focused ion beam milling," *Journal of the Mechanics and Physics of Solids*, vol. 125, pp. 488–501, 2019. DOI: https://doi.org/10.1016/j.jmps.2019.01.007.

[128] F. Quintero et al., "Continuous fiberizing by laser melting (Cofiblas): Production of highly flexible glass nanofibers with effectively unlimited length," *Science Advances*, vol. 6, no. 6, eaax7210, 2020. DOI: 10.1126/sciadv.aax7210.

[129] J. He et al., "Solution processes for ultrabroadband and omnidirectional graded-index glass lenses with near-zero reflectivity in high concentration photovoltaics," *Scientific Reports*, vol. 8, no. 1, p. 14 907, 2018. DOI: 10.1038/s41598-018-33200-9.

[130] A. J. Ikushima, T. Fujiwara, and K. Saito, "Silica glass: A material for photonics," *Journal of Applied Physics*, vol. 88, no. 3, pp. 1201–1213, Aug. 2000. DOI: 10.1063/1.373805.

[131] J. D. Musgraves, J. Hu, and L. Calvez, Eds., *Springer Handbook of Glass* (Springer Handbooks), 1st ed. Cham: Springer, 2019, 1841 pp., XXXVI, 1841 pages; 1400 colour illustrations. DOI: 10.1007/978-3-319-93728-1.

[132] X.-Q. Liu et al., "Optical nanofabrication of concave microlens arrays," *Laser & Photonics Reviews*, vol. 13, no. 5, p. 1 800 272, 2019. DOI: https://doi.org/10.1002/lpor.201800272.

[133] F. Kotz et al., "Two-photon polymerization of nanocomposites for the fabrication of transparent fused silica glass microstructures," *Advanced Materials*, vol. 33, no. 9, p. 2 006 341, 2021. DOI: https://doi.org/10.1002/adma.202006341.

[134] F. Kotz et al., "Three-dimensional printing of transparent fused silica glass," *Nature*, vol. 544, no. 7650, pp. 337–339, 2017. DOI: 10.1038/nature22061.

[135] M. Mader et al., "High-throughput injection molding of transparent fused silica glass," *Science*, vol. 372, no. 6538, pp. 182–186, 2021. DOI: 10.1126/science.abf1537.

[136] X. Wen et al., "3D-printed silica with nanoscale resolution," *Nature Materials*, vol. 20, no. 11, pp. 1506–1511, 2021. DOI: 10.1038/s41563-021-01111-2.

[137] J. Bauer, C. Crook, and T. Baldacchini, "A sinterless, low-temperature route to 3D print nanoscale optical-grade glass," *Science*, vol. 380, no. 6648, pp. 960–966, 2023. DOI: 10.1126/science.abq3037.

[138] S. Bruns, L. Petho, C. Minnert, J. Michler, and K. Durst, "Fracture toughness determination of fused silica by cube corner indentation cracking and pillar splitting," *Materials and Design*, vol. 186, Jan. 2020. DOI: 10.1016/j.matdes.2019.108311.

[139] J. Ast, M. Ghidelli, K. Durst, M. Göken, M. Sebastiani, and A. Korsunsky, "A review of experimental approaches to fracture toughness evaluation at the micro-scale," *Materials & Design*, vol. 173, p. 107 762, 2019. DOI: https://doi.org/10.1016/j.matdes.2019.107762.

[140] S. Bruns, K. E. Johanns, H. U. Rehman, G. M. Pharr, and K. Durst, "Constitutive modeling of indentation cracking in fused silica," *Journal of the American Ceramic Society*, vol. 100, pp. 1928–1940, 5 May 2017. DOI: 10.1111/jace.14734.

[141] S. Bruns et al., "Indentation densification of fused silica assessed by raman spectroscopy and constitutive finite element analysis," *Journal of the American Ceramic Society*, vol. 103, no. 5, pp. 3076–3088, 2020. DOI: https://doi.org/10.1111/jace.17024.

[142] H. Liang et al., "Investigation of the effect of berkovich and cube corner indentations on the mechanical behavior of fused silica using molecular dynamics and finite element simulation," *Ceramics International*, vol. 48, no. 19, Part B, pp. 28 781–28 789, 2022,

Recent Advances in Structural and Functional Ceramics: Development, characterization, properties, and applications. DOI: https://doi.org/10.1016/j.ceramint.2021.12.201.

[143] R. N. Widmer, D. Bischof, J. Jurczyk, M. Michler, J. Schwiedrzik, and J. Michler, "Smooth or not: Robust fused silica micro-components by femtosecond-laser-assisted etching," *Materials & Design*, vol. 204, p. 109 670, 2021. DOI: https://doi.org/10.1016/j.matdes.2021.109670.

[144] D. Tromans and J. Meech, "Fracture toughness and surface energies of covalent minerals: Theoretical estimates," *Minerals Engineering*, vol. 17, no. 1, pp. 1–15, 2004. DOI: https://doi.org/10.1016/j.mineng.2003.09.006.

[145] R. J. Charles, "A review of glass strength," *Progress in Ceramic Science*, vol. 1, pp. 1–38, 1961.

[146] S. M. WIEDERHORN, "Fracture surface energy of glass," *Journal of the American Ceramic Society*, vol. 52, no. 2, pp. 99–105, 1969. DOI: https://doi.org/10.1111/j.1151-2916.1969.tb13350.x.

[147] F. Célarié et al., "Glass breaks like metal, but at the nanometer scale," *Phys. Rev. Lett.*, vol. 90, p. 075 504, 7 Feb. 2003. DOI: 10.1103/PhysRevLett.90.075504.

[148] R. Barciela, T. S. Mahadevan, F. Quintero, J. Pou, and J. Du, "Size effects on the fracture behavior of amorphous silica from molecular dynamics simulations," *Journal of Non-Crystalline Solids*, vol. 631, p. 122 935, 2024. DOI: https://doi.org/10.1016/j.jnoncrysol.2024.122935.

[149] J. Luo et al., "Size-dependent brittle-to-ductile transition in silica glass nanofibers," eng, *Nano letters*, vol. 16, no. 1, pp. 105–113, 2016.

[150] S. King and G. Antonelli, "Simple bond energy approach for non-destructive measurements of the fracture toughness of brittle materials," *Thin Solid Films*, vol. 515, no. 18, pp. 7232–7241, 2007. DOI: https://doi.org/10.1016/j.tsf.2007.02.106.

[151] R. H. Doremus, "Viscosity of silica," *Journal of Applied Physics*, vol. 92, no. 12, pp. 7619–7629, Dec. 2002. DOI: 10.1063/1.1515132.

[152] Y. Shi, D. Ma, A. P. Song, B. Wheaton, M. Bauchy, and S. R. Elliott, "Structural evolution of fused silica below the glass-transition temperature revealed by in-situ neutron total scattering," *Journal of Non-Crystalline Solids*, vol. 528, p. 119 760, 2020. DOI: https://doi.org/10.1016/j.jnoncrysol.2019.119760.

[153] R. C. Breneman and J. W. Halloran, "Kinetics of cristobalite formation in sintered silica," *Journal of the American Ceramic Society*, vol. 97, no. 7, pp. 2272–2278, 2014. DOI: https://doi.org/10.1111/jace.12889.

[154] L. Huang and J. Kieffer, "Amorphous-amorphous transitions in silica glass. I. reversible transitions and thermomechanical anomalies," *Phys. Rev. B*, vol. 69, p. 224 203, 22 Jun. 2004. DOI: 10.1103/PhysRevB.69.224203.

[155] R. Le Parc, C. Levelut, J. Pelous, V. Martinez, and B. Champagnon, "Influence of fictive temperature and composition of silica glass on anomalous elastic behaviour," *Journal of Physics: Condensed Matter*, vol. 18, no. 32, p. 7507, Jul. 2006. DOI: 10.1088/0953-8984/18/32/001.

[156] L. Huang and J. Kieffer, "Amorphous-amorphous transitions in silica glass. II. irreversible transitions and densification limit," *Phys. Rev. B*, vol. 69, p. 224 204, 22 Jun. 2004. DOI: 10.1103/PhysRevB.69.224204.

[157] J. Bauer, L. R. Meza, T. A. Schaedler, R. Schwaiger, X. Zheng, and L. Valdevit, "Nanolattices: An emerging class of mechanical metamaterials," *Advanced Materials*, vol. 29, pp. 1–26, 40 2017. DOI: 10.1002/adma.201701850.

[158] X. Chen et al., "3D lightweight mechanical metamaterial with nearly isotropic inelastic large deformation response," *Journal of the Mechanics and Physics of Solids*, vol. 169, Dec. 2022. DOI: 10.1016/j.jmps.2022.105057.

[159] R. W. Johnson, A. Hultqvist, and S. F. Bent, "A brief review of atomic layer deposition: From fundamentals to applications," *Materials Today*, vol. 17, no. 5, pp. 236–246, 2014. DOI: https://doi.org/10.1016/j.mattod.2014.04.026.

[160] E. Rossi, J. Bauer, and M. Sebastiani, "Humidity-dependent flaw sensitivity in the crack propagation resistance of 3D-printed nano-ceramics," *Scripta Materialia*, vol. 194, Mar. 2021. DOI: 10.1016/j.scriptamat.2020.113684.

[161] M. Lugovy, V. Slyunyayev, N. Orlovskaya, G. Blugan, J. Kuebler, and M. Lewis, "Apparent fracture toughness of Si3N4-based laminates with residual compressive or tensile stresses in surface layers," *Acta Materialia*, vol. 53, no. 2, pp. 289–296, 2005. DOI: https://doi.org/10.1016/j.actamat.2004.09.022.

[162] Z. Xia, W. Curtin, and B. Sheldon, "A new method to evaluate the fracture toughness of thin films," *Acta Materialia*, vol. 52, no. 12, pp. 3507–3517, 2004. DOI: https://doi.org/10.1016/j.actamat.2004.04.004.

[163] S. M. Sajadi et al., "Damage-tolerant 3D-printed ceramics via conformal coating," *Science Advances*, vol. 7, no. 28, eabc5028, 2021. DOI: 10.1126/sciadv.abc5028.

[164] M. Sebastiani, C. Eberl, E. Bemporad, and G. M. Pharr, "Depth-resolved residual stress analysis of thin coatings by a new FIB–DIC method," *Materials Science and Engineering: A*, vol. 528, no. 27, pp. 7901–7908, 2011. DOI: https://doi.org/10.1016/j.msea.2011.07.001.

[165] *Abaqus finite element analysis | SIMULIA - dassault systèmes*, https://www.3ds.com/products/simulia/abaqus, Accessed: 2024-10-17, 2024.

[166] K. E. Johanns, J. H. Lee, Y. F. Gao, and G. M. Pharr, "An evaluation of the advantages and limitations in simulating indentation cracking with cohesive zone finite elements," *Modelling and Simulation in Materials Science and Engineering*, vol. 22, 1 Jan. 2014. DOI: 10.1088/0965-0393/22/1/015011.

[167] J. Bauer, A. Schroer, R. Schwaiger, and O. Kraft, "The impact of size and loading direction on the strength of architected lattice materials," *Advanced Engineering Materials*, vol. 18, no. 9, pp. 1537–1543, 2016. DOI: https://doi.org/10.1002/adem.201600235.

[168] J. Zhao, R. Bradt, and P. Walker, "The fracture toughness of glassy carbons at elevated temperatures," *Carbon*, vol. 23, no. 1, pp. 15–18, 1985. DOI: https://doi.org/10.1016/0008-6223(85)90190-3.

[169] B. Winiarski, G. S. Schajer, and P. J. Withers, "Surface decoration for improving the accuracy of displacement measurements by digital image correlationin SEM," in *Application of Imaging Techniques to Mechanics of Materials and Structures, Volume 4*, T. Proulx, Ed., New York, NY: Springer New York, 2013, pp. 217–224.

[170] J. Chen, "Indentation-based methods to assess fracture toughness for thin coatings," *Journal of Physics D: Applied Physics*, vol. 45, no. 20, p. 203 001, May 2012. DOI: 10.1088/0022-3727/45/20/203001.

[171] G. Okuma, K. Maeda, S. Yoshida, A. Takeuchi, and F. Wakai, "Morphology of subsurface cracks in glass-ceramics induced by Vickers indentation observed by synchrotron X-ray multiscale tomography," *Scientific Reports*, vol. 12, 1 Dec. 2022. DOI: 10.1038/s41598-022-11084-0.

[172] J. Oishi and T. Kimura, "Thermal expansion of fused quartz," *Metrologia*, vol. 5, no. 2, p. 50, Apr. 1969. DOI: 10.1088/0026-1394/5/2/004.

[173] D. D. Markushev et al., "Thermal and elastic characterization of glassy carbon thin films by photoacoustic measurements," *The European Physical Journal Plus*, vol. 132, no. 2, p. 33, 2017. DOI: 10.1140/epjp/i2017-11307-2.

[174] D. C. Miller et al., "Thermo-mechanical properties of alumina films created using the atomic layer deposition technique," *Sensors and Actuators, A: Physical*, vol. 164, pp. 58–67, 1-2 Nov. 2010. DOI: 10.1016/j.sna.2010.09.018.

[175] S. Burgmann et al., "New avenues for residual stress analysis in ultrathin atomic layer deposited free-standing membranes through release of micro-cantilevers," *Heliyon*, vol. 10, 4 Feb. 2024. DOI: 10.1016/j.heliyon.2024.e26420.

[176] M. Berdova et al., "Mechanical assessment of suspended ALD thin films by bulge and shaft-loading techniques," *Acta Materialia*, vol. 66, pp. 370–377, 2014. DOI: 10.1016/j.actamat.2013.11.024.

[177] V. Chawla et al., "Fracture mechanics and oxygen gas barrier properties of Al2O3/ZnO nanolaminates on PET deposited by atomic layer deposition," *Nanomaterials*, vol. 9, 1 Jan. 2019. DOI: 10.3390/nano9010088.

[178] T. Singh, T. Lehnen, T. Leuning, D. Sahu, and S. Mathur, "Thickness dependence of optoelectronic properties in ALD grown ZnO thin films," *Applied Surface Science*, vol. 289, pp. 27–32, Jan. 2014. DOI: 10.1016/j.apsusc.2013.10.071.

[179] C.-H. Liang and Y.-J. Chen, "Fabrication of oxide-based near infrared-shielding coatings for a smart window to prevent infrared-induced photoaging in human skin," *Ceramics International*, vol. 47, no. 4, pp. 5177–5186, 2021. DOI: https://doi.org/10.1016/j.ceramint.2020.10.095.

[180] D. C. Harris, *Optical Properties of Infrared Windows: Materials for Infrared Windows and Domes: Properties and Performance*. Bellingham, Washington: SPIE, 1999.

[181] H. K. Raut, V. A. Ganesh, A. S. Nair, and S. Ramakrishna, "Anti-reflective coatings: A critical, in-depth review," *Energy Environ. Sci.*, vol. 4, no. 10, pp. 3779–3804, 2011. DOI: 10.1039/C1EE01297E.

[182] K. Ye and Z. Li, "Toward ceramic anticorrosion coatings: A review," *Corrosion*, vol. 76, no. 10, pp. 895–917, Jul. 2020. DOI: 10.5006/3560.

[183] S. PalDey and S. Deevi, "Single layer and multilayer wear resistant coatings of (Ti,Al)N: A review," *Materials Science and Engineering: A*, vol. 342, no. 1, pp. 58–79, 2003. DOI: https://doi.org/10.1016/S0921-5093(02)00259-9.

[184] A. Thobor et al., "Enhancement of mechanical properties of TiN/AlN multilayers by modifying the number and the quality of interfaces," *Surface and Coatings Technology*, vol. 124, no. 2, pp. 210–221, 2000. DOI: https://doi.org/10.1016/S0257-8972(99)00655-6.

[185] Z. R. Liu, Y. X. Xu, B. Peng, W. Wei, L. Chen, and Q. Wang, "Structure and property optimization of Ni-containing AlCrSiN coatings by nano-multilayer construction," *Journal of Alloys and Compounds*, vol. 808, p. 151 630, 2019. DOI: https://doi.org/10.1016/j.jallcom.2019.07.342.

[186] D. He, W. Li, L. Wang, Z. Lu, G. Zhang, and Z. Cai, "Impact wear behavior of WC/a-C nanomultilayers," *Materials Research Express*, vol. 6, no. 11, p. 116 443, Oct. 2019. DOI: 10.1088/2053-1591/ab4d29.

[187] J. González-Carmona et al., "Wear mechanisms identification using kelvin probe force microscopy in TiN, ZrN and TiN/ZrN hard ceramic multilayers coatings," *Ceramics International*, vol. 46, no. 15, pp. 24 592–24 604, 2020. DOI: https://doi.org/10.1016/j.ceramint.2020.06.248.

[188] G. Li, Y. Li, and G. Li, "Crystallization of amorphous AlN and superhardness effect in VC/AlN nanomultilayers," *Thin Solid Films*, vol. 520, no. 6, pp. 2032–2035, 2012. DOI: https://doi.org/10.1016/j.tsf.2011.09.079.

[189] M. Kong, J. Dai, J. Lao, and G. Li, "Crystallization of amorphous SiC and superhardness effect in TiN/SiC nanomultilayers," *Applied Surface Science*, vol. 253, no. 10, pp. 4734–4739, 2007. DOI: https://doi.org/10.1016/j.apsusc.2006.10.050.

[190] Y. Pan, L. Dong, N. Liu, J. Yu, C. Li, and D. Li, "Investigating the influence of epitaxial modulation on the evolution of superhardness of the VN/TiB2 multilayers," *Applied Surface Science*, vol. 390, pp. 406–411, 2016. DOI: https://doi.org/10.1016/j.apsusc.2016.08.133.

[191] P. Dubey, A. K. Battu, V. Shutthanandan, and C. V. Ramana, "Effect of interface structure on the hydrophobicity, mechanical and optical properties of HfO2/Mo/HfO2 multilayer films," *JOM*, vol. 71, no. 10, pp. 3711–3719, 2019. DOI: 10.1007/s11837-019-03614-5.

[192] E. Nichelatti, M. Montecchi, and R. Montereali, "Optical reflectance and transmittance of a multilayer coating affected by refractive-index inhomogeneity, interface roughness, and thickness wedge," *Journal of Non-Crystalline Solids*, vol. 355, no. 18, pp. 1115–1118, 2009, SiO2, Advanced Dielectrics and Related Devices. DOI: https://doi.org/10.1016/j.jnoncrysol.2008.11.040.

[193] I. Pana, C. Vitelaru, A. Kiss, N. C. Zoita, M. Dinu, and M. Braic, "Design, fabrication and characterization of TiO2-SiO2 multilayer with tailored color glazing for thermal

solar collectors," *Materials & Design*, vol. 130, pp. 275–284, 2017. DOI: https://doi.org/10.1016/j.matdes.2017.05.063.

[194] C.-H. Liang and Y.-J. Chen, "Fabrication of oxide-based near infrared-shielding coatings for a smart window to prevent infrared-induced photoaging in human skin," *Ceramics International*, vol. 47, no. 4, pp. 5177–5186, 2021. DOI: https://doi.org/10.1016/j.ceramint.2020.10.095.

[195] M. Mazur, D. Wojcieszak, J. Domaradzki, D. Kaczmarek, S. Song, and F. Placido, "TiO2/SiO2 multilayer as an antireflective and protective coating deposited by microwave assisted magnetron sputtering," *Opto-Electronics Review*, vol. 21, no. 2, pp. 233–238, 2013. DOI: doi:10.2478/s11772-013-0085-7.

[196] H. K. Raut, V. A. Ganesh, A. S. Nair, and S. Ramakrishna, "Anti-reflective coatings: A critical, in-depth review," *Energy Environ. Sci.*, vol. 4, pp. 3779–3804, 10 2011. DOI: 10.1039/C1EE01297E.

[197] T. Druffel, K. Geng, and E. Grulke, "Mechanical comparison of a polymer nanocomposite to a ceramic thin-film anti-reflective filter," *Nanotechnology*, vol. 17, no. 14, p. 3584, Jun. 2006. DOI: 10.1088/0957-4484/17/14/038.

[198] C. D. Appleget and A. M. Hodge, "Synthesis and characterization of optically transparent ceramic crystalline/amorphous and amorphous/amorphous multilayers," *Scripta Materialia*, vol. 187, pp. 157–162, 2020. DOI: https://doi.org/10.1016/j.scriptamat.2020.06.013.

[199] A. C. Fischer-Cripps, "Analysis of nanoindentation test data," in *Nanoindentation*. New York, NY: Springer New York, 2011, pp. 39–75. DOI: 10.1007/978-1-4419-9872-9_3.

[200] C.-h. Park, Y. H. Kim, H. Jeong, B.-R. Won, H. Jeon, and J.-h. Myung, "Development of robust YSZ thin-film electrolyte by RF sputtering and anode support design for stable IT-SOFC," *Ceramics International*, vol. 49, no. 20, pp. 32 953–32 961, 2023. DOI: https://doi.org/10.1016/j.ceramint.2023.07.270.

[201] Q.-L. Xiao, C. Xu, S.-Y. Shao, J.-D. Shao, and Z.-X. Fan, "Y2O3 stabilized ZrO2 thin films deposited by electron-beam evaporation: Optical properties, structure and residual stresses," *Vacuum*, vol. 83, no. 2, pp. 366–371, 2008. DOI: https://doi.org/10.1016/j.vacuum.2008.05.031.

[202] A. F. Dericioglu, "Effect of microstructure on the mechanical behavior of reactive magnetron sputtered Al2O3/TiO2 multilayer ceramics," *MATERIALS TRANSACTIONS*, vol. 49, no. 11, pp. 2714–2722, 2008. DOI: 10.2320/matertrans.MER2008055.

[203] J. González-Carmona et al., "Wear mechanisms identification using Kelvin probe force microscopy in TiN, ZrN and TiN/ZrN hard ceramic multilayers coatings," *Ceramics International*, vol. 46, no. 15, pp. 24 592–24 604, 2020. DOI: https://doi.org/10.1016/j.ceramint.2020.06.248.

[204] W. D. Callister and D. G. Rethwisch, *Materials Science and Engineering: An Introduction*, 9th. New York: John Wiley & Sons, 2014.

[205] AZoM. "The resource." Accessed: November 12, 2025. [Online]. Available: https://azom.com.

[206] P. Baral et al., "Al_2O_3/Al hybrid nanolaminates with superior toughness, strength and ductility," *Nature Communications*, vol. 16, no. 1, p. 1355, 2025. DOI: 10.1038/s41467-025-56512-7.

[207] R. N. Chan, B. R. Stoner, J. Y. Thompson, R. O. Scattergood, and J. R. Piascik, "Fracture toughness improvements of dental ceramic through use of yttria-stabilized zirconia (YSZ) thin-film coatings," *Dental Materials*, vol. 29, no. 8, pp. 881–887, 2013. DOI: https://doi.org/10.1016/j.dental.2013.05.003.

[208] D. Stollberg, J. Hampikian, L. Riester, and W. Carter, "Nanoindentation measurements of combustion CVD Al2O3 and YSZ films," *Materials Science and Engineering: A*, vol. 359, no. 1, pp. 112–118, 2003. DOI: https://doi.org/10.1016/S0921-5093(03)00339-3.

[209] Q. Gao and S. Zhu, *Textbook of Medical Statistics: For Medical Students*. Singapore: Springer Nature Singapore, 2024. DOI: 10.1007/978-981-99-7390-3.

[210] R. Bermejo, Y. Torres, A. Sánchez-Herencia, C. Baudín, M. Anglada, and L. Llanes, "Residual stresses, strength and toughness of laminates with different layer thickness ratios," *Acta Materialia*, vol. 54, no. 18, pp. 4745–4757, 2006. DOI: https://doi.org/10.1016/j.actamat.2006.06.008.

[211] D. E. White, K. Jagadish, Y.-T. Shao, and A. M. Hodge, "Synthesis and characterization of aperiodic multifunctional AlN/Al2O3 nanomultilayers," *Thin Solid Films*, vol. 815, p. 140 638, 2025. DOI: https://doi.org/10.1016/j.tsf.2025.140638.

[212] Y. Cui, P. Huang, F. Wang, T. Lu, and K. Xu, "The hardness and related deformation mechanisms in nanoscale crystalline–amorphous multilayers," *Thin Solid Films*, vol. 584, pp. 270–276, 2015, The 7th International Conference on Technological Advances of Thin Films & Surface Coatings (ThinFilms2014). DOI: https://doi.org/10.1016/j.tsf.2015.01.067.

[213] T. E. J. Edwards et al., "On the thinnest Al2O3 interlayers in Al-based nanolaminates to enhance strength, and the role of constraint," *Acta Materialia*, vol. 240, p. 118 345, 2022. DOI: https://doi.org/10.1016/j.actamat.2022.118345.

[214] P. Hollmann et al., "Investigation of cracking prevention in magnetron-sputtered TiAlN coatings during subsequent electron beam hardening," *Surface and Coatings Technology*, vol. 338, pp. 75–83, 2018. DOI: https://doi.org/10.1016/j.surfcoat.2017.12.042.